Dissertation

submitted to the

Combined Faculty of Natural Sciences and Mathematics

of the Ruperto Carola University Heidelberg, Germany

for the degree of

Doctor of Natural Sciences

Presented by

M.Sc. Letao Huang

born in: Hubei, China

Oral examination: 21. 11. 2025

Quantum Chemical Investigation of Excited States and Electron Transfer in Organic Semiconductors

Referees: Prof. Dr. Andreas Dreuw

Prof. Dr. Saeed Amirjalayer

Abstract

Amid the accelerating global energy transition and the deepening emphasis on sustainable development, organic semiconductors have attracted increasing attention as promising candidates for next-generation optoelectronic and energy devices, owing to their highly tunable molecular structures, low-cost processing, and excellent mechanical flexibility. A thorough understanding of the electronic structures of these molecules and their charge-transfer mechanism is crucial for guiding molecular design, optimizing device performance, and predicting functional properties. In particular, quantum chemical calculations provide useful quantitative insights into the excited-state behavior and charge mobility prediction, offering theoretical support for the design and optimization of organic semiconductor materials.

In this work, the photoexcitation processes of triphenylamine (**TPA**) and its dimethylmethylene-bridged derivative (**DTPA**) in chloroform solution were first explored. Unlike conventional cyclization reactions, which often produce significant carbazole by-products, the **TPA** derivatives act as electron donors transferring electrons to the electron-accepting chloroform, inducing dimer formation. The absorption spectra obtained from quantum chemical calculations agree closely with experimental measurements, validating the computational model and providing a quantitative basis for understanding electron transfer in solution.

Subsequently, the carrier mobilities of the organic molecules were calculated by combining Marcus–Hush theory with quantum chemical methods. By introducing a projection function based on the intermolecular polar angle (γ) and azimuthal angle (θ), the relative mobilities of different dimer types along specific directions were quantified, allowing precise characterization of anisotropic charge transport. Using this approach, the electronic structures and spatial charge transport properties of halogenated N-heteroacene derivatives **4Br-TIPS-TAP** and **4I-TIPS-TAP** were investigated. Both molecules exhibit typical n-type behavior, consistent with previous reports, highlighting the significant effects of molecular design and halogen substitution on crystal packing and transport properties.

Finally, the three-dimensional anisotropic charge transport of singlet fission (SF)–active diketopyrrolonaphthyridinedione derivatives, namely **DPND** and **DPND6**, was examined. The calculations indicate that the unsubstituted **DPND** predominantly favors p-type transport, whereas the side-chain–modified **DPND6** exhibits n-type characteristics. This result demonstrates that side-chain–induced changes in crystal packing can reverse the dominant carrier type, providing clear theoretical guidance for tuning charge transport through molecular design. These findings not only deepen the understanding of structure–property relationships in organic semiconductors but also offer feasible strategies for applying singlet fission materials in efficient optoelectronic devices.

Zusammenfassung

Angesichts der sich beschleunigenden globalen Energiewende und des wachsenden Fokus auf nachhaltige Entwicklung haben sich organische Halbleiter als vielversprechende Materialkandidaten für zukünftige optoelektrische Geräte und Energieträger bewiesen. Dies liegt an ihrer hochgradig anpassbaren molekularen Struktur, kostengünstigen Verarbeitung und hervorragenden mechanischen Flexibilität. Ein umfassendes Verständnis der elektronischen Struktur dieser Moleküle sowie ihres Ladungstransfermechanismus ist für ihr molekulares Design unerlässlich und hilft dabei, die Geräteleistung zu optimieren und funktionale Eigenschaften vorherzusagen. Insbesondere liefern quantenchemische Berechnungen nützliche quantitative Einblicke in das Verhalten angeregter Zustände und die Vorhersage der Ladungsträgermobilität. Sie bieten somit eine theoretische Grundlage für das Design und die Optimierung organischer Halbleitermaterialien.

In dieser Arbeit wurden zunächst die Photoanregungsprozesse von Triphenylamin (**TPA**) und seinem Dimethylmethylen-verbrückten Derivat (**DTPA**) in Chloroformlösung eingehend untersucht. Im Gegensatz zu herkömmlichen Cyclisierungsreaktionen, die häufig erhebliche Carbazol-Nebenprodukte erzeugen, fungieren die **TPA**-Derivate als Elektronendonoren, die Elektronen auf das elektronenakzeptierende Chloroform übertragen und dadurch die Dimerbildung induzieren. Die aus quantenchemischen Berechnungen erhaltenen Absorptionsspektren stimmen gut mit experimentellen Messungen überein, was das Berechnungsmodell validiert und eine quantitative Grundlage für das Verständnis des Elektronentransfers in Lösung liefert.

Anschließend wurden die Ladungsträgermobilitäten organischer Moleküle durch Kombination von Marcus–Hush-Theorie mit quantenchemischen Methoden berechnet. Durch die Einführung einer Projektionsfunktion, die auf dem intermolekularen Polwinkel (γ) und Azimutwinkel (θ) basiert, konnten die relativen Mobilitäten verschiedener Dimer-Typen entlang bestimmter Richtungen quantifiziert werden, was eine präzise Charakterisierung des anisotropen Ladungstransports ermöglicht. Mit diesem Ansatz wurden die elektronischen Strukturen und räumlichen Ladungstransporteigenschaften der halogenierten N-Heteroacen-Derivate **4Br-TIPS-TAP** und **4I-TIPS-TAP** untersucht. Beide Moleküle zeigen im Einklang mit früheren Berichten ein typisches n-Typ-Verhalten und betonen und verdeutlichen den erheblichen Einfluss von Moleküldesign und Halogensubstitution auf die Kristallpackung und Transporteigenschaften.

Abschließend wurde der dreidimensionale anisotrope Ladungstransport Singlet Fission (SF)-aktiver Diketopyrrolonaphthyridindion-Derivate **DPND** und **DPND6** untersucht. Die Berechnungen zeigen, dass das unsubstituierte **DPND** überwiegend p-Typ-Transport bevorzugt, während das seitenkettenmodifizierte **DPND6** n-Typ-Eigenschaften aufweist. Dieses Ergebnis belegt, dass seitenketteninduzierte Änderungen in der Kristallpackung den dominanten Ladungsträgertyp umkehren können und liefert eine klare theoretische Grundlage zur Steuerung des Ladungstransports durch molekulares Design. Diese Erkenntnisse vertiefen nicht nur das Verständnis der Struktur–Eigenschafts-Beziehungen in organischen Halbleitern, sondern bieten auch praktikable Strategien für den Einsatz von Singlet-Fission-Materialien in hocheffizienten optoelektronischen Geräten.

Contents

List of Figures

List of Tables

Chapter 1

General Introduction

Sunlight is the most abundant energy source available to humankind.[1] Developing efficient strategies for capturing and storing this energy to meet long-term societal demands represents one of the foremost challenges in contemporary science and technology.[2–4] Among various renewable energy technologies, photovoltaic (PV) power generation is widely regarded as one of the most promising clean energy pathways, as it can directly convert solar energy into electricity. With the continuous evolution of the global energy landscape, PV technology is becoming a key pillar of the future energy system. By contrast, fossil fuels are limited in reserve, with extraction and supply becoming increasingly costly. Their combustion releases substantial amounts of carbon dioxide along with other pollutants, thereby exerting serious impacts on the climate and the environment. Thus, the development and commercialization of renewable energy represents both an indispensable option for overcoming resource limitations and a key approach to achieving sustainable development while addressing environmental and climate challenges.[5]

The core of photovoltaic facilities is the solar cell panel. In the photoelectric conversion process of organic solar cells, electron transfer (ET) plays a crucial role. More broadly, ET is a fundamental process that widely exists in physical, chemical, and biological systems.[6] It plays essential roles in biology,[7–12] sensing[13–18], catalysis,[19–24] and energy materials.[25–32] Marcus laid the foundation of ET theory in 1956.[33,34] Later, experimental studies by Taube[35] and Sutin[6], together with theoretical extensions by Hush,[36] Levich,[37,38] and Jortner,[39,40] greatly advanced this field.

Molecules, as many-particle systems consisting of nuclei and electrons, exhibit behaviors that can be accurately described within the framework of quantum mechanics. Therefore, quantum chemical methods are essential for reliable modeling and property prediction.[41] The approach models electronic behavior through quantum mechanics, enabling the prediction and explanation of molecular energies, structures, and dynamics, and offering a clear basis for understanding the performance of organic photovoltaic materials. Within wavefunction-based methods, the most fundamental approximation is the Hartree–Fock (HF) method. It describes electron–electron interactions with a mean-field approximation and provides a starting point for more accurate correlation treatments such as Møller–Plesset perturbation theory of second order (MP2), Coupled-Cluster with Single and Double excitations (CCSD), and Configuration Interaction (CI). Although HF neglects electron correlation, it remains essential in modeling and understanding electronic structures.[42,43] Another mainstream approach is density functional theory (DFT), which replaces the many-electron wavefunction with electron density as the fundamental variable, thereby reducing computational complexity. With properly chosen exchange–correlation functionals, DFT offers a good

balance between accuracy and efficiency for ground-state properties.[44–47] Furthermore, time-dependent density functional theory (TDDFT) extends the DFT formalism to the time domain, enabling the description of excited-state properties, optical absorption spectra, and photochemical processes with reasonable computational cost.[48,49] In Chapter 2, these quantum chemical methods are introduced and derived.

Triphenylamine (**TPA**) possesses multiple advantages that make it a potential core building block for photovoltaic materials. First, its easy chemical modification offers the possibility for designing and synthesizing new materials. Second, the propeller-like framework of **TPA** allows for diverse aggregation states, enabling tunable solid-state properties. Its strong electron-donating character also facilitates the modulation of optical and electronic behavior, while the efficient hole-transporting ability enhances overall charge transfer. These features make **TPA** a versatile platform adaptable to different types of solar cells, including organic, dye-sensitized, and perovskite devices.[50–53] Since the earliest studies of its photochemical properties, it has been shown that under photoexcitation **TPA** tends to undergo ring closure to form carbazole derivatives. This reaction has been widely investigated in both polar and nonpolar solvents. However, in chloroform, **TPA** derivatives display distinctive behavior, attributable to their strong electron-donating character. In Chapter 3, the photoexcitation reactions of **TPA** and dimethylmethylene-bridged derivative **DTPA** in chloroform are examined.

In organic optoelectronic materials, electron transfer takes place not only in isolated molecular systems but also within molecular aggregates. Organic semiconductors are organic materials that exhibit semiconducting properties. The main physical parameter that describes charge transport in these materials is the charge mobility, denoted as μ. Depending on how easily charges can be injected from the electrodes, organic semiconductors can be divided into two types. When the Fermi level of an electrode is close to the electron affinity of the material, electrons are easily injected, and the material is called an n-type semiconductor. In contrast, when the ionization energy of the material is close to the Fermi level of the electrode, it mainly transports holes and is known as a p-type semiconductor.[41,54]

Although significant progress has been achieved, most studies on charge carrier mobility in organic semiconductors remain limited to one- or two-dimensional transport anisotropy, which cannot fully describe the relationship between molecular packing and charge transport in crystals with an inherently three-dimensional (3D) nature.[55,56] To overcome these limitations, a 3D mobility model based on Marcus–Hush theory combined with quantum chemical calculations offers a quantitative framework for elucidating the orientation dependence of transport pathways. Huang et al. introduced an orientation function to describe the mobility in a specific conducting direction on a specific surface in organic single crystal. Here, γ is the angle of intermolecular hopping relative to the plane of interest, Φ is the orientation angle of the transistor channel with respect to a reference axis (often a crystal axis), and θ is the projection angle of the electronic coupling pathway of a specific dimer relative to the same axis. Thus, the relative angle between a given hopping pathway and the conducting channel is expressed as $(\theta - \Phi)$ (As shown in Figures 1.1). The mobility along a specific conducting direction on the surface of an organic single crystal is then described as:

$$\mu(\gamma, \Phi) = \frac{e}{2nk_BT} \sum_i W_i \, {r_i}^2 P_i \cos^2(\gamma_i) \cos^2(\theta_i - \Phi), \tag{1.1}$$

here, $P_i \cos^2 \gamma_i \cos^2(\theta_i - \Phi)$ describes the relative hopping probability of different dimer types in the conducting channel. r_i, γ_i, and θ_i are determined by the molecular packing geometry of the organic crystal.[57] However, equation 1.1 could not account for the contribution of polar angles.

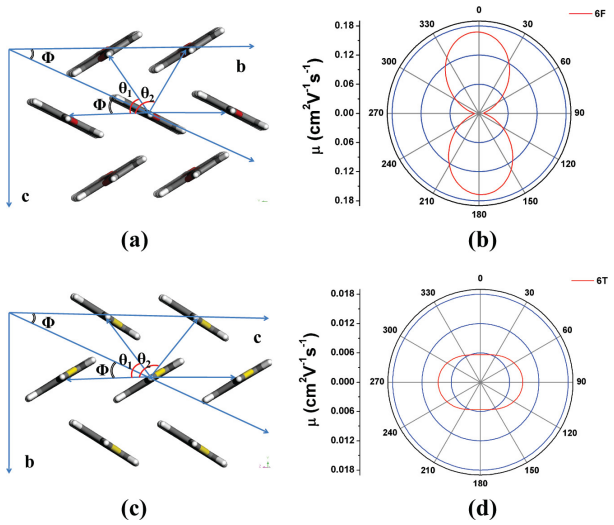

Figure 1.1: (a) and (c) Different hopping paths projecting to a transistor channel in the a–b plane of **6F** and **6T** single crystals respectively. For **6F** (**6T**), θ_1 and θ_2 are the angles of T1 and T2 dimers relative to the reference crystallographic axis b (c); Φ is the angle of a conduction channel relative to the reference crystallographic axis b (c). (b) and (d) Calculated angle resolved anisotropic hole mobility of **6F** and **6T**, respectively.[57]

In 2023, the electronic structures and three-dimensional angle-resolved anisotropic mobilities of **6-CH**, **6-EH**, and **6-DIPP** were first investigated (Figures 1.2). Both **6-EH** and **6-CH** exhibited typical n-type charge transport characteristics, with mobilities as high as 1.45 and 0.31 $cm^2 \cdot V^{-1} \cdot s^{-1}$, respectively. The predicted anisotropic mobility range of **6-EH** was consistent with the reported values in organic field-effect transistor (OFET) devices.[58]

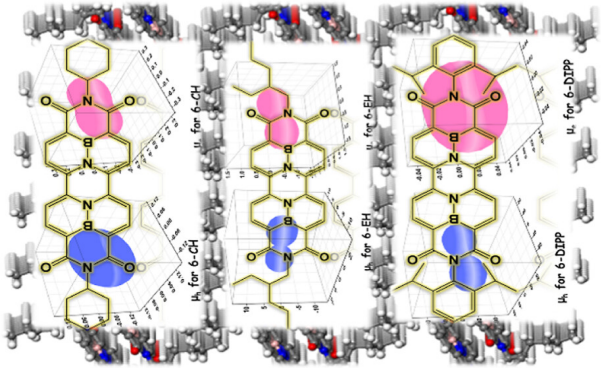

Figure 1.2: Calculated angle-resolved anisotropic hole and electron mobility values in 3D space for **6-CH**, **6-EH**, and **6-DIPP**.[58]

The three-dimensional anisotropic mobilities in **BTBT** and its derivatives were studied, and the optimal conducting channels relative to the crystal axes were identified, providing a reliable reference for optimizing OFET performance (Figures 1.3). Notably, **–COPHF** substitution was found to enhance electron affinities and significantly narrow the HOMO–LUMO gaps, which can help reduce electron injection barriers and improve optical absorption. This provides a promising approach for converting p-type semiconductors into ambipolar or n-type semiconductors.[59]

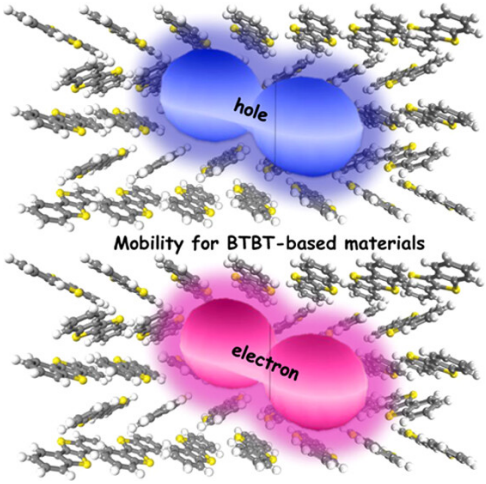

Figure 1.3: Calculated angle-resolved anisotropic hole and electron mobility values in 3D space for **BTBT**.[59]

Therefore, the three-dimensional mobility modeling method, based on Marcus–Hush theory combined with crystallography, provides a quantitative approach to understand the transport pathways, carrier mobilities, and spatial dependence of device performance in organic materials. However, in both of the above studies, no explicit formula for calculating the three-dimensional charge carrier mobility was provided. Inspired by these reports, instead of using $P_i \cos^2 \gamma_i \cos^2(\theta_i - \Phi)$, the projection function between two unit vectors in spherical coordinates was adopted, which can be expressed as:

$$Q(\gamma, \theta) = \sin \gamma_i \sin \gamma \cos(\theta_i - \theta) + \cos \gamma_i \cos \gamma. \tag{1.2}$$

Then a more specific physical meaning of the three-dimensional charge mobility equation would be given as:

$$\mu(\gamma, \theta) = \frac{e}{2nk_BT} \sum_i W_i r_i^2 P_i Q^2(\gamma, \theta) \tag{1.3}$$

$$= \frac{e}{2nk_BT} \sum_i W_i r_i^2 P_i \Big[\sin \gamma_i \sin \gamma \cos(\theta_i - \theta) + \cos \gamma_i \cos \gamma\Big]^2. \tag{1.4}$$

The detailed derivation can be found in the following chapter, Theoretical Methods. By using equation 1.4, in Chapter 4, the polar angle γ and the azimuthal angle θ are introduced to establish a 3D charge transport model. The mobilities of Triisopropylsilyl-tetraazapentacene (**TIPS-TAP**) derivatives, **4Br-TIPS-TAP** and **4I-TIPS-TAP**, are systematically investigated as bromine- and iodine-substituted compounds.

In designing high-performance materials, singlet fission is considered an effective strategy for improving light energy conversion efficiency. The dipyrrolonaphthyridinedione derivative (**DPND6**) features a pyrrole-fused, cross-conjugated skeleton with distinctive adaptive (dual) aromatic character. This unique electronic framework not only stabilizes the excited states but also promotes highly efficient singlet fission, yielding triplet excitons with efficiencies as high as 173%. Although the dynamics of the excited-state of **DPND** derivatives in SF have been widely studied,[60,61] how to further investigate the charge mobility of them remains a key challenge. In Chapter 5, the investigation of the 3D charge transport model is extended to (**DPND**)-type molecules which undergo singlet fission, in particular **DPND** and its alkylated derivative **DPND6**. For the first time, we theoretically evaluate their anisotropic electron and hole mobilities.

Chapter 2

Theoretical Methods

2.1 Basic concepts

2.1.1 The Schrödinger Equation

The Schrödinger equation, proposed by physicist Erwin Schrödinger in 1926, is one of the fundamental equations of quantum mechanics. It provides us with a mathematical framework for describing the behavior of particles, such as electrons, atoms, and molecules. The Schrödinger equation can be written as:[62]

$$\hat{H}\Psi = E\Psi, \tag{2.1}$$

where $\hat{H}$ denotes the Hamiltonian operator, which includes the kinetic and potential energy, Ψ represents the wave function, and E is the energy of the system. The Hamiltonian is defined as:

$$\hat{H} = -\sum_{i=1}^{N}\frac{1}{2}\nabla_i^2 - \sum_{A=1}^{M}\frac{1}{2M_A}\nabla_A^2 - \sum_{i=1}^{N}\sum_{A=1}^{M}\frac{Z_A}{r_{iA}} + \sum_{i=1}^{N}\sum_{j>i}^{N}\frac{1}{r_{ij}} + \sum_{A=1}^{M}\sum_{B>A}^{M}\frac{Z_A Z_B}{R_{AB}}, \tag{2.2}$$

in this equation, M_A is the ratio of the mass of nucleus A to the mass of an electron, and Z_A represents the atomic number of nucleus A. The Laplacian operators ∇_i^2 and ∇_A^2 correspond to differentiation with respect to the coordinates of the i-th electron and the A-th nucleus, respectively. This equation can also be briefly summed up as:

$$\hat{H} = \hat{T}_{ele} + \hat{T}_{nuc} + \hat{V}_{ele-nuc} + \hat{V}_{ele-ele} + \hat{V}_{nuc-nuc}, \tag{2.3}$$

here, $\hat{T}_{ele}$ and $\hat{T}_{nuc}$ correspond to the kinetic energy operators for electrons and nuclei, respectively. The term $\hat{V}_{ele\text{-}nuc}$ represents the Coulomb attraction, while $\hat{V}_{ele\text{-}ele}$ and $\hat{V}_{nuc\text{-}nuc}$ describe the electron–electron and nucleus–nucleus repulsions, respectively.[42]

2.1.2 The Born-Oppenheimer Approximation

The Born-Oppenheimer approximation is an important theoretical assumption in quantum chemistry and molecular physics, proposed by Max Born and J. Robert Oppenheimer in 1927.[63] For a many-particle system consisting of N electrons and M nuclei, the stationary Schrödinger equation for the Hamiltonian can be generally written as:

$$\hat{H}\,\Psi(x_1, x_2, \ldots, x_N; R_1, R_2, \ldots, R_M) = E\,\Psi(x_1, x_2, \ldots, x_N; R_1, R_2, \ldots, R_M), \tag{2.4}$$

where the total wave function depends on as many as $3(N+M)$ spatial variables. The computational complexity of solving this equation scales directly with the total number of particles, making exact solutions for most realistic systems extremely challenging or practically impossible.

Since the motion of electrons is much faster than that of atomic nuclei, and the mass of an electron is much smaller than that of a nucleus (approximately 1/1836 the mass of a proton), the electrons can rapidly adjust to their equilibrium state while the positions of the nuclei remain nearly fixed. Therefore, the motion of electrons and nuclei can be decoupled, reducing the variables of the wave function in the many-body problem from $3(N+M)$ to $3N$. Thus we have:

$$\hat{H}\,\Psi(x_1, x_2, \ldots, x_N) = E\,\Psi(x_1, x_2, \ldots, x_N). \tag{2.5}$$

The total molecular wave function can be approximately expressed as the product of the electronic wave function and the nuclear wave function, simplifying the complex many-body problem into two relatively simpler parts.

$$\Psi(R, r) \approx \psi_{\text{ele}}(r; R) \cdot \chi_{\text{nuc}}(R), \tag{2.6}$$

where *R* denotes the set of nuclear coordinates, *r* denotes the set of electronic coordinates, ψ_{ele} is the electronic wavefunction solved at fixed nuclear coordinates, and χ_{nuc} is the nuclear wavefunction describing the motion of the nuclei. This greatly enhances computational efficiency. The electronic Hamiltonian under the Born-Oppenheimer approximation can be written as:[42]

$$\hat{H}_e = -\sum_{i=1}^{N} \frac{1}{2}\nabla_i^2 - \sum_{i=1}^{N}\sum_{A=1}^{M} \frac{Z_A}{r_{iA}} + \sum_{i=1}^{N}\sum_{j>i}^{N} \frac{1}{r_{ij}}, \tag{2.7}$$

However, the third term on the right-hand side of the equation above (the electron–electron Coulomb term) cannot be separated into independent variables. This necessitates the use of various approximations, which leads to different theoretical methods in quantum chemical calculations.

2.2 The Hartree-Fock Approximation

Due to the Coulomb interactions among electrons, directly solving the Schrödinger equation for many-electron systems is mathematically intractable. To address this challenge, the Hartree–Fock (HF) approximation was developed.[64] In this method, each electron is treated as moving independently in an average potential generated by the nuclei and the other electrons. This approach reduces the complex many-electron problem to a series of equations for individual electrons. The total wavefunction is then approximated as a product of these single-electron wavefunctions, called the Hartree product, which helps to understand the electronic structure of molecules in their ground state.

Mathematically, the Hartree product can be written as:

$$\Psi_n^{\text{HP}} = \chi_1(X_1)\chi_2(X_2)\ldots\chi_n(X_n), \tag{2.8}$$

where Ψ_n^{HP} is the many-electron wavefunction of the system. The $\chi_n(X_n)$ denotes the spin orbital, which is the product of a spatial orbital $\phi_n(r)$ and the α or β spin function:

$$\chi_n(X_n) = \phi_n(r)\alpha(s), \tag{2.9}$$

$$\chi_n(X_n) = \phi_n(r)\beta(s), \tag{2.10}$$

where X_n denotes both the spatial and spin coordinates of the *n*-th electron.

However, since electrons are fermions, they must satisfy the Pauli exclusion principle. The Hartree product cannot guarantee this requirement, so the Slater determinant was introduced to construct a multi-electron wavefunction that satisfies the antisymmetry requirement. For a system containing N electrons, the Slater determinant can be expressed as:

$$\Psi(X_1, X_2, \ldots, X_N) = \frac{1}{\sqrt{N!}} \begin{vmatrix} \psi_1(X_1) & \psi_1(X_2) & \cdots & \psi_1(X_N) \\ \psi_2(X_1) & \psi_2(X_2) & \cdots & \psi_2(X_N) \\ \vdots & \vdots & \ddots & \vdots \\ \psi_N(X_1) & \psi_N(X_2) & \cdots & \psi_N(X_N) \end{vmatrix}, \tag{2.11}$$

here, $\psi_i(X_j)$ spcifies the i-th spin orbital evaluated at the position X_j of the j-th electron. $\frac{1}{\sqrt{N!}}$ is the normalization factor.

The short-hand notation for a normalized Slater determinant is:

$$\Psi(X_1, X_2, \ldots, X_N) = |\chi_1 \chi_2 \cdots \chi_N\rangle. \tag{2.12}$$

When exchanging any two electrons (for example, the *i*-th electron and *j*-th electron), the determinant will change sign.[42]

$$|\ldots \chi_i \cdots \chi_j \ldots\rangle = -|\ldots \chi_j \cdots \chi_i \ldots\rangle. \tag{2.13}$$

2.2.1 Hartree-Fock Equation

With the Slater determinant wavefunction, the Hamiltonian can be simplified by defining one-electron and two-electron operators and their corresponding integrals. The one-electron operator $\hat{h}(r_i)$ describes the kinetic energy of an electron and its attraction to the nuclei:

$$\hat{h}(r_i) = -\frac{1}{2}\nabla_i^2 - \sum_A \frac{Z_A}{r_{iA}}, \tag{2.14}$$

here, ∇_i^2 is the Laplacian operator for the i-th electron, Z_A is the nuclear charge of atom A, and r_{iA} is the distance between the i-th electron and nucleus A. The corresponding one-electron integral is:

$$\langle i|\hat{h}|j\rangle = \int \phi_i^*(r)\hat{h}(r)\phi_j(r)\, dr, \tag{2.15}$$

for two-electron interactions, the Coulomb operator $\nu(i, j)$ represents the repulsion between electrons:

$$\nu(i, j) = \frac{1}{r_{ij}}, \tag{2.16}$$

where r_{ij} is the distance between electron i and electron j. The two-electron integrals are defined as:

$$\langle ij|kl\rangle = \int\int \phi_i^*(r_1)\phi_j^*(r_2)\frac{1}{r_{12}}\phi_k(r_1)\phi_l(r_2)\, dr_1\, dr_2, \tag{2.17}$$

the antisymmetrized two-electron integral, accounting for exchange effects, is:

$$\langle ij||kl\rangle = \langle ij|kl\rangle - \langle ij|lk\rangle. \tag{2.18}$$

Using these integrals, the Hartree-Fock energy E_{HF} is expressed as:

$$E_{HF} = \sum_i \langle i|h|i\rangle + \frac{1}{2}\sum_{ij}\langle ij||ij\rangle. \tag{2.19}$$

To derive the Hartree-Fock equations, the Lagrangian $\mathcal{L}_{(\chi_i)}$ with Lagrange multipliers ϵ_{ij} is constructed to enforce orthonormality constraints:

$$\mathcal{L}_{(\chi_i)} = E_{HF(\chi_i)} - \sum_{ij}\epsilon_{ij}\left(\langle\chi_i|\chi_j\rangle - \delta_{ij}\right). \tag{2.20}$$

Setting the first variation of the Lagrangian to zero ($\mathcal{L}_{(\chi_i)}$ = 0) yields the Hartree-Fock integro-differential equations:

$$\hat{h}(1)\chi_i(1) + \sum_{j\neq i}\left[\int dx_2\,|\chi_j(2)|^2\frac{1}{r_{12}}\right]\chi_i(1) - \sum_{j\neq i}\left[\int dx_2\,\chi_j^*(2)\chi_i^*(2)\frac{1}{r_{12}}\right]\chi_j(1) = \epsilon_i\,\chi_i(1). \tag{2.21}$$

To simplify this formulation, the Fock operator $\hat{f}(1)$ is introduced, which combines the one-electron Hamiltonian $\hat{h}(1)$, the Coulomb operator:

$$\mathcal{J}_j(1) = \int dx_2\,\chi_j^*(2)r_{12}^{-1}\chi_j(2),$$

and the Exchange operator:

$$\mathcal{K}_j(1) = \int dx_2\,\chi_j^*(2)r_{12}^{-1}\chi_i(2).$$

Thus we have:

$$\hat{f}(1) = \hat{h}(1) + \sum_j \mathcal{J}_j(1) - \mathcal{K}_j(1), \tag{2.22}$$

by expressing the Hartree-Fock equation in terms of the Fock operator, the original integro-differential equation is transformed into a simpler eigenvalue problem:

$$\hat{f}|\chi_i\rangle = \epsilon_i|\chi_i\rangle, \tag{2.23}$$

where ϵ_i denotes the orbital energy of the i-th spin orbital χ_i. This eigenvalue formulation is more convenient for practical calculations and forms the basis of standard Hartree-Fock computational procedures.[42]

2.2.2 Roothan-Hall Equation

The Roothaan–Hall equation is a key formulation in quantum chemistry used to solve the Hartree–Fock equation for molecular systems within the framework of the Linear Combination of Atomic Orbitals (LCAO) approximation. It provides a means to express a molecular orbital (MO) as a linear combination of atomic orbitals (AOs), which are represented by basis functions. This approach allows the electronic structure of molecules to be obtained efficiently in computational chemistry. In the LCAO approach, each molecular orbital ψ_i is expressed as a linear combination of K atomic orbitals ϕ_μ:

$$\psi_i = \sum_{\mu=1}^{K} C_{\mu i}^{*}\, \phi_\mu, \quad i = 1, 2, \ldots, K, \tag{2.24}$$

where $C_{\mu i}$ is an expansion coefficient (to be determined), and ϕ_μ is an atomic orbital basis function. This coefficient is unknown and needs to be determined by solving the Hartree–Fock equation.

The Hartree-Fock equation in the LCAO basis is:

$$\hat{f}(1) \sum_{\nu} C_{\nu i}^{*}\, \phi_\nu(1) = \epsilon_i \sum_{\nu} C_{\nu i}^{*}\, \phi_\nu(1), \tag{2.25}$$

to transform the Hartree-Fock equations into a form suitable for numerical solution, both sides of equation (2.25) are multiplied by the complex conjugate of an atomic orbital, $\phi_\nu^*(1)$, and integrated over the spatial coordinates of electron 1. This procedure leads to the Roothaan equation:

$$\sum_{\nu} F_{\mu\nu}\, C_{\nu i} = \epsilon_i \sum_{\nu} S_{\mu\nu}\, C_{\nu i}, \tag{2.26}$$

here, the matrix elements are defined as follows. The Fock matrix element,

$$F_{\mu\nu} = \int \phi_\mu^*(1) \hat{f}(1) \phi_\nu(1)\, dr_1, \tag{2.27}$$

describes the interaction between atomic orbitals ϕ_μ and ϕ_ν under the influence of the Fock operator. The overlap matrix element,

$$S_{\mu\nu} = \int \phi_\mu^*(1) \phi_\nu(1)\, dr_1, \tag{2.28}$$

quantifies the spatial overlap between the orbitals ϕ_μ and ϕ_ν. Together, equations (2.26)–(2.28) provide a matrix representation of the Hartree–Fock problem, which is well suited for computational implementation. In this framework, the equations can be expressed in the following compact matrix form:

$$\mathbf{FC} = \epsilon \mathbf{SC}. \tag{2.29}$$

From the Roothaan equation, it is evident that $\mathbf{C}$ represents the expansion coefficient for each orbital. Since $\mathbf{C}$ depends on the Fock matrix $\mathbf{F}$, which in turn is constructed from $\mathbf{C}$, the solution requires an iterative approach known as the self-consistent field (SCF) method.[42]

2.3 Density Functional Methods

2.3.1 Density Functional Theory

Density Functional Theory (DFT) is a quantum mechanical method to study the electronic structure of many-body systems. Unlike traditional wavefunction methods, DFT uses the electron density as the central variable and expresses the total energy as a functional of the density. It is mainly applied to efficiently compute the ground-state properties of multi-electron systems. In 1927, Thomas and Fermi proposed a pioneering idea: using the electron density distribution ρ as the basic variable to describe many-body systems, thus avoiding the complicated wavefunction.[65,66] This model provided a new theoretical framework for solving the Schrödinger equation and

is regarded as the precursor of modern DFT. However, due to its neglect of electron–electron interactions and its approximate treatment of kinetic energy, the method proved inadequate for a wide range of systems.

In 1964, Hohenberg and Kohn established the famous Hohenberg–Kohn theorems, which became the foundation of DFT and marked its true beginning. The first theorem states that the total energy of a system is a functional of the electron density. It proves that there is a one-to-one correspondence between the electron density and the external potential $\hat{V}_{ext}(r)$, meaning that the ground-state density uniquely determines the wavefunction and total energy. Therefore, in principle, all physical properties of the system can be derived from the electron density. The second theorem shows that the energy can be written as a functional $E[\rho(r)]$, and its minimum corresponds to the ground-state energy. Thus, the density that yields the lowest energy is the ground-state density.[44]

Since the electron density depends only on spatial coordinates, the number of variables needed to describe a many-electron system is reduced from $3N$ to 3. This dimensional reduction is a key advantage of DFT, as it greatly simplifies the solution of the Schrödinger equation.

In 1965, Kohn and Sham introduced the Kohn–Sham (KS) equations, which provided explicit expressions for the components of the energy functional and enabled the wide application of DFT in practical calculations.[45] The key idea is to map a complex interacting many-body system onto a fictitious non-interacting single-particle system. In this framework, all complicated electron–electron interactions are incorporated into a unified exchange–correlation potential. The basic form of the Kohn–Sham equation is given as:

$$\left[-\frac{1}{2}\nabla_i^2 + \hat{V}_{\mathit{eff}}(r)\right]\psi_i^{KS}(r) = \epsilon_i^{KS}\psi_i^{KS}(r), \tag{2.30}$$

where $\psi_i^{KS}(r)$ is Kohn-Sham orbitals. ϵ_i is orbital energy eigenvalues. $\hat{V}_{\mathit{eff}}(r)$ is effective potential, defined as:

$$\hat{V}_{\mathit{eff}}(r) = \hat{V}_{ext}(r) + \hat{V}_H(r) + \hat{V}_{xc}(r), \tag{2.31}$$

here, $\hat{V}_H(r)$ is Hartree potential which accounts for the classical Coulomb interaction between the electrons. $\hat{V}_{xc}(r)$ is exchange-correlation potential, includes all nontrivial many-body effects.

The SCF procedure is a fundamental iterative method in density functional theory (DFT) used to solve the Kohn-Sham equations. The process begins with an initial guess for the electron density, $\rho(r)$, which serves as the starting point for the calculation. The Kohn-Sham equations are then solved to obtain the single-particle orbitals $\psi_i(r)$. These orbitals are used to update the electron density according to the following equation:

$$\rho(r) = \sum_i |\psi_i(r)|^2. \tag{2.32}$$

This updated electron density is fed back into the Kohn-Sham equations, and the process is repeated iteratively until self-consistency is achieved. Self-consistency is typically defined as the point where the input and output electron densities converge to within a predefined tolerance threshold.[67]

The Kohn-Sham approach is widely regarded as a cornerstone of modern computational chemistry and materials science due to its unique combination of accuracy and computational efficiency. One of its key strengths is its ability to handle large and complex systems, including proteins, nanoparticles, and solid-state materials, making it a versatile tool for both theoretical and applied research. However, the accuracy of the Kohn–Sham method strongly depends on the choice of the exchange–correlation functional. Perdew's "Jacob's ladder" describes the stepwise development from simple approximations to high-level functionals (Figure 2.1).[68–70]

At the first rung, the local spin-density approximation (LSDA) is used. It depends only on the (spin) electron density $\rho(r)$. This approximation is exact for the uniform electron gas (UEG) model but often lacks accuracy

for molecular systems with strongly inhomogeneous densities. To overcome this, the second rung introduces the density gradient $\nabla\rho(r)$, forming the generalized gradient approximation (GGA). Compared with LSDA, GGA better accounts for density inhomogeneity and improves the prediction of molecular properties.

Further improvement comes at the third rung with meta-GGA functionals. These include the Laplacian of the density $\nabla^2\rho(r)$ and/or the kinetic energy density $\tau(r)$ in addition to the GGA terms. Meta-GGAs usually perform better than GGAs in thermochemistry, kinetics (e.g., reaction barriers), and noncovalent interactions.

The fourth rung is hybrid density functionals. They mix a fraction of Hartree–Fock exact exchange with LSDA, GGA, or meta-GGA, leading to hybrid LSDA, hybrid GGA, and hybrid meta-GGA. For example, B3LYP was the first widely used global hybrid in chemistry and remains one of the most popular functionals.[71] Global hybrid (GH) functionals use a fixed portion of exact exchange, while range-separated hybrids (RSH) split exact exchange into short-range (SR) and long-range (LR) parts, usually with the error function erf and the complementary error function erfc(1 - erf):

$$\frac{1}{r_{12}} = \frac{\mathrm{erfc}(\omega r_{12})}{r_{12}} + \frac{\mathrm{erf}(\omega r_{12})}{r_{12}}, \tag{2.33}$$

here, the first term on the right side is singular but short-rang while the second term is non-singular and long-range. This treatment balances short- and long-range interactions.

Finally, the fifth rung involves functionals that, in addition to occupied orbitals (via exact exchange), also include virtual orbital information, such as second-order perturbation theory (MP2) or the random phase approximation (RPA). These double hybrid (DH) functionals are computationally expensive but highly accurate.

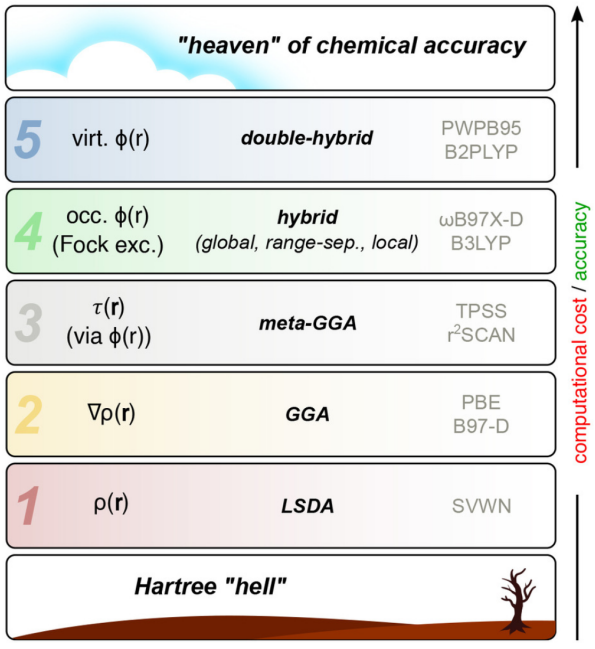

Figure 2.1: Functional categorization according to Perdew's "Jacob's ladder". ρ is electron density, τ is kinetic energy density, ϕ is molecular orbital, Fock exc. is Fock exchange.[70]

2.3.2 Time-Dependent Density Functional Theory

Time-Dependent Density Functional Theory (TDDFT) is an extension of Density Functional Theory that allows the study of time-dependent phenomena in quantum systems.[72] While DFT is a powerful tool for ground-state properties of many-electron systems, TDDFT generalizes the framework to handle time-dependent problems, such as the response to external perturbations (e.g., electromagnetic fields) and excited-state properties.

2.3.2.1 The Runge−Gross Theorem

The Runge–Gross (RG) theorem provides the fundamental basis for time-dependent density functional theory (TDDFT). It states that, for a given initial many-body system, the time-dependent electron density $\rho(r,t)$ uniquely determines the external potential $v_{ext}(r,t)$, so that knowledge of the density alone is sufficient to define the potential. Once the potential is specified, the complete properties of the system can be obtained by solving the time-dependent Schrödinger equation.[48,73]

When introducing a non-interacting auxiliary system affected by an effective local potential $v_{KS}(r,t)$, the RG theorem guarantees that this potential is uniquely defined and ensures that the electron density obtained from the Kohn–Sham orbitals exactly matches that of the interacting system. The Kohn–Sham orbitals obey the following time-dependent Schrödinger equation:

$$i\frac{\partial}{\partial t}\Psi(r,t) = \hat{H}(r,t)\Psi(r,t), \tag{2.34}$$

here, $\Psi(r,t)$ is the time-dependent wavefunction, and $\hat{H}(r,t)$ is the time-dependent Hamiltonian. Analogous to the ground-state Kohn-Sham scheme, the time-dependent Kohn-Sham potential $\hat{V}_{\mathit{eff}}(r,t)$ comprises the external potential $\hat{V}_{ext}(r,t)$, the Hartree potential $\hat{V}_{Hartree}(r,t)$, and the exchange-correlation potential $\hat{V}_{xc}(r,t)$:

$$\hat{V}_{\mathit{eff}}(r,t) = \hat{V}_{ext}(r,t) + \hat{V}_{Hartree}(r,t) + \hat{V}_{xc}(r,t), \tag{2.35}$$

where $\hat{V}_{xc}(r,t)$ is also a functional of the time-dependent electron density $\rho(r,t)$.

2.3.2.2 The Time-Dependent Kohn−Sham Equation

Similar to the time-independent Kohn–Sham equation, transforming an interacting many-body system into a non-interacting system makes the problem more tractable. The non-interacting wavefunction can be written as a Slater determinant of single-particle orbitals, and each orbital is determined by a partial differential equation in a single variable. The kinetic energy of the non-interacting system can be expressed exactly in terms of its orbitals.

For the non-interacting system, there exists an external one-particle potential $v_s(r,t)$ that yields an electron density $\rho_s(r,t)$ identical to the exact electron density $\rho(r,t)$ of the interacting system:

$$\rho(r,t) = \rho_s(r,t) = \sum_i^N |\phi_i(r,t)|^2. \tag{2.36}$$

The single-electron orbitals can be given by the single-electron SE:

$$i\frac{\partial}{\partial t}\,\phi_i(r,t) = \left[-\frac{1}{2}\nabla^2 + v_s(r,t)\right]\phi_i(r,t). \tag{2.37}$$

The time-dependent single-particle potential is:

$$v_s(r,t) = v(r,t) + \int d^3r'\,\frac{\rho(r',t)}{|r-r'|} + \frac{\delta A_{xc}[\rho]}{\delta\rho(r,t)}, \tag{2.38}$$

where A_{xc} is the exchange-correlation part of the action integral.[74] Substituting equation (2.38) into equation (2.37) leads to the explicit form of the time-dependent Kohn-Sham (TDKS) equation:

$$i\frac{\partial}{\partial t}\phi_i(r,t) = \left[-\frac{1}{2}\nabla^2 + v(r,t) + \int d^3r' \frac{\rho(r',t)}{|r-r'|} + \frac{\delta A_{\mathrm{xc}}[\rho]}{\delta\rho(r,t)}\right]\phi_i(r,t), \tag{2.39}$$

which can be compactly written in operator form as

$$i\frac{\partial}{\partial t}\phi_i(r,t) = \hat{F}^{\mathrm{KS}}\,\phi_i(r,t), \tag{2.40}$$

here, $\hat{F}^{\mathrm{KS}}$ is the time-dependent Kohn-Sham operator, which acts on the orbital $\phi_i(r,t)$ and includes four contributions: the kinetic energy operator $-\frac{1}{2}\nabla^2$, the external potential $v(r,t)$, the Hartree potential $\int d^3r' \frac{\rho(r',t)}{|r-r'|}$, and the exchange-correlation potential $\frac{\delta A_{\mathrm{xc}}[\rho]}{\delta\rho(r,t)}$.

In a chosen basis set, for example consisting of M time-independent single-particle functions $\chi_i(r)$,

$$\phi_i(r,t) = \sum_j^M c_{ij}(t)\chi_j(r). \tag{2.41}$$

the time-dependent Kohn–Sham equation can be conveniently expressed in matrix form:

$$i\frac{\partial}{\partial t}\,\mathbf{C} = \mathbf{F}^{\mathrm{KS}}\,\mathbf{C}. \tag{2.42}$$

2.3.2.3 Linear-Response TDDFT Equation

The time-dependent KS approach includes two strategies to compute excitation energies and oscillator strengths, namely real-time TDDFT[73,75] and linear-response TDDFT[74]. The latter is mainly introduced here due to its broader applications. By multiplying the right-hand side of equation 2.40 with $\mathbf{C}^\dagger$ and subtracting its Hermitian conjugate, the Dirac form of the time-dependent Kohn–Sham equation in the density matrix representation is obtained. This equation can be written as:

$$\sum_q (F_{pq}P_{qr} - P_{pq}F_{qr}) = i\frac{\partial}{\partial t}\,\mathbf{P}_{pr}(t). \tag{2.43}$$

The wave function, or equivalently the density matrix in this context, is expressed as the sum of the unperturbed ground state and its first-order time-dependent correction. The same treatment applies to the time-dependent Kohn–Sham Hamiltonian.

$$F_{pq} = F_{pq}^{(0)} + F_{pq}^{(1)}, \tag{2.44}$$

$$P_{pq} = P_{pq}^{(0)} + P_{pq}^{(1)}. \tag{2.45}$$

Substituting equation 2.44 and equation 2.45 into equation 2.43, we obtain:

$$\left(F_{pq}^{(0)}P_{qr}^{(1)} - P_{pq}^{(1)}F_{qr}^{(0)}\right) + \left(F_{pq}^{(1)}P_{qr}^{(0)} - P_{pq}^{(0)}F_{qr}^{(1)}\right) = i\frac{\partial}{\partial t}\,P^{(1)}. \tag{2.46}$$

After a series of transformations, the matrix form of the non-Hermitian eigenvalue equation in the LR-TDDFT method can be given:

$$\begin{bmatrix}\mathbf{A} & \mathbf{B}\\ \mathbf{B}^* & \mathbf{A}^*\end{bmatrix}\begin{bmatrix}\mathbf{X}\\ \mathbf{Y}\end{bmatrix} = \omega\begin{bmatrix}\mathbf{1} & \mathbf{0}\\ \mathbf{0} & -\mathbf{1}\end{bmatrix}\begin{bmatrix}\mathbf{X}\\ \mathbf{Y}\end{bmatrix}, \tag{2.47}$$

where ω is the corresponding excitation energy. The matrix elements of $\mathbf{A}$ and $\mathbf{B}$ are:

$$A_{ia,jb} = \delta_{ij}\delta_{ab}(\epsilon_a - \epsilon_i) + (ia|jb) + (ia|f_{\text{xc}}|jb), \tag{2.48}$$

$$B_{ia,jb} = (ia|bj) + (ia|f_{\text{xc}}|bj), \tag{2.49}$$

If the de-excitation term $\mathbf{B}$ is neglected, the Tamm–Dancoff approximation (TDA) is obtained, which leads to a Hermitian eigenvalue equation:

$$\mathbf{AX} = \omega\mathbf{X}. \tag{2.50}$$

The Tamm–Dancoff approximation (TDA) is a simplification of TDDFT. TDA reduces the computational cost. For molecular systems with the triplet instability problem, TDDFT often gives excitation energies lower than experiment, while TDA shows no significant deviation.[76]

2.4 Solvation Models

External conditions, such as temperature, pressure, and solute–solvent interactions, can significantly affect molecular free energy, conformational changes, and the physicochemical properties of atomic or molecular systems.[77,78] In quantum chemical calculations for solution phases, the Continuum Solvation Model (CSM) is an efficient and practical approach to account for solvent effects. The core idea is to approximate the solvent as a continuous medium with a uniform dielectric constant, thus avoiding explicit simulation of each solvent molecule. The Integral Equation Formalism Polarizable Continuum Model (IEFPCM) is a mathematically rigorous and widely used implementation of this method. It represents the solvent polarization response as an induced surface charge distribution on the cavity boundary of the solute.[78,79]

2.4.1 Theoretical Framework of the IEFPCM

In IEFPCM, the solute is placed in a dielectric medium with permittivity $\varepsilon(r)$. The electrostatic potential $V(r)$ satisfies the general Poisson equation:

$$\nabla \cdot [\epsilon(r)\nabla V(r)] = -4\pi\rho(r), \tag{2.51}$$

where ρ is the total charge density. ϵ is dielectric constant. Inside the cavity, $\varepsilon = 1$, and the equation reduces to:

$$-\nabla^2 V(r) = 4\pi\rho(r). \quad \text{(Inside cavity } C\text{)} \tag{2.52}$$

Outside the cavity, equation 2.51 can be simplified to:

$$-\epsilon\nabla^2 V(r) = 0, \quad \text{(Outside cavity } C\text{)} \tag{2.53}$$

the total potential V is composed of two parts: the electrostatic potential V_M, generated by the charge distribution ρ_M, and the reaction potential V_R, resulting from the polarization of the dielectric medium.

$$V(x) = \int_{R^3} G^s(x,y)\rho_M(y)\,dy, \tag{2.54}$$

$$V_M(x) = \int_{R^3} G(x,y)\rho_M(y)\,dy, \tag{2.55}$$

$$V_R(x) = \int_{R^3} G^R(x,y)\rho_M(y)\,dy, \tag{2.56}$$

$$G^R(x,y) = G^s(x,y) - G(x,y). \tag{2.57}$$

According to the boundary conditions, the electric potential and normal displacement are required to be continuous, we have:

$$[V] = V_{\text{in}} - V_{\text{out}} = 0. \tag{2.58}$$

The second jump condition concerns the discontinuity in the field component that is represented as the gradient of V and is perpendicular to the cavity.

$$\partial V = \left.\frac{\partial V}{\partial \mathbf{n}}\right|_{\text{in}} - \epsilon \left.\frac{\partial V}{\partial \mathbf{n}}\right|_{\text{out}} = 0, \tag{2.59}$$

where $\mathbf{n}$ is the outward-pointing vector perpendicular to the cavity.

$$V_R(x) = \int_\Gamma \frac{\sigma(y)}{|x-y|} dy. \tag{2.60}$$

Using the integral equation formulation based on the single-layer potential operator S, the double-layer potential operator D, and the adjoint double-layer potential operator D^*, a linear system for determining σ is obtained:[78,80]

$$A\sigma = g, \tag{2.61}$$

$$A = (2\pi - D_e)\, S_i + S_e\,(2\pi + D_i^*)\,, \tag{2.62}$$

$$g = (2\pi - D_e)\, V_M + S_e \left(\frac{\partial V_M}{\partial n}\right), \tag{2.63}$$

in the last two relationships we have introduced the operators S_a, D_a, and D_a^* with $a \in \{e, i\}$ denoting external (e, outside the cavity) and internal (i, inside the cavity), respectively.[79]

$$(S_a\sigma)(x) = \int_\Gamma G_a(x,y)\sigma(y)dy, \tag{2.64}$$

$$(D_a\sigma)(x) = \int_\Gamma \left[\epsilon_a \nabla_y G_a(x,y)\cdot \mathbf{n}(y)\right]\sigma(y)dy, \tag{2.65}$$

$$(D_a^*\sigma)(x) = \int_\Gamma \left[\epsilon_a \nabla_x G_a(x,y)\cdot \mathbf{n}(x)\right]\sigma(y)dy, \tag{2.66}$$

after obtaining σ, the reaction field potential V_R can be constructed, yielding the total potential:

$$V_{total}(x) = V_M(x) + V_R(x), \tag{2.67}$$

$$(H_0 + V_R)\Psi = E\Psi, \tag{2.68}$$

where H_0 is the standard Hamiltonian of the molecule in vacuum (without solvent), and V_R depends on the solute electron density ρ_M and must be solved self-consistently with the wavefunction.

The method effectively reduces the three-dimensional Poisson equation solution to a two-dimensional integral equation over the molecular surface, significantly decreasing computational complexity while accurately capturing solvent polarization effects on both electronic structure of solute and solvation free energy.

2.5 Electron transfer

2.5.1 Marcus–Hush theory

The Marcus–Hush theory is introduced starting with the two-parabolic free-energy surface model. Within the harmonic approximation the Gibbs free energies of the donor (1) and acceptor (2) diabatic states along the reaction coordinate x are (Figure 2.2):

$$G_1(x) = G_1^0 + k_1(x - x_1)^2, \tag{2.69}$$

$$G_2(x) = G_2^0 + k_2(x - x_2)^2, \tag{2.70}$$

The activation free energy $\Delta G^\ddagger$ is:

$$\Delta G^\ddagger = k(x^\ddagger - x_1)^2. \tag{2.71}$$

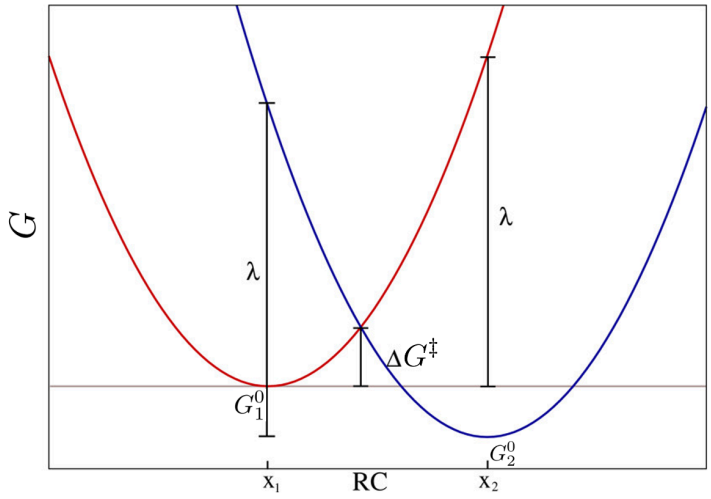

Figure 2.2: Idealized parabolic potential energy surfaces (PES) of reactants ($G_1(x)$, red) and products ($G_2(x)$, blue) in an electron self-exchange process. The two parabolas have the same curvature near their respective local minima (x_1 and x_2).[6]

To get intersection by solving the quadratic in x, we have:

$$G_2(x) - G_1(x) = (k_2 - k_1)x^2 - 2(k_2x_2 - k_1x_1)x + \left(G_2^0 - G_1^0 + k_2x_2^2 - k_1x_1^2\right) = 0. \tag{2.72}$$

The analytical solution is:

$$x_\pm = \frac{k_2x_2 - k_1x_1 \pm \sqrt{\Delta G^0(k_1 - k_2) + k_1k_2(x_2 - x_1)^2}}{k_2 - k_1}, \tag{2.73}$$

in the symmetric-curvature limit $k_1 = k_2 \equiv k$ (or by taking $k_1 \to k_2$ with a controlled small-parameter expansion), the feasible solutions substituted into eqation 2.71 lead directly to the expression for the classical free-energy barrier:[6,81]

$$\Delta G^\ddagger = \frac{(\lambda + \Delta G^0)^2}{4\lambda}, \tag{2.74}$$

where ΔG^0 is driving force, given by:

$$\Delta G^0 = G_2^0 - G_1^0, \tag{2.75}$$

and λ is the reorganization energy, given by:

$$\lambda = k(x_2 - x_1)^2. \tag{2.76}$$

To obtain the rate constant we insert the activation free energy into Fermi's golden rule, yielding the electron transfer rate:[82,83]

$$W_{if} \;=\; \frac{2\pi}{\hbar}\,|J_{if}|^2\,\frac{1}{\sqrt{4\pi\lambda k_B T}}\,\exp\!\left[-\frac{(\Delta G^0+\lambda)^2}{4\lambda k_B T}\right], \tag{2.77}$$

where $\hbar$ is the reduced Planck constant, J_{if} represents the electronic coupling between molecule i to molecule f, λ is the reorganization energy, k_B is the Boltzmann constant, T is the absolute temperature, ΔG^0 is the standard free energy change of the reaction. As shown by the formula, at a given temperature T, a large electronic coupling and a small reorganization energy result in a high transfer rate k.

In the thermoneutral case $\Delta G^0 = 0$, equation 2.77 reduces to:

$$W_{if} = \frac{J_{if}^2}{\hbar}\sqrt{\frac{\pi}{\lambda k_B T}}\exp\!\left(-\frac{\lambda}{4k_B T}\right), \tag{2.78}$$

which is widely used to describe electron transfer:[31,34,82,84–86]

2.5.2 Reorganization energy

The reorganization energy λ was calculated using the four-point method.[85] This energy represents the structural relaxation associated with electron or hole transfer and can be decomposed into contributions from changes in geometry of the neutral and charged species.

For the total electron reorganization energy λ_e, we have:

$$\lambda_e = \lambda_{e1} + \lambda_{e2}, \tag{2.79}$$

where the reorganization energy of the neutral state is:

$$\lambda_{e1} = E_{(M^-)} - E_{(M)}, \tag{2.80}$$

the reorganization energy of the anionic state is as follows:

$$\lambda_{e2} = E^-_{(M)} - E^-_{(M^-)}, \tag{2.81}$$

$E_{(M)}$ is the energy of the neutral state at its optimized geometry, $E_{(M^-)}$ is the energy of the neutral state at the optimized anionic geometry, $E^-_{(M^-)}$ is the energy of the anionic state at the optimized anionic geometry, and $E^-_{(M)}$ is the energy of the anionic state at the optimized neutral geometry. These contributions are illustrated in Figure 2.3.

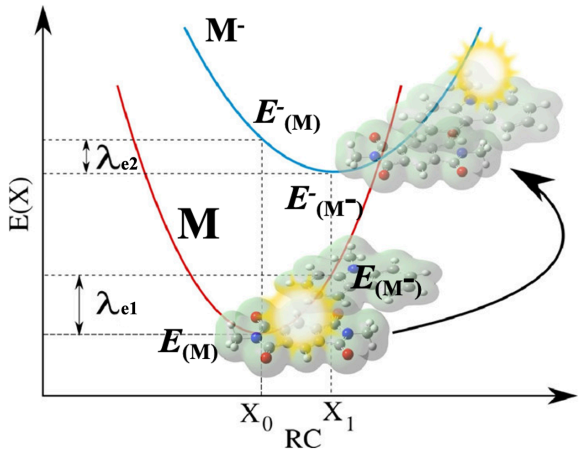

Figure 2.3: Sketch of the potential energy surfaces (PESs) for the neutral state E and anionic state E^-. λ_1 and λ_2 represent the two contributions to the intramolecular reorganization energy.[41,85]

Similarly, for the total hole reorganization energy:

$$\lambda_h = \lambda_{h1} + \lambda_{h2}, \tag{2.82}$$

where the reorganization energy of the neutral state is:

$$\lambda_{h1} = E_{(M^+)} - E_{(M)}, \tag{2.83}$$

the reorganization energy of the cationic state is as follows:

$$\lambda_{h2} = E^+_{(M)} - E^+_{(M^+)}. \tag{2.84}$$

In this case, $E_{(M)}$ is the energy of the neutral state at its optimized geometry, $E_{(M^+)}$ is the energy of the neutral state at the optimized cationic geometry, $E^+_{(M^+)}$ is the energy of the cationic state at the optimized cationic geometry, and $E^+_{(M)}$ is the energy of the cationic state at the optimized neutral geometry. Together, these terms provide a complete picture of the intramolecular reorganization energy for electron and hole transport.

In some reports, the normal-mode (NM) analysis is also used to calculate the reorganization energy. The vibrational modes are included in λ which can be calculated by using DUSHIN.[87]

$$\lambda = \sum_\kappa \lambda_\kappa = \sum_\kappa \frac{1}{2} k_\kappa \Delta Q_\kappa^2, \tag{2.85}$$

where k_κ is the force constant for corresponding mode. ΔQ_κ represents the displacement between the neutral and charged molecules.[88]

2.5.3 Electronic Coupling

Organic semiconductors have broad prospects in optoelectronic devices due to their tunability and processability. To promote its practical application, it is necessary to deeply understand the charge transport mechanism from the fundamental to the device level, that is, how electrons or holes migrate between these organic molecules, as it directly determines the performance of the device.

Electron-electron and electron-phonon interactions and electron-phonon interactions can be effectively interpreted using the tight-binding approximation.

$$H = \sum_m \epsilon_m a_m^+ a_m^- + \sum_{m \neq n} t_{mn} a_m^+ a_n^-, \tag{2.86}$$

this Hamiltonian describes a tight-binding model, commonly used to study electron behavior in molecular, crystalline, or other periodic structures.[54]

The first term, $\sum_m \epsilon_m a_m^+ a_m^-$, represents the energy contribution from electrons localized at their respective sites. Here, a_m^+ and a_m^- are the creation and annihilation operators for site m. The creation operator a_m^+ adds an electron to site m (if the site was unoccupied, it becomes occupied after this operation), while the annihilation operator a_m^- removes an electron from site m (if the site was occupied, it becomes empty; if it was already empty, the result is zero). The combination $a_m^+ a_m^-$ first attempts to remove an electron from site m and then recreates it. The key point is that this combination only yields a non-zero result when site m was originally occupied.

The second term, $\sum_{m \neq n} t_{mn} a_m^+ a_n^-$, describes the energy contribution from electron hopping between different sites, reflecting electron delocalization or mobility. Here, t_{mn} is the transfer integral (electronic coupling), representing the strength of electron hopping from site n to site m. The operator $a_m^+ a_n^-$ removes an electron from site n and creates one at site m, thus describing electron hopping through the molecular or crystal lattice. This term is central to the tight-binding model, as it determines the system's dynamical properties, such as conductivity and band structure.

The Highest Occupied Molecular Orbital (HOMO) and the Lowest Unoccupied Molecular Orbital (LUMO) are key frontier orbitals that largely determine the electronic properties and reactivity of a molecule.[89] Assuming that HOMO and HOMO-1 of the dimer are produced only by the interaction of the monomer HOMO, the orbital energies of the dimer can be described by the following secular equation:

$$\mathbf{HC} = E\mathbf{SC}, \tag{2.87}$$

where $\mathbf{H}$ is the system Hamiltonian in the basis of monomer HOMOs:

$$\mathbf{H} = \begin{pmatrix} e_1 & J_{12} \\ J_{12} & e_2 \end{pmatrix}, \tag{2.88}$$

$\mathbf{S}$ is the overlap matrix in the basis of monomer HOMOs:

$$\mathbf{S} = \begin{pmatrix} 1 & S_{12} \\ S_{12} & 1 \end{pmatrix}, \tag{2.89}$$

$$e_i = \langle \Psi_i | \hat{H} | \Psi_i \rangle, \tag{2.90}$$

$$J_{ij} = \langle \Psi_i | \hat{H} | \Psi_j \rangle. \tag{2.91}$$

The matrix elements e_i and J_{ij} carry the same physical interpretations as the parameters ε and t_{ij} in equation (2.86). However, the two sets of parameters are not directly equivalent. Specifically, while the monomer orbitals Ψ used to define e and J_{ij} are non-orthogonal, equation (2.86) are expressed in an orthonormal basis.

To bridge this gap, a Löwdin symmetric orthogonalization can be applied to transform the original monomer orbitals into an orthogonal set, while preserving as much of their local character as possible. In this symmetrically orthonormalized basis, equation (2.88) takes the following form:[90]

$$\mathbf{H}^{eff} = \begin{pmatrix} e_1^{eff} & J_{12}^{eff} \\ J_{12}^{eff} & e_2^{eff} \end{pmatrix}, \tag{2.92}$$

$$e_{1(2)}^{eff} = \frac{1}{2}\frac{(e_1 + e_2) - 2J_{12}S_{12} \pm (e_1 - e_2)\sqrt{1 - S_{12}^2}}{1 - S_{12}^2}, \tag{2.93}$$

$$J_{12}^{eff} = \frac{J_{12} - \frac{1}{2}(e_1 + e_2)S_{12}}{1 - S_{12}^2}. \tag{2.94}$$

2.5.4 Charge Carrier Mobility

According to Marcus–Hush theory, electron transfer rate W can be calculated by inserting the electronic coupling and the reorganization energy into equation (2.78). Then, the diffusion coefficient D is obtained from W:

$$D \approx \frac{1}{2n} r_i^2 W_i P_i, \tag{2.95}$$

$$\tag{2.96}$$

where P_i is the hopping probability:

$$P_i = \frac{W_i}{\sum_i W_i}. \tag{2.97}$$

Based on the Einstein relation, the mobility can be expressed as:[54]

$$\mu = \frac{eD}{k_B T}, \tag{2.98}$$

where e is the elementary charge (1.602×10^{-19} C), D is the diffusion coefficient (m^2s^{-1}), k_B is the Boltzmann constant (1.381×10^{-23} J/K), T is the absolute temperature (K). To calculate the three-dimensional anisotropic charge mobility, Huang et al. introduced an orientation function to build a 3D model of carrier mobility. The mobility of organic single crystals along a specific conducting direction can be expressed as:[57]

$$\mu(\gamma, \Phi) = \frac{e}{2nk_B T} \sum_i W_i \, {r_i}^2 P_i \cos^2(\gamma_i) \cos^2(\theta_i - \Phi), \tag{2.99}$$

however, it does not consider the contributions from polar angles. To address this limitation, the projection function is introduced based on this formula. If there is a known unit vector:

$$\mathbf{n}_i = (\sin\gamma_i \cos\theta_i,\ \sin\gamma_i \sin\theta_i,\ \cos\gamma_i), \tag{2.100}$$

its projection onto another unit vector:

$$\mathbf{n} = (\sin\gamma \cos\theta,\ \sin\gamma \sin\theta,\ \cos\gamma), \tag{2.101}$$

is given by the dot product of the two vectors, leading to the projection function:

$$Q(\gamma, \theta) = \sin\gamma_i \sin\gamma \cos(\theta_i - \theta) + \cos\gamma_i \cos\gamma. \tag{2.102}$$

By applying this projection function to W_i and P_i along a given unit vector, the three-dimensional charge mobility is obtained as:

$$\mu(\gamma,\theta) = \frac{e}{2nk_BT}\sum_i W_i r_i^2 P_i Q^2(\gamma,\theta) \tag{2.103}$$

$$= \frac{e}{2nk_BT}\sum_i W_i r_i^2 P_i \Big[\sin\gamma_i \sin\gamma\cos(\theta_i-\theta) + \cos\gamma_i\cos\gamma\Big]^2. \tag{2.104}$$

Chapter 3

Photochemistry upon charge transfer in triphenylamine (TPA) derivatives

3.1 Introduction

Triphenylamine derivatives, as an important class of organic functional materials, have been widely applied in various cutting-edge research fields due to their excellent optoelectronic properties. For example, in the domain of organic fluorescent probes, these derivatives exhibit outstanding fluorescence, good biocompatibility, high sensitivity and selectivity, which can be used for bioimaging and detection.[91–96] Particularly in photoelectric conversion devices like dye-sensitized solar cells (DSSCs),[97–100] these materials effectively absorb photons across a broad wavelength range, especially in the visible light region.[99] Electronic transitions induced by light absorption generate charge carriers. The efficient separation and transport of these carriers facilitate the conversion of light into electrical energy, leading to an enhanced photocurrent response and improved device performance. Furthermore, the precise molecular design and the introduction of functional substituents have not only optimized the light absorption range of triphenylamine derivatives but also enhanced their photostability and charge transport properties, thus providing crucial support for the development of efficient and low-cost solar cells.[98]

Triphenylamine derivatives exhibit different photophysical and photochemical behaviors in polar and nonpolar solvents. The photochemically induced 6π-electrocyclization reaction of triphenylamine (**TPA**) has been extensively studied.[101–105] The mechanism of the continuous reaction is illustrated in Figure 3.1.[101] Upon photoexcitation, **TPA** is promoted to its first excited state, and subsequently undergoes intersystem crossing to a higher triplet state, with a quantum yield exceeding 90%. From this state, it proceeds through the triplet state of *trans*-*N*-phenyl-4*a*,4*b*-dihydrocarbazole (^{3}**DHC**$_0$), and the rate of formation of ^{3}**DHC**$_0$ has been measured in different nonpolar and polar solvents, including cyclohexane, acetonitrile (**MeCN**), 2,2,2-trifluoroethanol (**TFE**), and Dichloromethane (**DCM**). Subsequently, it converts to the ground state of *Trans*-*N*-phenyl-4*a*,4*b*-dihydrocarbazole (^{1}**DHC**$_0$), exhibiting zwitterionic character,[104] and finally returns to the ground state of **TPA** or generates intermediates, **I** and **II**, under oxidative conditions in the presence of oxygen. A hydrogen peroxide molecule is eliminated, leading to the formation of the carbazole derivative, **NPhCA** (Figure 3.2).[101,105] It has been reported that this reaction strongly depends on the oxygen concentration in the solution, which plays a dual role: quenching the triplet state of **TPA** and facilitating the conversion of intermediates to **NPhCA** via oxidation, thereby enhancing

the overall yield.[101]

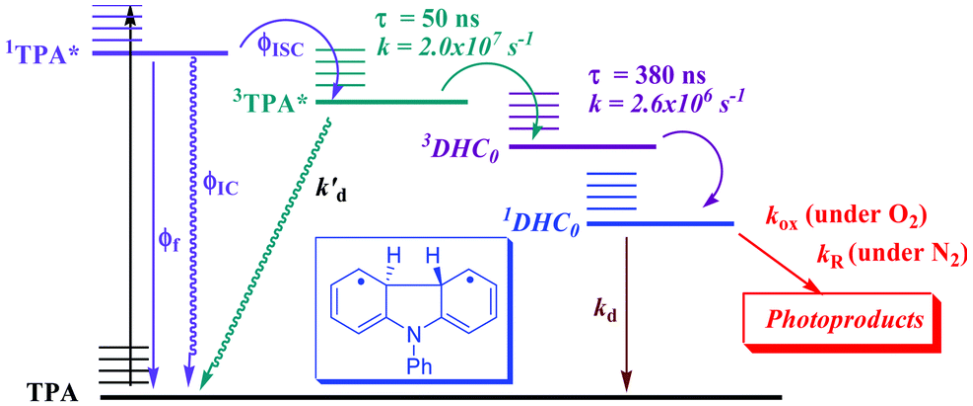

Figure 3.1: Jablonski diagram for the multi-step of the 6π-photocyclization process of **TPA**.[101]

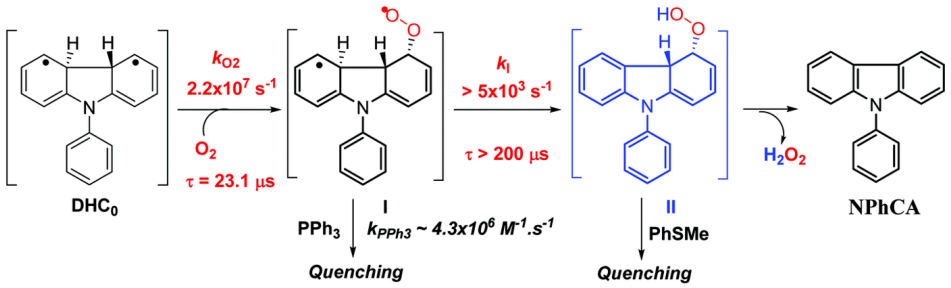

Figure 3.2: The reaction proceeds via the consecutive formation of intermediates **I** and **II**, ultimately leading to the formation of the product **NPhCA**.[101]

TPA derivatives react with Cu^{2+} in acetonitrile solution to form triphenylamine radical cations **($TPA^{\bullet+}$)**. These radical cations subsequently undergo dimerization and deprotonation reactions, ultimately leading to the formation of tetraarylbenzidine (**TPB**). Through electron paramagnetic resonance (ESR) and absorption spectroscopy analyses, it was confirmed that the triphenylamine radical cation plays a crucial role in these processes. The study demonstrates that, under **copper(II)** mediation, the generation of triphenylamine radical cations and their subsequent dimerization is both efficient and controllable (Figure 3.3).[106]

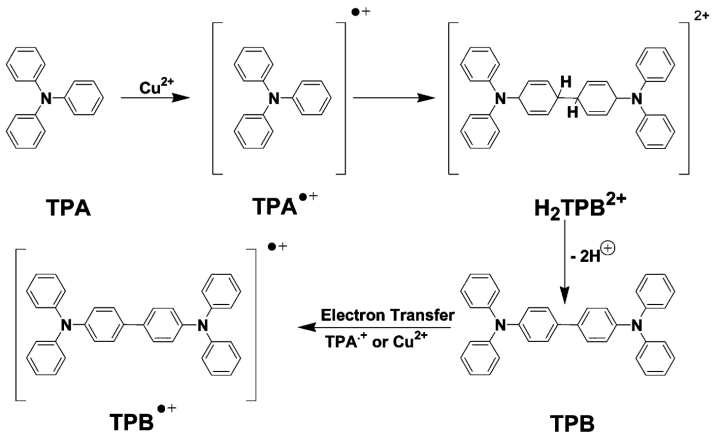

Figure 3.3: Mechanism showing the formation of $\mathbf{TPB}^{\bullet+}$ from **TPA**.[106]

Furthermore, dimethylmethylene-bridged triphenylamine compound **DTPA** can be oxidized by either $\mathbf{B(C_6F_5)_3}$ or $\mathbf{Ag}^+$ to produce the planar radical cation $\mathbf{DTPA}^{\bullet+}$. Subsequent investigations revealed that when $\mathbf{DTPA}^{\bullet+}$ reacts with **DTPA** in the presence of trace amounts of silver cation $\mathbf{Ag}^+$, it leads to the formation of the dication $\mathbf{DTPB}^{\bullet+}$. X-ray crystallography and theoretical calculations indicate that $\mathbf{DTPB}^{\bullet+}$ adopts a singlet state with dual radical characteristics, resembling the properties of Chichibabin-type hydrocarbon compounds. Based on all experimental results and theoretical analyses, a plausible reaction mechanism was proposed, including detailed steps for radical cation formation, dimerization, and final product formation. This mechanism provides significant theoretical support and practical guidance for the application of triarylamine compounds in organic synthesis and electronic materials.[107]

However, there is currently a lack of systematic research on the reaction mechanism of triphenylamine derivatives in chloroform without a catalyst and under light irradiation conditions. Therefore, this study aims to fill this gap by investigating the photochemical behavior and reaction mechanism of **TPA** and **DTPA** in the polar solvent chloroform. Unlike propeller-shaped of **TPA**, **DTPA**, features the ortho-carbon atoms of the phenyl rings connected by dimethylmethylene bridges, which has been reported to improve its physical properties.[107–109] Furthermore, the planar structure of its radical cation makes it a potential electromagnetic material. The modification of **DTPA** not only prevents the close approach of adjacent carbon atoms, thereby inhibiting ring closure, but also increases molecular rigidity. As a result, the molecule adopts a more planar conformation, enhancing the overlap of atomic p-orbitals and extending its π-electron system. This structural change is expected to significantly influence the electronic properties of **DTPA**.

This study provides a new perspective on understanding the photochemical behavior of triphenylamine derivatives under non-metal ion catalysis. Quantum chemical calculations aid in elucidating the specific mechanism of the electron transfer between **TPA** and **DTPA** with the polar solvent (chloroform) under illumination conditions (Figure 3.4), offering a theoretical foundation for the development of materials with high optoelectronic performance.[110] This research provides significant theoretical support for the design and optimization of high-performance organic materials and is expected to pave the way for their widespread applications in fields such as optoelectronics and photocatalysis.

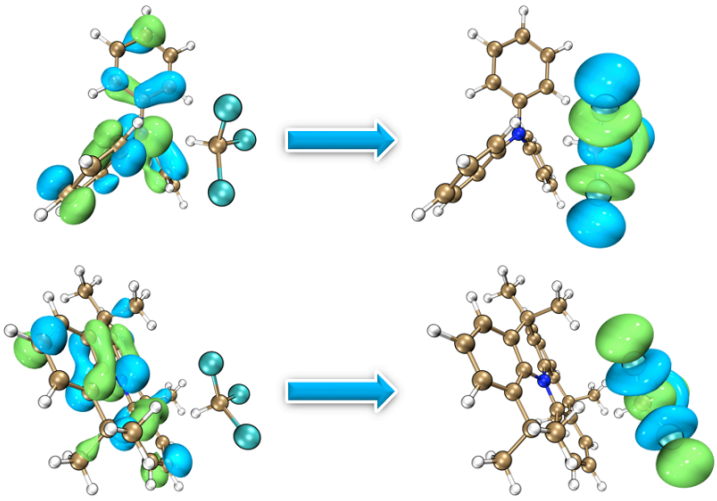

Figure 3.4: Schematic diagram of the electron-hole distribution of **TPA** and **DTPA** in chloroform, illustrating the photoinduced electron transfer from the donor side of the **TPA** derivatives to the electron-accepting chloroform molecules.

3.2 Computational Methods

All calculations were performed using Gaussian 16.[111] In the following sections, detailed protocols for the various topics addressed in this work are described.

Geometry optimizations and frequency calculations were carried out using B3LYP functional[112] with D3 Becke-Johnson (BJ) dispersion correction[113] and the def2-SVP basis set,[114] unless stated otherwise. Absorption spectra for both ground states and excited states were calculated using linear-response time-dependent density functional theory (TDDFT) with the PBE0 functional[115] and the def2-TZVP basis set.[114] The vertical excited-state absorption spectrum of the first excited singlet state (S_1) of **DTPA**, calculated at its optimized equilibrium S_1 geometry, includes absorption contributions from higher electronic states, with transitions originating from the (S_1) reference state. For the charge-transfer (CT) chloroform complexes of **TPA** and **DTPA**, the absorption spectra were computed utilizing the range-separated exchange-correlation functional CAM-B3LYP with reference to the optimized sixth excited state (S_6) to account for the underestimation of charge-transfer excitation energies by most other common exchange-correlation functionals.[116] The first triplet excited state (T_1) absorption spectrum was calculated based on transitions from the optimized T_1 geometry, which was determined using unrestricted density functional theory (UDFT). The transitions to higher triplet excited states ($T_1 \rightarrow T_n$) were computed via time-dependent density functional theory (TDDFT),[117,118] as the direct $S_1 \rightarrow T_1$ transition is spin-forbidden. The spectra of the **DTPA** and **TPA** radical cations were calculated based on their respective optimized doublet ground states. To take into account the influence of the experimental solvent environment on the geometrical properties, the integral equation formalism polarizable continuum model (IEFPCM)[79,119,120] was applied using chloroform during both ground- and excited-state optimizations. For single-point energy calculations, the solvent model density (SMD) method[121] was employed with chloroform as the solvent. The solvent was considered to be in equilibrium with the ground state (GS) and the optimized excited states, but non-equilibrated with the vertical excited electronic states (EES).[122,123]

The hole-electron analysis module was employed to comprehensively characterize electronic excitations.[124] Three indices were selected to describe the separation of electrons and holes: (1) The *D*-index, which quantifies the centroid distance between electrons and holes. (2) The S_r parameter, which represents the overlap between electrons and holes. (3) The *t*-index, which evaluates the degree of spatial separation between electrons and holes. These indices were calculated for the charge-transfer chloroform complexes **[TPA$^+$•CHCl$_3^-$]** and **[DTPA$^+$• CHCl$_3^-$]** using the Multiwfn 3.8 program.[125]

Based on results from the electron-hole analysis, the degree of charge transfer (CT) for the vertical electronic states of **[TPA$^+$•CHCl$_3^-$]** and **[DTPA$^+$•CHCl$_3^-$]** was determined. Subsequently, the geometries of the charge-transfer states were optimized at the CAM-B3LYP/def2-SVP level of theory, and their harmonic frequencies were computed. To ensure reliable geometry optimization on the desired charge-transfer excited-state potential energy surface, a state tracking algorithm utilizing natural transition orbitals (NTOs) was applied at each optimized excited-state geometry.[126] All the optimized molecular coordinate data for the ground-state, excited-state, cationic, and anionic species are detailed in Table A.1-Table A.14 of Appendix A.

Total Gibbs free energies were computed as the sum of the electronic energy and thermodynamic corrections in the gas phase at 298 K and 1 atm, expressed in kcal/mol, along with the free energy of solvation calculated using the PCM solvation model for chloroform.[127] Electronic energies were determined at the M062X/def2-TZVPD level of theory. The energy barriers for single-electron transfer (SET) processes were computed using Savéant's "sticky" concerted dissociative electron transfer (cDET) model. The activation energy barrier ($\Delta G^{\ddagger}$) for the "sticky" cDET process can be estimated by:[128,129]

$$\Delta G^{\ddagger}_{sticky} = \frac{\lambda_{sticky}}{4}\left(1 + \frac{\Delta G_0 - D_P}{\lambda_{sticky}}\right)^2, \tag{3.1}$$

with

$$\lambda_{sticky} = \lambda_i + \lambda_0 + \left(\sqrt{D_R} - \sqrt{D_P}\right)^2, \tag{3.2}$$

the parameter λ_i represents the internal reorganization energy, λ_0 is the external reorganization energy, D_R is the charge-dipole interaction, and D_P is the interaction energy in the corresponding radical-ion pair **CHCl$_2$•**.

3.3 Results and Discussion

3.3.1 Ground and excited-state absorption spectra

Linear-response time-dependent density functional theory (TDDFT),[74] utilizing the PBE0/def2-TZVP exchange-correlation functional and basis set combination, was employed to calculate the vertical excitation energies and oscillator strengths of the energetically low-lying singlet states of **TPA**, **DTPA**, and their corresponding dimers, **TPB** and **DTPB** (Table 3.1, Figure 3.5C, Figure 3.6C). The results show that **TPA** exhibits $S_0 \rightarrow S_2$ and $S_0 \rightarrow S_3$ transitions at 3.97 eV, primarily dominated by transitions from HOMO to LUMO+1 and from HOMO to LUMO+2 (Table 3.1). These transitions correspond to the minimum energy peak observed at 300 nm (4.13 eV) in the experimental steady-state UV/VIS absorption spectra (Figure 3.5A-B, Figure 3.6A-B). The S_1 state of **TPA** shows virtually no oscillator strength and, therefore, does not appear in the experimental absorption spectrum. The peak observed at 360 nm (3.44 eV) following irradiation is attributed to the HOMO-LUMO transition of **TPB**, which has a computed vertical excitation energy of 3.30 eV.

Table 3.1: Vertical singlet excitation energies of **TPA**, **DTPA**, and their dimers **TPB** and **DTPB** in eV, along with the corresponding molecular orbital (MO) contributions and oscillator strengths (in parentheses), calculated at the TDDFT/PBE0/def2-TZVP level of theory.

Excited States	Molecules			
	TPA	**TPB**	**DTPA**	**DTPB**
S_1	3.77 (0.02)	3.30 (1.28)	4.17 (0.16)	3.35 (0.96)
	H → L 97.8%	H → L 96.6%	H → L 94.0%	H → L 96.7%
S_2	3.97 (0.32)	3.62 (0.02)	4.17 (0.16)	3.70 (0.02)
	H → L+1 97.8%	H → L+1 84.4%	H → L+1 93.9%	H → L+1 91.0%
S_3	3.97 (0.32)	3.69 (0.00)	4.29 (0.15)	3.86 (0.16)
	H → L+2 97.8%	H → L+2 76.4%	H → L+2 89.1%	H^{-1} → L 75.1%
S_4	4.48 (0.05)	3.81 (0.00)	4.29 (0.15)	4.00 (0.09)
	H → L+3 93.6%	H-1 → L 93.5%	H → L+3 89.2%	H → L+3 65.8%
S_5	4.48 (0.05)	3.87 (0.08)	4.75 (0.00)	4.01 (0.10)
	H → L+4 93.6%	H → L+4 79.4%	H → L+4 87.0%	H → L+2 47.3% H → L+4 24.8%

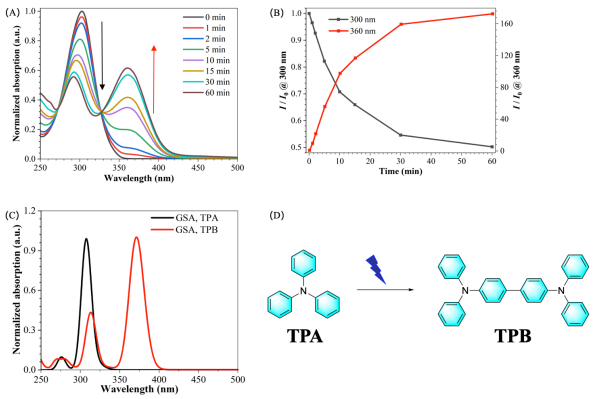

Figure 3.5: (A) Irradiation series of **TPA** in chloroform; (B) The plots of absorption intensity changes of **TPA** at 300 nm (black) and 360 nm (red) in chloroform; (C) Calculated ground-state absorption spectra for **TPA** and **TPB** in chloroform at the PBE0/def2-TZVP level of theory; (D) The photochemical reaction of **TPA** generating **TPB**. The spectra were plotted employing Gaussian broadening functions with a constant value for full-width-at-half-maximum (FWHM) of 0.4 eV.

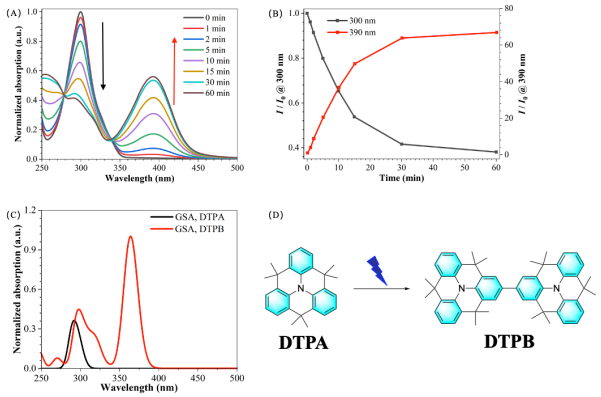

Figure 3.6: (A) Irradiation series of **DTPA** in chloroform; (B) The plots of absorption intensity changes of **DTPA** at 300 nm (black) and 390 nm (red) in chloroform; (C) Calculated ground-state absorption spectra for **DTPA** and **DTPB** in chloroform at the PBE0/def2-TZVP level of theory; (D) The photochemical reaction of **DTPA** generating **DTPB**. The spectra were plotted employing Gaussian broadening functions with a constant value for full-width-at-half-maximum (FWHM) of 0.4 eV.

Due to the slight changes in the molecular and electronic structure of **DTPA** compared with **TPA**, the vertical excitation energy of the S_1 state increases by about 0.4 eV, reaching 4.17 eV, and the oscillator strength of this transition is significantly enhanced. In the molecular orbital picture (Figure 3.7), this excitation is mainly characterized by the HOMO $\rightarrow$ LUMO transition (about 90%), which partly explains the red-shifted shoulder peak observed in the 300–330 nm absorption region.

Additionally, the calculated $S_0 \rightarrow S_3$ and $S_0 \rightarrow S_4$ transitions exhibit excitation energies of 4.29 eV and an oscillator strength of 0.15, which primarily contribute to the slightly blueshifted main absorption band of **DTPA** compared to **TPA**. After irradiation, this peak shifts to 390 nm (3.18 eV), corresponding to the $S_0 \rightarrow S_1$ transition of **DTPB**, where the S_1 state can be characterized as a single-electron HOMO $\rightarrow$ LUMO transition.

Moreover, analysis of the frontier molecular orbitals (Figure 3.7) indicates that the π-system extension primarily modulates the energies of LUMO, LUMO+2, and LUMO+3, with minimal effect on the HOMO and LUMO+1. In particular, the LUMO+3 undergoes a shift in energetic order during the transition from **TPA** to **DTPA**.

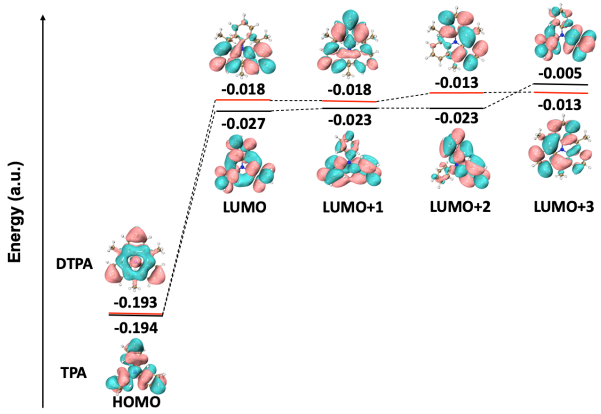

Figure 3.7: Frontier molecular orbitals and their relative energies in atomic units (a.u.) involved in the energetically lowest excited electronic states of **TPA** and **DTPA** in chloroform.

Furthermore, the steady state absorption spectra for potential transient species, which may arise during the transient absorption experiments, have been simulated. The vertical excited-state absorption spectrum of the first excited singlet state of **DTPA** was calculated at its independently optimized equilibrium geometry. The primary feature of this spectrum appears at 1.83 eV (678 nm), with a notable shoulder at 2.05 eV (605 nm) (Figure 3.8C-D). Additionally, an absorption peak at 350 nm, arising from two electronic transitions with excitation energies of 3.66 eV (339 nm) and 3.48 eV (356 nm), was observed at the TDDFT/PBE0/def2-TZVP level, using the PCM model for chloroform solvation. The excited-state absorption spectrum of the first triplet state shows a broad band around 700 nm, attributed to transitions at 1.89 eV (656 nm) and 1.74 eV (713 nm), respectively. Next to this, a smaller peak at 2.27 eV (546 nm) is also observed. In addition to these features, the main absorption feature is located at 2.70 eV (459 nm), with a shoulder attributed to transitions at 2.90 eV (428 nm) and 2.94 eV (422 nm). The excited-state absorption spectrum of the CT state of the **[DTPA^{+}•CHCl$_3^{-}$]** complex is calculated. The main transition is given at 2.27 eV (546 nm) with a pronounced shoulder at 2.48 eV (500 nm). An additional broad band is located at 1.78 eV (697 nm), accompanied by several smaller features at 3.15 eV (394 nm).

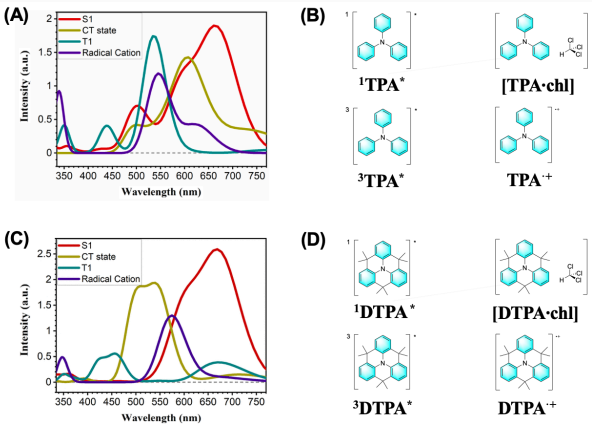

Figure 3.8: (A) Simulated transient absorption spectra of possible short-lived **TPA** species; (B) Chemical structures of representative transient species for **TPA** derivatives; (C) Simulated transient absorption spectra of possible short-lived **DTPA** species; (D) Chemical structures of representative transient species for **DTPA** derivatives. The spectra were plotted employing Gaussian broadening functions with a constant value for full-width-at-half-maximum (FWHM) of 0.565 eV.

For comparison, the absorption spectrum of the **DTPA** radical cation was also calculated. Its most prominent peak is found at 580 nm, resulting from two electronic transitions at 2.18 eV (569 nm) and 2.13 eV (582 nm). A smaller absorption band at 3.53 eV (351 nm) is also observed in the calculated spectrum of the **DTPA** radical cation.

The absorption spectra for potential short-lived **TPA** species are calculated (Figure 3.8A-B). The primary characteristic for the S_1 state manifests at 1.85 eV (670 nm), accompanied by noticeable peaks at around 600 nm and 500 nm. The first triplet excited state has a peak at about 2.31 eV (537 nm). Finally, the spectrum of the **TPA** radical cation is calculated, revealing a prominent peak at 2.27 eV (546 nm). For the CT state of the **[TPA^{+}•CHCl$_3^{-}$]**, the maximum absorption peak is at 2.03 eV (611 nm), with a prominent shoulder at 2.52 eV (492 nm) aligning closely with the experimental spectrum.

3.3.2 The electron and hole analysis

Previously, Fitzgerald et al. observed that amines could undergo single electron transfer upon photoexcitation when dissolved in chloroform.[130] Therefore, potential charge-transfer complexes were also investigated theoretically. The geometries of the **[TPA$^+$•CHCl$_3^-$]** and **[DTPA$^+$•CHCl$_3^-$]** complexes were computed, and their vertical excited states were calculated using DFT and TDDFT, employing the CAM-B3LYP functional (as described above) along with the PCM model for chloroform.

The electron and hole analyses of the excited electronic states reveal significant charge-transfer characteristics, enabling electron transfer following the excitation process. As shown in Table 3.2, the electron and hole analyses of the excited electronic states reveal significant charge-transfer characteristics, enabling electron transfer following the excitation process. The S_6 state of **[DTPA$^+$•CHCl$_3^-$]** has a charge transfer index (D) of 4.078 Å and an electron-hole separation (t-index) of 2.510 Å, while the overlap of the hole and electron (S_r) is only 0.20429 a.u. Similar results were observed for the S_6 state of **[TPA$^+$•CHCl$_3^-$]**, where the D index is 3.501 Å, the t-index is 2.294 Å, and the overlap (S_r) is 0.30039 a.u. (Table 3.3).

Table 3.2: Key parameters of the electron-hole transfer analysis for **DTPA** in chloroform. The first column lists the number of the excited state, with the vertical excitation energy in eV, OS being the oscillator strength, S_r representing the overlap of electrons and holes, D representing the centroid distance of electrons and holes in angstroms, and t indicating the separation of electrons and holes.

Excited States	Energy (eV)	OS	S_r	D (Å)	t
S_1	4.20190	0.09152	0.72662	0.621	-1.307
S_2	4.21990	0.03366	0.73744	0.616	-1.344
S_3	4.54030	0.24644	0.80310	0.453	-1.343
S_4	4.61870	0.34158	0.77766	0.137	-1.907
S_5	4.79320	0.00818	0.80973	0.354	-1.574
S_6	4.79870	0.00945	0.20429	4.078	2.510
S_7	5.63160	0.03097	0.87575	0.147	-1.872
S_8	5.74900	0.43096	0.89687	0.141	-2.116
S_9	5.77380	0.06956	0.91753	0.247	-1.888
S_{10}	5.79870	0.01401	0.91732	0.168	-1.711

Table 3.3: Key parameters of the electron-hole transfer analysis for **TPA** in chloroform. The first column lists the number of the excited state, with the vertical excitation energy in eV, OS being the oscillator strength, S_r representing the overlap of electrons and holes, D representing the centroid distance of electrons and holes in angstroms, and t indicating the separation of electrons and holes.

Excited States	Energy (eV)	OS	S_r	D (Å)	t
S_1	4.22150	0.02910	0.68036	0.143	-1.168
S_2	4.37640	0.30999	0.68155	1.020	-0.747
S_3	4.37680	0.30780	0.68376	1.010	-0.694
S_4	4.88490	0.05704	0.79979	0.673	-0.974
S_5	4.88520	0.05673	0.80733	0.677	-1.518
S_6	5.02250	0.00028	0.30039	3.501	2.294
S_7	5.80500	0.10291	0.88103	0.008	-2.121
S_8	5.86990	0.00878	0.90077	0.042	-1.145
S_9	5.94200	0.06457	0.89478	0.427	-1.346
S_{10}	5.94440	0.06356	0.90257	0.423	-1.575

The detailed nature of this electron transfer state is visualized in Figure 3.9 and Figure 3.10. Specifically, the hole is mostly located at the nitrogen atom in **DTPA** and **TPA** with 17.95% and 22.42%, respectively, while the electron is essentially localized at the Cl atom of chloroform with 15.92% in **[DTPA$^+$•CHCl$_3^-$]** and C atom of chloroform with 24.21% in **[TPA$^+$•CHCl$_3^-$]**, respectively.

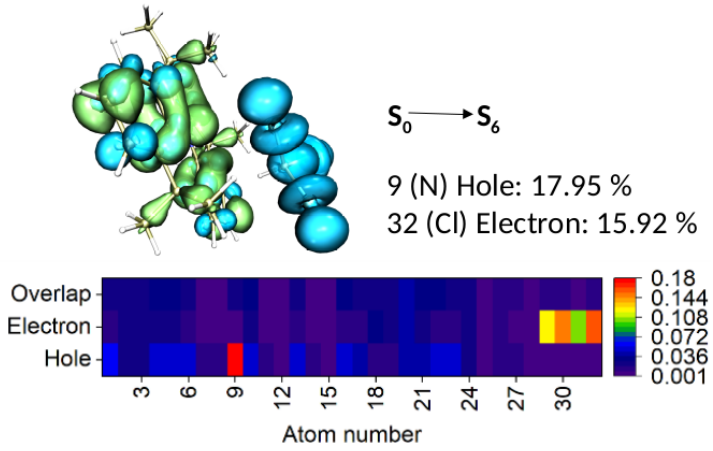

Figure 3.9: The electron (cyan blue) and hole (green) distribution for the **[DTPA$^+$•CHCl$_3^-$]** charge-transfer complex. The atomic number refers to the first 32 non-hydrogen atoms, where 9 is the nitrogen atom of **DTPA**, 29 represents the carbon atom and 30 to 32 are the chlorine atoms of chloroform.

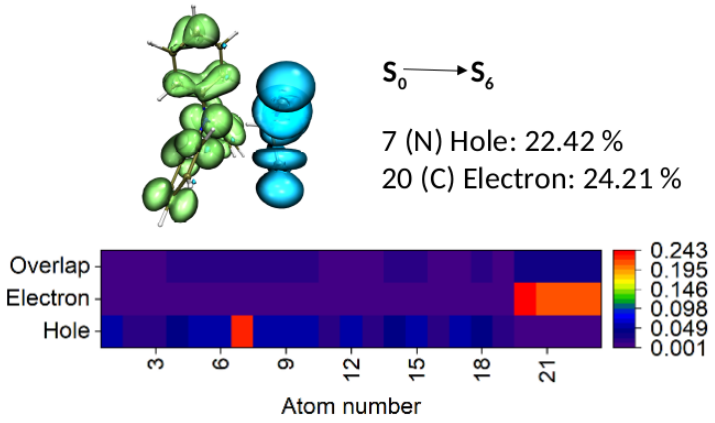

Figure 3.10: The electron (cyan blue) and hole (green) distribution for the **[TPA$^+$•CHCl$_3^-$]** charge-transfer complex. The atomic number refers to the first 23 non-hydrogen atoms, where 7 is the nitrogen atom of **TPA**, 20 represents the carbon atom and 21 to 23 are the chlorine atoms of chloroform.

3.3.3 NTO analysis

Although this charge-transfer configuration initially corresponds to the S_6 state at the Franck-Condon (FC) geometry, i.e., the equilibrium geometry of the electronic ground states of **[DTPA$^+$•CHCl$_3^-$]** and **[TPA$^+$•CHCl$_3^-$]**, it rapidly relaxes to the lowest excited S_1 state upon geometry optimization. To ensure that the optimization follows the correct potential energy surface, a state-tracking algorithm was employed, which is further corroborated by the results of the NTO analysis (Figures 3.11, 3.12, 3.13, and 3.14). During the $S_0 \rightarrow S_6$ excitation of **[DTPA$^+$•CHCl$_3^-$]** or **[TPA$^+$•CHCl$_3^-$]**, the excited electron departs from the n-type molecular orbital localized on the nitrogen atom of **DTPA** or **TPA** and populates the σ^*-type orbital of the chloroform molecule. In the optimized S_6 excited-state geometry of **[DTPA$^+$•CHCl$_3^-$]** and **[TPA$^+$•CHCl$_3^-$]**, the hole remains primarily localized on the nitrogen atom, whereas the electron is concentrated on chloroform, representing the final optimized state.

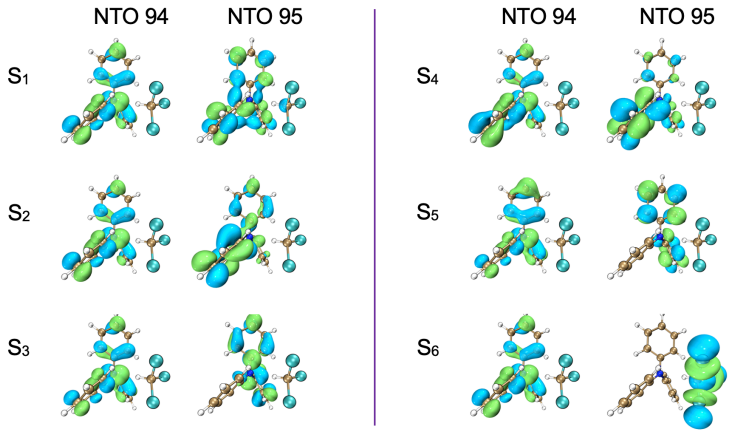

Figure 3.11: NTO analysis for the ground state of **[TPA$^+$•CHCl$_3^-$]**.

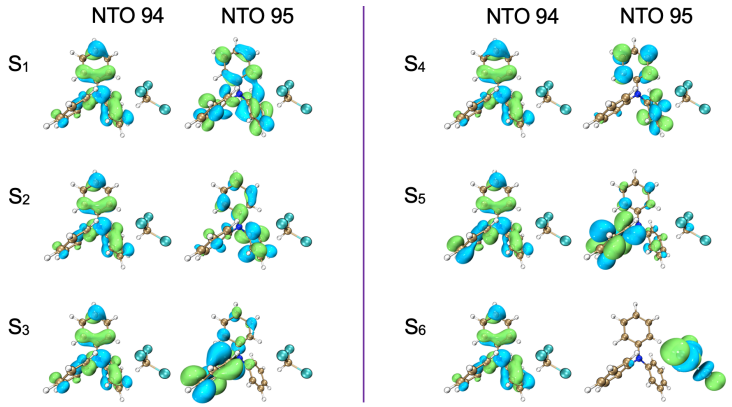

Figure 3.12: NTO analysis for the excited state of **[TPA$^+$•CHCl$_3^-$]**.

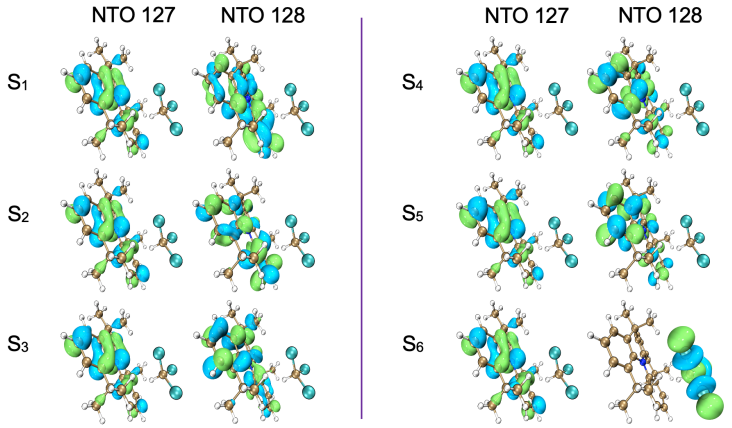

Figure 3.13: NTO analysis for the ground state of **[DTPA$^+$•CHCl$_3^-$]**.

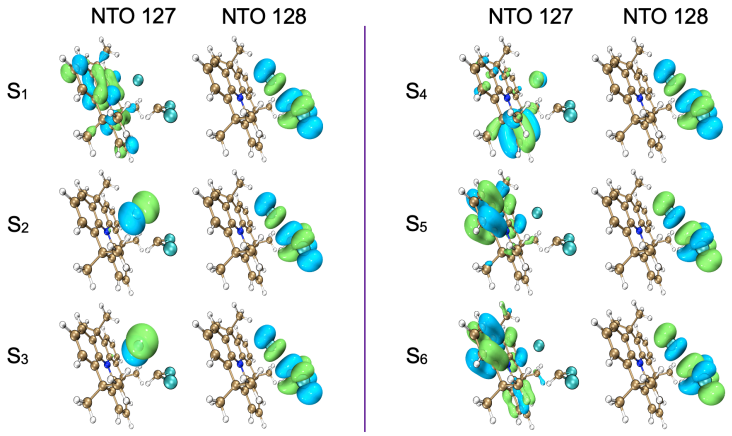

Figure 3.14: NTO analysis for the excited state of **[DTPA$^+$•CHCl$_3^-$]**.

At the equilibrium structure of the **[DTPA$^+$•CHCl$_3^-$]** complex, the chlorine atom (Atom number 60) moves away from the carbon atom (Atom number 57) in Figure 3.15 to a distance of 2.651 Å, an increase of 0.865 Å relative to the carbon-chlorine bond before optimization (Table 3.4).

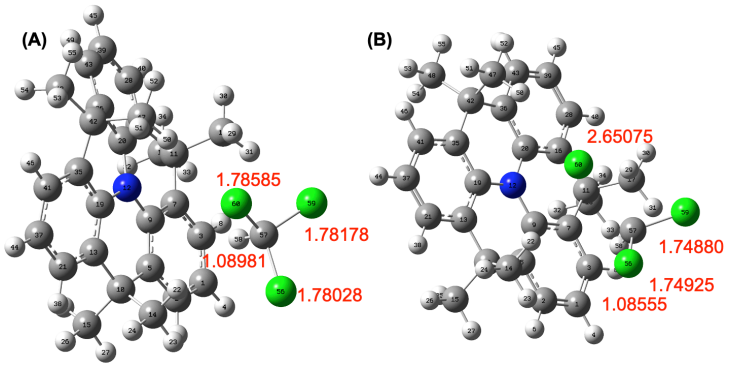

Figure 3.15: Geometry structure of **[DTPA$^+$•CHCl$_3^-$]** (A) Before optimization of the excited state and (B) After optimization of the excited state. Unit of bond length: Å.

Table 3.4: Bond lengths in **[DTPA$^+$•CHCl$_3^-$]**.

Bond	Before optimization (Å)	After optimization (Å)	Difference (Å)
57C – 58H	1.090	1.086	-0.004
57C – 56Cl	1.780	1.749	-0.031
57C – 59Cl	1.782	1.749	-0.033
57C – 60Cl	1.786	2.651	0.865

In the **[TPA$^+$•CHCl$_3^-$]** complex, the transferred electron to the chloroform molecule induces a significant elongation of one of the carbon-chlorine single bonds (Atom number 35 and 39 in Figure 3.16) to 1.993 Å as compared to about 1.782 Å of a C-Cl bond, which increased by 0.211 Å (Table 3.5).

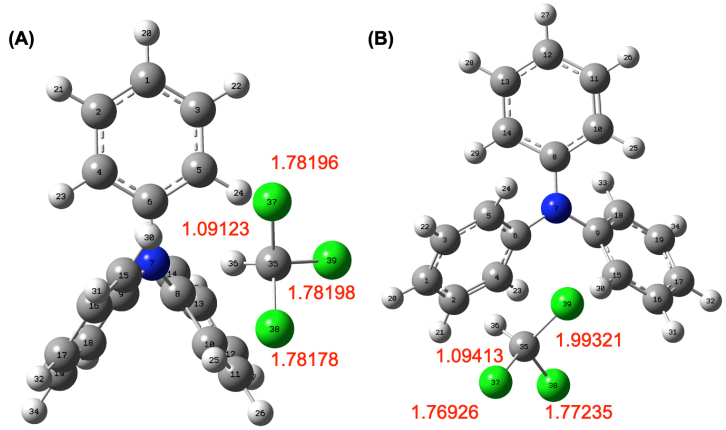

Figure 3.16: Geometry structure of **[TPA$^+$•CHCl$_3^-$]** (A) Before optimization of the excited state and (B) After optimization of the excited state. Unit of bond length: Å.

Table 3.5: Bond lengths in **[TPA$^+$•CHCl$_3^-$]**.

Bond	Before optimization (Å)	After optimization (Å)	Difference (Å)
35C - 36H	1.091	1.094	0.003
35C - 37Cl	1.782	1.769	-0.013
35C - 38Cl	1.782	1.772	-0.010
35C - 39Cl	1.782	1.993	0.211

3.3.4 Gibbs Free Energy Analysis and Photoproduct Formation

The dissociation of the amine (**A**) complex under photooxidation into an **A** radical cation, a **CHCl$_2$** radical, and a chloride anion was proposed (as shown in equation (3.3)).[130] Based on the reported mechanism, a "sticky" concerted dissociative electron transfer model, which belongs to the outer-sphere single-electron transfer (SET) framework,[128,129] was adopted to evaluate the feasibility of this process for both **DTPA** and **TPA**.

$$A^* + CHCl_3 \rightarrow A^{\cdot+} + Cl^- + CHCl_2\cdot \tag{3.3}$$

The obtained energy barriers to form the **TPA** and **DTPA** radical cations from the **[TPA$^+$•CHCl$_3^-$]** and **[DTPA$^+$• CHCl$_3^-$]** amount to 9.04 kcal/mol and 8.58 kcal/mol, respectively (Table 3.6). This indicates that **DTPA** more readily forms a radical cation during the electron transfer process. The Gibbs free energy change of the whole radical formation processes described above are -32.75 kcal/mol and -36.24 kcal/mol, respectively (Equation (3.4) and equation (3.6)). Eventually, the radical cations react further and form the final photoproducts, i.e., **TPB** and **DTPB**, with a Gibbs free energy release of -75.98 kcal/mol and -66.28 kcal/mol (Equation (3.5) and equation (3.7)). The combination of a lower energy barrier and a more negative overall Gibbs free energy suggests that the **DTPA** system possesses greater thermodynamic driving force and faster reaction kinetics throughout the photochemical process.

$$TPA^* + CHCl_3 \rightarrow TPA^{\cdot+} + Cl^- + CHCl_2\cdot \qquad \Delta G_0 = -32.75\,\text{kcal/mol} \tag{3.4}$$

$$2TPA^{\cdot+} + 2Cl^- \rightarrow TPB + 2HCl \qquad \Delta G_0 = -75.98\,\text{kcal/mol} \tag{3.5}$$

$$DTPA^* + CHCl_3 \rightarrow DTPA^{\cdot+} + Cl^- + CHCl_2\cdot \qquad \Delta G_0 = -36.24\,\text{kcal/mol} \tag{3.6}$$

$$2DTPA^{\cdot+} + 2Cl^- \rightarrow DTPB + 2HCl \qquad \Delta G_0 = -66.28\,\text{kcal/mol} \tag{3.7}$$

Table 3.6: Comparison of parameters for **[TPA$^+$•CHCl$_3^-$]** and **[DTPA$^+$•CHCl$_3^-$]**

Parameter	**[TPA$^+$•CHCl$_3^-$]**	**[DTPA$^+$•CHCl$_3^-$]**
λ_i	28.59	31.28
λ_0	23.46	23.59
D_R	65.71	65.71
D_P	2.73	2.73
λ_{sticky}	93.69	69.51
ΔG_0	-32.75	-36.24
$\Delta G^{\ddagger}_{sticky}$	9.04	8.58

3.4 Conclusion

The photoexcitation of **TPA** and **DTPA** in chloroform was simulated using quantum chemical calculations. In these processes, **TPA** and **DTPA** serve as electron donors, while chloroform functions as the electron acceptor. Contrary to the previously reported formation of carbazole, dimer generation was observed in this study. A detailed model was developed to analyze these processes, allowing the identification of intermediates and their verification through comparison of calculated and experimental spectra. Additionally, the reaction pathways leading to the formation of **DTPB** and **TPB** were confirmed by density functional theory calculations of Gibbs free energies for the relevant steps. These findings provide new insights into outer-sphere single-electron transfer, charge-transfer state formation, and charge separation in **TPA** derivatives, offering valuable guidance for the design of novel optoelectronic materials.

Chapter 4

Theoretical Investigation of 3D Anisotropic Charge Carrier Mobility in Halogenated N-Heteroacenes: 4Br-TIPS-TAP and 4I-TIPS-TAP

4.1 Introduction

In recent years, organic semiconductors have attracted great attention due to their advantages such as flexibility, light weight, low cost, easy processing, and versatile chemical synthesis.[131] They have been widely used in organic light-emitting diodes (OLEDs),[132–135] (bio)chemical sensors,[136,137] organic field-effect transistors (OFETs),[138,139] and organic photovoltaic (OPV).[140–142] However, the development of n-type semiconductors has significantly lagged behind that of p-type semiconductors, limiting the progress of practical organic electronics.[143,144] Some studies have reported the transformation of n-type semiconductors into p-type materials. As a widely studied p-type benchmark material in the field of organic semiconductors, pentacene exhibits a hole mobility of up to 35 $cm^2 \cdot V^{-1} \cdot s^{-1}$ at room temperature.[145] To address its poor solubility, low stability, and suboptimal crystal packing, bulky triisopropylsilyl acetylene (**TIPS**) groups were introduced at the highly reactive **C6** and **C13** positions.[146] This functionalization not only enhanced the oxidative stability of the molecule, but also improved its solubility, enabling solution processing. More importantly, **TIPS** substitution induced an ordered brickwork arrangement in the crystal, forming a stable face-to-face π–π stacking structure. Compared with the herringbone packing of pristine pentacene, this arrangement enhances intermolecular electronic coupling and effectively improves charge transport efficiency.[41] Furthermore, by introducing electronegative nitrogen atoms into the acene backbone to stabilize the anionic state, excellent n-type semiconductor properties can be achieved.[147] This approach yields N-heteroacene derivatives, effectively converting p-type semiconductors into n-type semiconductors (Figure 4.1).[41]

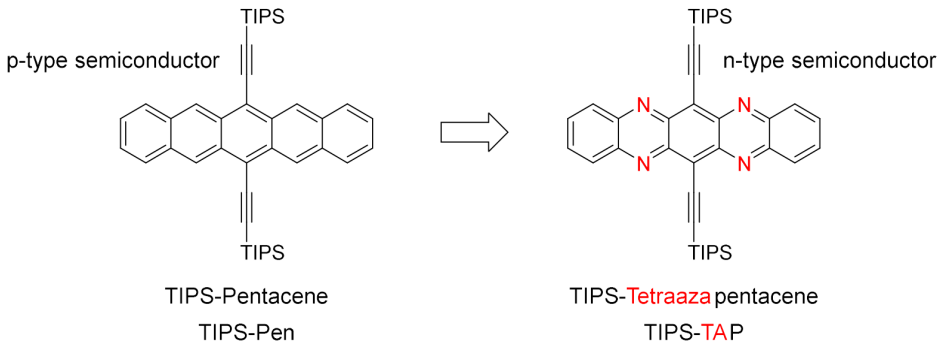

Figure 4.1: Molecular structures of **TIPS-Pen** (p-type) and **TIPS-TAP** (n-type).[41]

Building on the success of **TIPS** functionalization, the introduction of halogen substituents (**F**, **Cl**, **Br**, **I**) into the N-heteroacene backbone has been further explored. Fluorinated and chlorinated **TIPS-TAP** derivatives have been extensively studied. Miao et al. reported that **4Cl-TIPS-TAP** exhibited an electron mobility of up to 27.8 $cm^2 \cdot V^{-1} \cdot s^{-1}$ in solution-processed thin-film transistors, setting a new record for n-type organic field-effect transistors.[148]

Using CDFT-CI theoretical calculations, Jie et al. showed that **4Br-TIPS-TAP** and **4I-TIPS-TAP** (Figure 4.2) have higher electron mobility than **4F-TIPS-TAP** and **4Cl-TIPS-TAP**, indicating their potential as semiconductors. The corresponding three-dimensional electron mobility was further roughly estimated based on the two-dimensional values.[41]

However, most current studies remain limited to in-plane (2D) mobility predictions and do not fully capture the complex packing and anisotropic charge transport behavior in molecular crystals. In real devices, charge migration paths are three-dimensional and strongly depend on molecular orientation and electronic coupling.[55,56] Therefore, accurate descriptions of anisotropic 3D mobility are essential for optimizing molecular alignment, device design, and macroscopic performance modeling.

Since practical devices typically involve both electron and hole transport, the hole mobility is an equally important parameter. In this work, quantum chemical calculations combined with Marcus–Hush theory are employed, and projection functions of the polar angle γ and azimuthal angle θ are incorporated to construct the full three-dimensional electron and hole mobilities of **4Br-TIPS-TAP** and **4I-TIPS-TAP**. The results indicate that these molecules exhibit a stronger propensity for electron transport than for hole transport, consistent with previous reports. This approach provides a more comprehensive understanding of their charge transport behavior and offers guidance for the design of future devices.

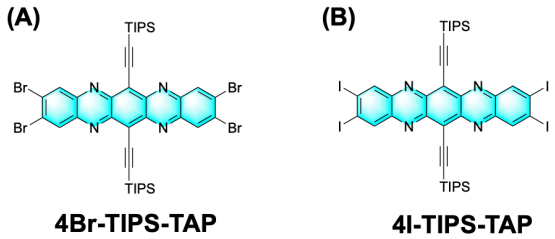

Figure 4.2: Molecular structures of (A) **4Br-TIPS-TAP**; (B) **4I-TIPS-TAP**.

4.2 Computational Methods

The molecular geometry optimizations and frequency analyses were performed using Gaussian 16 software,[111] employing the B3LYP functional[112] with D3 dispersion correction[113] and the def2-SVP basis set.[114] Optimized coordinates for the ground-state, cationic, and anionic species are listed in Table B.1-Table B.6 of Appendix B. Single-point energy calculations were performed at the M06-2X[149]/def2-TZVP[114] level of theory. The transfer integral and electron density overlap integral were calculated using the code J-from-g03,[150,151] in combination with the B3LYP functional and the def2-SVP basis set.

The crystal structures of **4Br-TIPS-TAP** and **4I-TIPS-TAP** were retrieved from the Cambridge Crystallographic Data Center (CCDC) with deposition numbers 1843862[152] and 2155634,[153] respectively. These structural data served as the basis for subsequent computational modeling and analysis.

Reorganization energy (λ) is one of the key parameters regulating the intermolecular charge transfer process in organic materials. It includes internal reorganization energy (λ_{int}) and external reorganization energy (λ_{ext}). Since previous reports indicate that λ_{ext} is typically much smaller than λ_{int} and can be neglected,[154–156] λ is considered equivalent to λ_{int} in this study.

The vertical ionization potential (VIP), adiabatic ionization potential (AIP), vertical electron affinity (VEA), and adiabatic electron affinity (AEA) can be calculated as follows:

$$\mathrm{VIP} = E_{cation}^{vertical} - E_{neutral}^{optimized} \tag{4.1}$$

$$\mathrm{AIP} = E_{cation}^{optimized} - E_{neutral}^{optimized} \tag{4.2}$$

$$\mathrm{VEA} = E_{neutral}^{optimized} - E_{anion}^{vertical} \tag{4.3}$$

$$\mathrm{AEA} = E_{neutral}^{optimized} - E_{anion}^{optimized} \tag{4.4}$$

4.3 Results and Discussion

4.3.1 Reorganization energy

As shown in Table 4.1 and Table 4.2, the reorganization energy of electron transfer for **4Br-TIPS-TAP** (218.35 meV) is 14.96 meV higher than that of **4I-TIPS-TAP** (203.39 meV). The reorganization energy of hole transfer for **4Br-TIPS-TAP** (250.50 meV) is also 15.26 meV higher than that of **4I-TIPS-TAP** (235.24 meV). This may be due to the weaker **C–I** bond, and suppresses the breathing and stretching vibration of the pentacene framework compared to the **C–Br** bond.[41] In addition, the electron reorganization energy is lower than the hole reorganization energy for both molecules. The difference is 32.15 meV for **4Br-TIPS-TAP** and 31.85 meV for **4I-TIPS-TAP**, respectively. This means less structural change is needed for electron transfer than for hole transfer. According to equation (2.78) and equation (2.99), carrier mobility μ increases as the reorganization energy λ decreases. Therefore, lower λ for electrons leads to higher electron mobility. These results suggest that both compounds are more suitable as n-type materials than as p-type.[88]

Table 4.3 summarizes the vertical and adiabatic ionization potentials (VIPs and AIPs), as well as the vertical and adiabatic electron affinities (VEA and AEA) of **4Br-TIPS-TAP** and **4I-TIPS-TAP**. The VIP and AIP of

4Br-TIPS-TAP are 7.22 eV and 7.13 eV, respectively. These values are 0.05 eV and 0.07 eV higher than those of **4I-TIPS-TAP** (7.17 eV and 7.06 eV), indicating that **4Br-TIPS-TAP** requires more energy for ionization and thus exhibits weaker hole generation ability. In contrast, the VEA and AEA values of the two compounds are nearly identical, differing by only 0.01 eV. This implies comparable electron-accepting capabilities, confirming their potential as good electron acceptors.

Moreover, for both compounds, the ionization potentials exceed the electron affinities by more than a factor of two. This implies that the energetic cost of electron removal significantly exceeds that of electron uptake. Accordingly, both molecules tend to exhibit predominant n-type characteristics in organic semiconductors.

Table 4.1: Summary of the relative energies for the optimized geometries of the neutral state (E_{M}) and the anionic state ($E^{-}_{\mathrm{M}-}$), as well as the neutral-state energies at the optimized anionic geometries (E_{M^-}) and the anionic-state energies at the optimized neutral geometries (E^{-}_{M}). The energy values above are given relative to the optimized neutral-state energy E_{M}. Electron reorganization energies for the neutral state (λ_1), the anionic state (λ_2), and the total reorganization energy (λ) are also included. All calculations were performed at the M06-2X/def2-TZVP level of theory.

Molecule	**4Br-TIPS-TAP**	**4I-TIPS-TAP**
E_{M} (meV)	0.00	0.00
E^{-}_{M} (meV)	-3309.00	-3319.83
E_{M^-} (meV)	178.70	178.78
$E^{-}_{\mathrm{M}-}$ (meV)	-3348.65	-3344.43
λ_1 (meV)	39.65	24.60
λ_2 (meV)	178.70	178.78
λ (meV)	218.35	203.39

Table 4.2: Summary of the relative energies for the optimized geometries of the neutral state (E_{M}) and the cationic state ($E^{+}_{\mathrm{M}+}$), as well as the neutral-state energies at the optimized cationic geometries (E_{M^+}) and the cationic-state energies at the optimized neutral geometries (E^{+}_{M}). The energy values above are given relative to the optimized neutral-state energy E_{M}. Electron reorganization energies for the neutral state (λ_1), the cationic state (λ_2), and the total reorganization energy (λ) are also included. All calculations were performed at the M06-2X/def2-TZVP level of theory.

Molecule	**4Br-TIPS-TAP**	**4I-TIPS-TAP**
E_{M} (meV)	0.00	0.00
E^{+}_{M} (meV)	7227.42	7167.73
E_{M^+} (meV)	150.21	130.90
$E^{+}_{\mathrm{M}+}$ (meV)	7127.13	7063.39
λ_1 (meV)	100.28	104.34
λ_2 (meV)	150.21	130.90
λ (meV)	250.50	235.24

Table 4.3: Vertical and adiabatic ionization potentials (VIP, AIP), and electron affinities (VEA, AEA) of **4Br-TIPS-TAP** and **4I-TIPS-TAP** calculated at the M06-2X/def2-TZVP level.

Molecule	VIP (eV)	AIP (eV)	VEA (eV)	AEA (eV)
4Br-TIPS-TAP	7.22	7.13	3.31	3.35
4I-TIPS-TAP	7.17	7.06	3.32	3.34

4.3.2 Crystal Structures and electronic couplings

In the organic crystals, neighboring molecules can be characterized as parallel (P) dimers and longitudinal (L) dimers, as illustrated in Figure 4.3. To further understand the charge transport behavior of **4Br-TIPS-TAP**, the electronic couplings for electron transfer (V_e) and hole transfer (V_h) in both P dimers and L dimers were calculated.

Figure 4.3(A) shows the P dimer configuration, with molecules stacked in parallel along the principal axis. The largest electron couplings occur at D1 (149.5 meV) and B2 (149.1 meV), highlighting the favorable conditions for electron transport in this arrangement. By contrast, hole couplings are much weaker: B2 ($V_h = 74.20$ meV) and D1 ($V_h = 44.81$ meV) are relatively high, while most other configurations have V_h values below 8 meV, indicating inefficient hole transport in this packing motif.

The electron and hole couplings drop rapidly with increasing intermolecular distance. At B1 and D2 (12.58 Å), the electron and hole couplings decrease to around 41.30 meV and 7.00 meV, respectively. At C1 (18.48 Å) and C2 (18.37 Å), V_e further drops to 4.073 meV and 5.316 meV, while V_h declines to 0.1511 meV and 1.499 meV, respectively. This highlights the critical role of distance in determining charge transport efficiency. Our calculated couplings for P dimers are consistent with previous results reported by Jie et al.[41]

Figure 4.3(B) shows L dimer types, where molecular orientation strongly affects orbital overlap and thus the coupling strengths. At 17.15 Å (A–E1), relatively strong couplings are observed ($V_e = 0.7101$ meV, $V_h = 1.877$ meV). However, as the distance increases to the 19–20 Å range (e.g., E2/E4, F1/F3), both couplings sharply decrease to the 10^{-2}–10^{-5} meV range. At 23.03 Å (E3/F2), they reach the lowest level, near 10^{-9} meV. A local increase is observed at 17.83 Å (F4) with $V_e = 4.362 \times 10^{-2}$ meV and $V_h = 6.520 \times 10^{-2}$ meV, which may result from favorable molecular orientation rather than distance alone. This agrees with the well-known sensitivity of charge transfer integrals to molecular packing geometry.[90]

Further insight is gained by analyzing the frontier molecular orbitals, shown in Figure 4.4 and Figure 4.5. For P dimers, HOMO and LUMO distributions reveal spatial delocalization. In A–B2 and A–D1 configurations, the LUMOs are significantly delocalized across both molecules, correlating with the highest V_e values. In contrast, in A–C1 and A–C2, both HOMO and LUMO show minimal overlap, explaining the lowest coupling values in these configurations.

For L dimers (Figure 4.5), the frontier orbitals are mostly localized on one molecule, leading to weak orbital overlap and thus small V_e and V_h. An exception is observed in A–E1, where HOMO has partial contributions from both molecules, indicating better delocalization and explaining its relatively higher coupling.

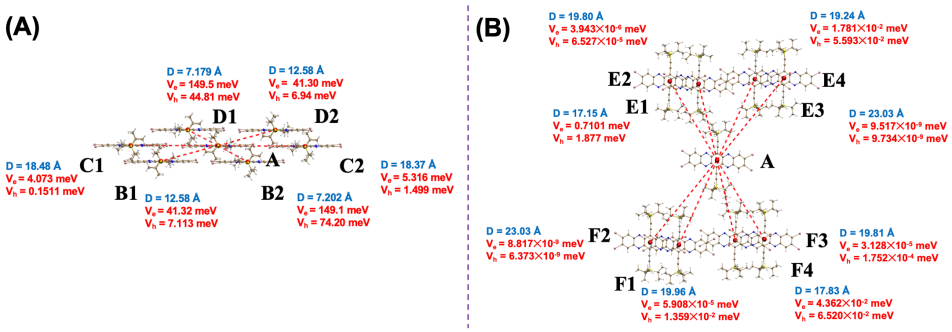

Figure 4.3: Molecular structures and electronic couplings of (A) P dimers and (B) L dimers in **4Br-TIPS-TAP**.

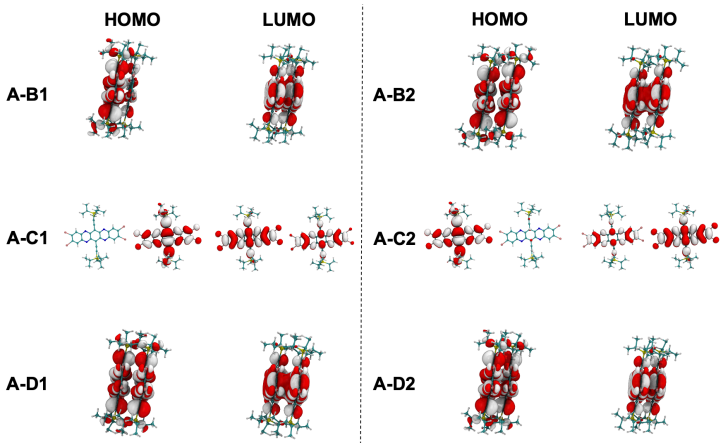

Figure 4.4: HOMO and LUMO distribution in P dimers for **4Br-TIPS-TAP**.

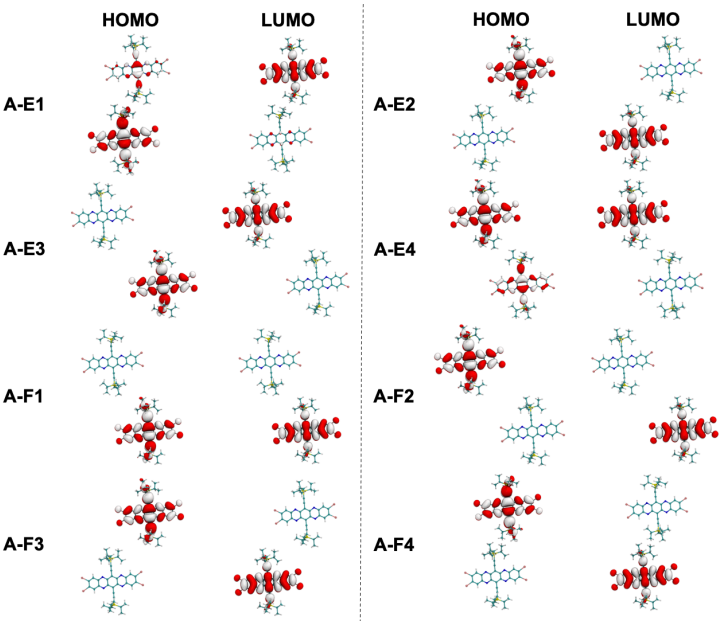

Figure 4.5: HOMO and LUMO distribution in L dimers for **4Br-TIPS-TAP**.

Similar to **4Br-TIPS-TAP**, in Figure 4.6, **4I-TIPS-TAP** shows significantly enhanced charge transfer couplings in the D1 configuration at an intermolecular distance of 7.13 Å, with $V_e = 162.9$ meV and $V_h = 92.21$ meV. Compared to **4Br-TIPS-TAP** at the similar distance, these values are higher by 13.4 meV and 47.40 meV, respectively. This enhancement may be attributed to the effects of iodine substitution. Among halogens, polarizability increases in the order **Br** < **I**, with iodine showing particularly high polarizability. Consequently, iodine can promote halogen bonding and, in some cases, facilitate the formation of supramolecular structures.[157–159] As shown in Figure 4.7, the strong delocalization in A-D1 configurations corresponds directly to the large coupling values, especially the LUMO, which spans both monomers.

When the distance increases to the C1/C2 configurations, the coupling drops sharply ($V_e = 5.886$ meV, $V_h = 1.896$ meV), where orbital overlap is much reduced. Notably, most L dimers show weak couplings, except for special cases like A-E1 and A-F4. This is mainly due to orbital localization within a single monomer, limiting overlap (see Figure 4.8). The relatively stronger coupling in A-E1 and A-F4 ($V_e = 4.362 \times 10^{-2}$ meV, $V_h = 6.520 \times 10^{-2}$ meV) can be attributed to the distribution of HOMO and LUMO over both monomers.

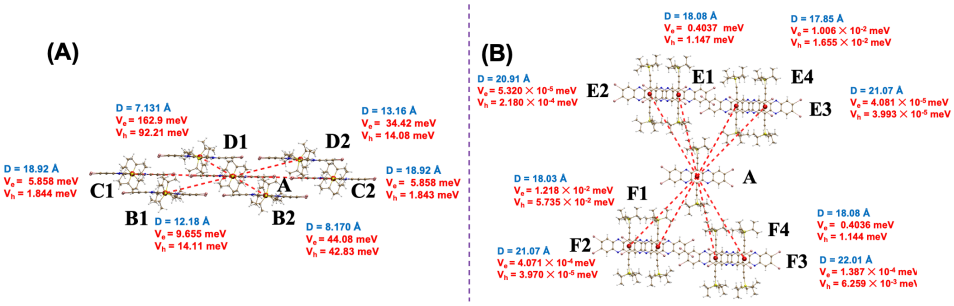

Figure 4.6: Molecular structures and electronic couplings of (A) P dimers and (B) L dimers in **4I-TIPS-TAP**.

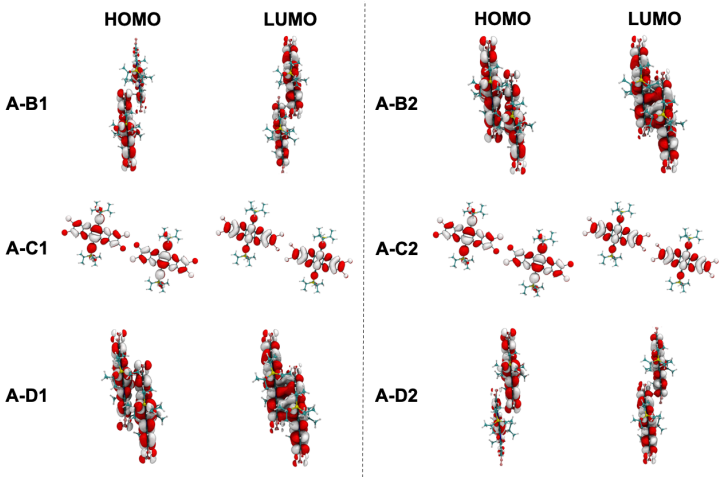

Figure 4.7: HOMO and LUMO distribution in P dimers for **4I-TIPS-TAP**.

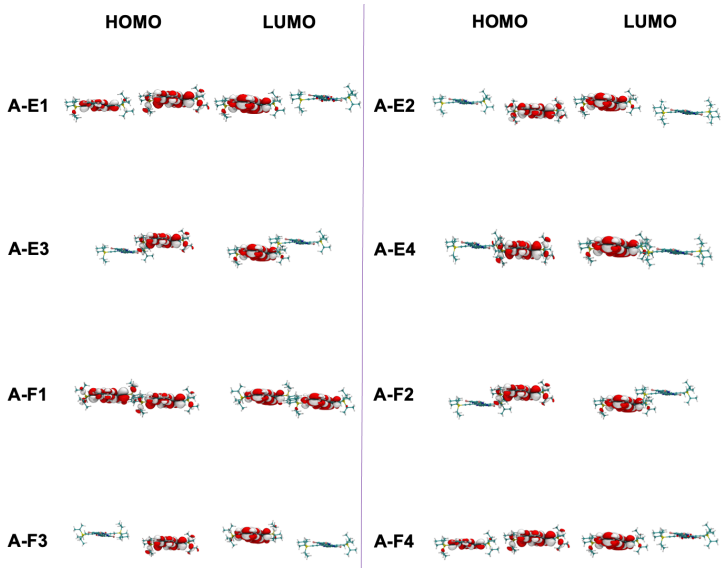

Figure 4.8: HOMO and LUMO distribution in L dimers for **4I-TIPS-TAP**.

4.3.3 Angle-resolved anisotropic electron and hole mobilities

Figures 4.9–4.12 show the anisotropic distributions of electron (μ_e) and hole mobilities (μ_h) for **4Br-TIPS-TAP** and **4I-TIPS-TAP** in three-dimensional and planar directions. The relative orientations of the Cartesian axes (*x*, *y*, *z*) with respect to the crystallographic axes (*a*, *b*, *c*) for **4Br-TIPS-TAP** and **4I-TIPS-TAP** are presented in Figure B.1 and Figure B.2 (Appendix B), respectively.

In the 3D heat maps (Figure A), μ_e shows strong directionality. The highest values appear in the yellow regions, while the lowest are near the central molecule A (blue regions). For **4Br-TIPS-TAP** (Figure 4.9 and Table 4.4), the maximum μ_e reaches 3.011 $cm^2 \cdot V^{-1} \cdot s^{-1}$, about 6.74 times higher than its maximum μ_h of 0.4467 $cm^2 \cdot V^{-1} \cdot s^{-1}$ (Figure 4.10). Similarly, **4I-TIPS-TAP** exhibits a maximum μ_e of 4.063 $cm^2 \cdot V^{-1} \cdot s^{-1}$ (Figure 4.11), 4.88 times larger than its μ_h of 0.832 $cm^2 \cdot V^{-1} \cdot s^{-1}$ (Figure 4.12). These results confirm the strong electron-transport nature of both molecules, consistent with reported n-type performance in N-heteroacene derivatives.[41]

Figures 4.9–4.12(B–D) present 2D projections of mobility on the xy, yz, and xz planes. Both μ_e and μ_h show a "gourd-shaped" pattern, indicating enhanced transport along the molecular long axis (P dimers stacking). On the xy plane, peak mobility nearly matches the 3D maximum, confirming that π–π stacking dominates electron transport. Specifically, **4Br-TIPS-TAP** exhibits a peak electron mobility (μ_e) of 3.011 $cm^2 \cdot V^{-1} \cdot s^{-1}$, corresponding to the maximum in its three-dimensional electron mobility. As indicated in Table 4.4, this maximum occurs at $\gamma = 90.00°$ and $\theta = 239.2°$, precisely within the xy plane. In comparison, **4I-TIPS-TAP** reaches a peak μ_e of 4.063 $cm^2 \cdot V^{-1} \cdot s^{-1}$ at $\gamma = 38.08°$ and $\theta = 206.8°$. This indicates that while both derivatives exhibit their highest electron mobilities near the plane defined by points A, B, and D (Figure 4.10 and Figure 4.12), the orientation of the mobility maxima differs, reflecting subtle variations in molecular packing and the influence of halogen substitution on three-dimensional charge transport.

In contrast, the xz plane (Figure D) shows low mobilities, reflecting weak interlayer coupling in L dimers configuration. The mobilities on the yz plane (Figure C) lie between those on the xy and xz planes, suggesting a combined influence from both P dimer and L dimer types.

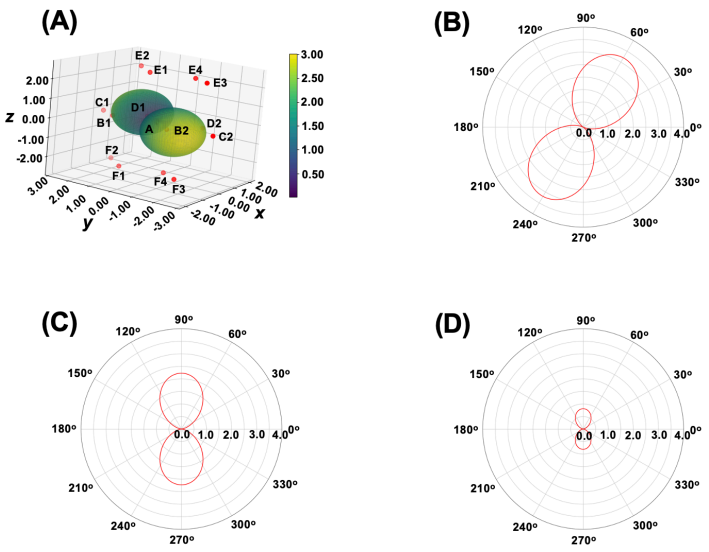

Figure 4.9: (A) Calculated angle-resolved anisotropic electron-mobility values μ_e ($cm^2 \cdot V^{-1} \cdot s^{-1}$) for **4Br-TIPS-TAP** in three-dimensional space. The calculated angle-resolved anisotropic electron mobility of **4Br-TIPS-TAP** in the (B) *xy* plane, (C) *yz* plane, and (D) *xz* plane.

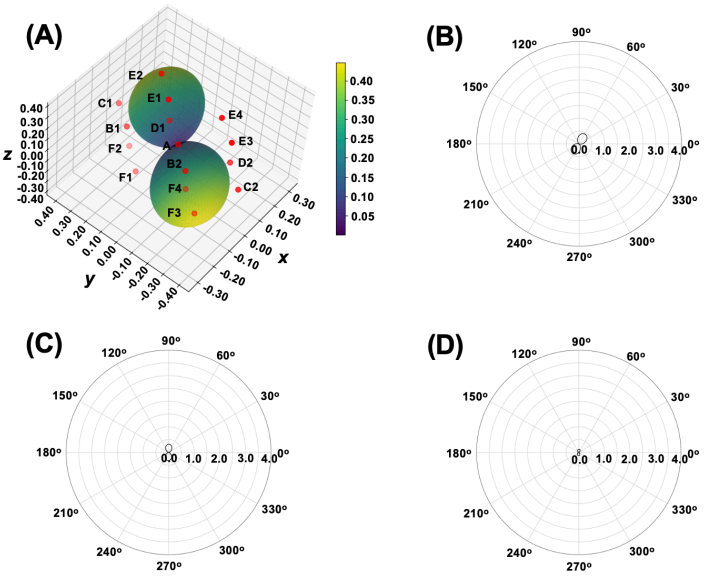

Figure 4.10: (A) Calculated angle-resolved anisotropic hole-mobility values μ_h ($cm^2 \cdot V^{-1} \cdot s^{-1}$) for **4Br-TIPS-TAP** in three-dimensional space. The calculated angle-resolved anisotropic hole mobility of **4Br-TIPS-TAP** in the (B) *xy* plane, (C) *yz* plane, and (D) *xz* plane.

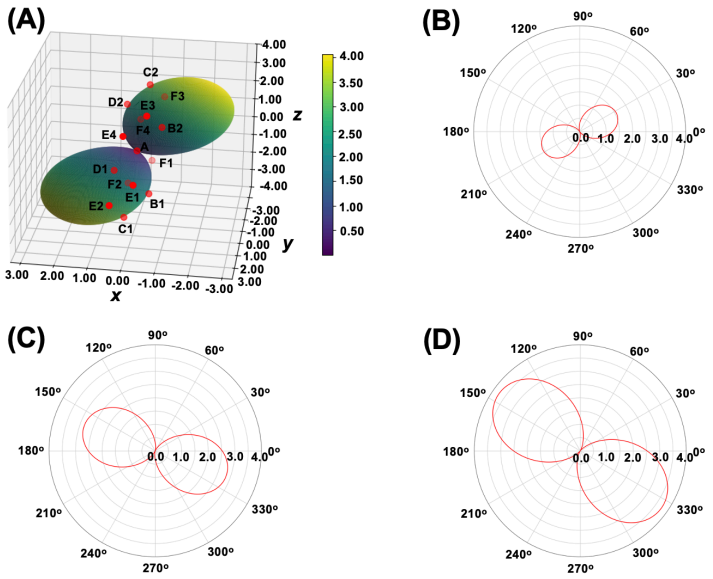

Figure 4.11: (A) Calculated angle-resolved anisotropic electron-mobility values μ_e ($cm^2 \cdot V^{-1} \cdot s^{-1}$) for **4I-TIPS-TAP** in three-dimensional space. The calculated angle-resolved anisotropic electron mobility of **4I-TIPS-TAP** in the (B) *xy* plane, (C) *yz* plane, and (D) *xz* plane.

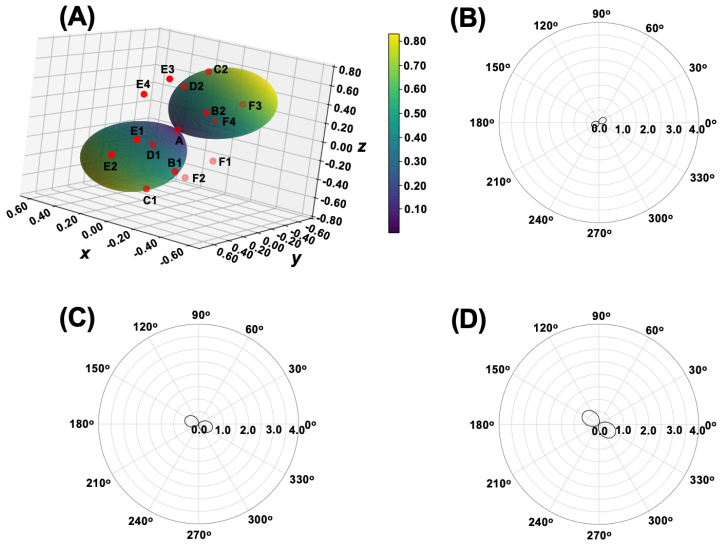

Figure 4.12: (A) Calculated angle-resolved anisotropic hole-mobility values μ_h ($cm^2 \cdot V^{-1} \cdot s^{-1}$) for **4I-TIPS-TAP** in three-dimensional space. The calculated angle-resolved anisotropic hole mobility of **4I-TIPS-TAP** in the (B) *xy* plane, (C) *yz* plane, and (D) *xz* plane.

A summary of mobility ranges is given in Table 4.4 and Figure 4.13. For hole mobility (μ_h), the range is 7.91×10^{-5} – 0.4467 $cm^2 \cdot V^{-1} \cdot s^{-1}$ for **4Br-TIPS-TAP**, while **4I-TIPS-TAP** shows a wider range of 2.04×10^{-4} – 0.8320 $cm^2 \cdot V^{-1} \cdot s^{-1}$. For electron mobility (μ_e), the range is 7.05×10^{-3} – 3.01 $cm^2 \cdot V^{-1} \cdot s^{-1}$ for **4Br-TIPS-TAP**, and 1.30×10^{-4} – 4.06 $cm^2 \cdot V^{-1} \cdot s^{-1}$ for **4I-TIPS-TAP**. Compared with hole mobility, electron mobility shows much higher values overall, indicating the excellent electron transport potential of both compounds.

Table 4.4: Simulated hole mobilities (μ_h) and electron mobilities (μ_e) ($cm^2 \cdot V^{-1} \cdot s^{-1}$) for **4Br-TIPS-TAP** and **4I-TIPS-TAP**, including extreme values and their corresponding angles.

Property	4Br-TIPS-TAP	4I-TIPS-TAP
Hole mobilities (μ_h) Range	$7.914 \times 10^{-5} - 0.4467$	$2.037 \times 10^{-4} - 0.8320$
Hole mobilities (μ_h) Min Orientation	$\gamma = 64.06°, \theta = 148.87°$	$\gamma = 66.08°, \theta = 82.73°$
Hole mobilities (μ_h) Max Orientation	$\gamma = 87.80°, \theta = 57.80°$	$\gamma = 141.8°, \theta = 27.08°$
Electron mobilities (μ_e) Range	$7.050 \times 10^{-3} - 3.011$	$1.297 \times 10^{-4} - 4.063$
Electron mobilities (μ_e) Min Orientation	$\gamma = 171.5°, \theta = 329.2°$	$\gamma = 68.42°, \theta = 86.49°$
Electron mobilities (μ_e) Max Orientation	$\gamma = 90.00°, \theta = 239.2°$	$\gamma = 38.08°, \theta = 206.8°$

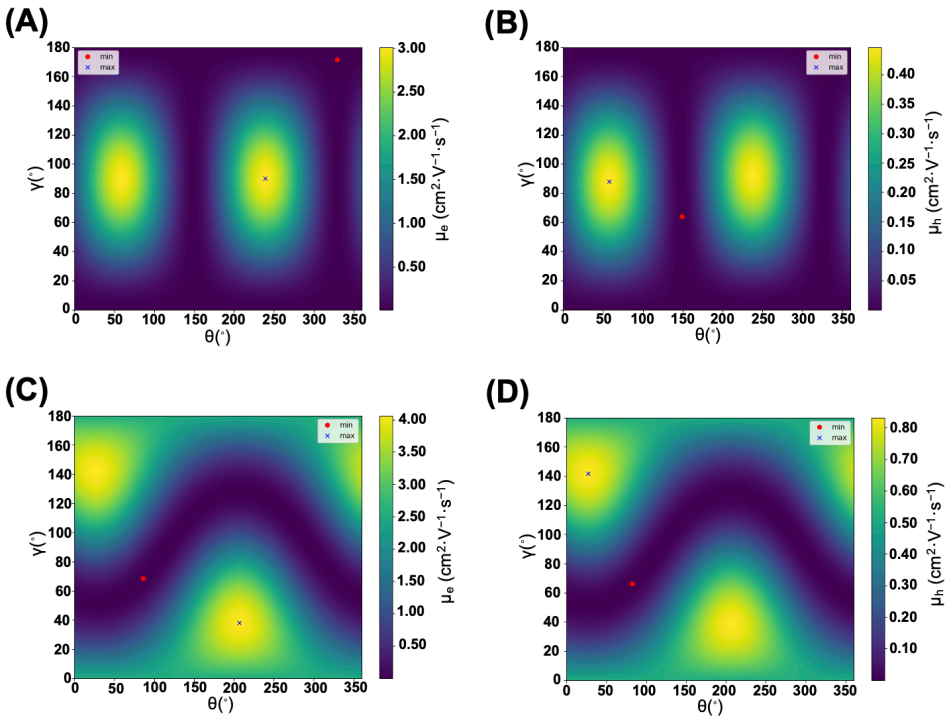

Figure 4.13: Calculated charge carrier mobilities (μ) of **4Br-TIPS-TAP** and **4I-TIPS-TAP** as functions of polar angle γ and azimuthal angle θ. (A) Electron mobility (μ_e) of **4Br-TIPS-TAP**; (B) Hole mobility (μ_h) of **4Br-TIPS-TAP**; (C) Electron mobility (μ_e) of **4I-TIPS-TAP**; (D) Hole mobility (μ_h) of **4I-TIPS-TAP**. Extreme values (maxima and minima) are indicated.

4.4 Conclusion

In this study, based on the projection function, we systematically examined the effects of bromine and iodine substitution on the 3D charge transport properties of **4Br-TIPS-TAP** and **4I-TIPS-TAP**. The calculations show that the substitution sites strongly modify the crystal packing, frontier orbital distribution, and degree of conjugation. These structural changes further affect key electronic parameters, including the ionization potential (IP), electron affinity (EA), reorganization energy (λ), electronic coupling (V), and three-dimensional anisotropic mobility (μ).

By combining quantum chemical calculations with Marcus–Hush theory, we evaluated the three-dimensional carrier mobilities of the two molecular crystals. The results indicate that the electron mobility of **4Br-TIPS-TAP** reaches 3.011 cm^2·V^{-1}·s^{-1}, while that of **4I-TIPS-TAP** reaches 4.063 cm^2·V^{-1}·s^{-1}. In comparison, the electron mobility (μ_e) is about one order of magnitude higher than the hole mobility (μ_h). This suggests that **Br**- and **I**-substituted **TIPS-TAP** derivatives exhibit excellent n-type charge transport properties, consistent with previous reports.

Chapter 5

Investigation of Anisotropic Electron and Hole Mobility in Dipyrrolonaphthyridinedione (DPND) and DPND6 Crystals

5.1 Introduction

Over the past decades, organic semiconductors have become a frontier in electronic materials research due to their potential in OLEDs,[160] OFETs,[161,162] photovoltaic cells,[163] wearable devices, and chemical sensors.[164] In particular, conjugated molecular systems with high tunability and simple processing have enabled the design for high carrier mobility.[165] However, most organic high-mobility semiconductor systems still rely on well-established π-conjugated backbones, such as pentacene,[166,167] perylene diimide (**PDI**),[168,169] [1]benzothieno[3,2-b]-[1]benzothiophene (**BTBT**) and dinaphtho[2,3-*b*:2',3'-*f*]thieno[3,2-*b*]thiophene (**DNTT**) derivatives,[168,170] which have been extensively studied for their carrier transport properties. Molecular systems with novel structures and high carrier-transport potential remain to be explored. Therefore, there is an urgent need to develop and expand the molecular library of high-mobility organic semiconductor materials to support the next generation of organic photovoltaic (OPV) devices before large-scale implementation.

DPND6 is an excellent SF-active molecule. It shows a triplet yield up to 173%, strong blue-green absorption, an appropriate triplet energy of 1.2 eV, and outstanding stability.[60] Wang et al. found that in H-type aggregates of **DPND** and **DPND6** (Figure 5.1), the substantially stabilized charge transfer (CT) state is close in energy to singlet and excimer states, leading to a CT/excimer mixed state. This state can drive the excited-state population to escape from the excimer trap and promote an ultrafast and highly efficient SF process.[171]

Feng et al., combining electronic structure calculations and quantum dynamics simulations, clarified the microscopic mechanism of how alkyl substituents on the **DPND** skeleton influence optical properties and exciton dynamics (Figure 5.2). In alkyl-substituted **DPND6**, the mixing between intramolecular local excited (LE) states and intermolecular CT states is weak, so the low-energy absorption band dominates the optical absorption. In

DPND, the CT and LE states are close in energy and strongly coupled, leading to significant state mixing. As a result, its two low-energy absorption bands have almost equal oscillator strengths and a wide energy spacing of more than 0.5 eV.[61]

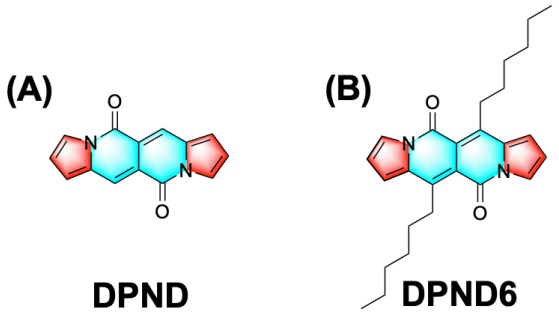

Figure 5.1: Molecular structures of (A) **DPND**; (B) **DPND6**.

Although the excited states and singlet fission (SF) behavior of **DPND** derivatives have been widely investigated, to our knowledge, no theoretical or experimental studies have examined their charge-transport properties. The excited states involved in SF can significantly influence overall charge-transport performance, because the long-lived triplet excitons produced by singlet fission facilitate charge separation and suppress exciton recombination, thereby enabling more efficient formation of free carriers.[172,173] It is therefore important to investigate the carrier-transport properties of SF-active **DPND** derivatives in order to better understand their material performance and optimize device design. Among high-performance molecular systems, **DPND**-type molecules have a well-conjugated backbone, and variations in their substituents, such as the alkyl groups in **DPND6**, can effectively modulate the crystal packing. In addition, most mobility studies focus on two-dimensional in-plane transport, neglecting directional dependence in real three-dimensional crystals. Thus, there is a need to establish a theoretical framework to analyze, from a 3D perspective, the relationship between molecular packing, electronic structure, and mobility.[55,56]

This study focuses on the three-dimensional electron and hole mobilities of **DPND** and **DPND6**, which are systematically evaluated using the projection function. The aim is to explore their potential as n-type, p-type, or ambipolar semiconductors and to assess their suitability as tunable organic semiconductor candidates, based on their reported crystal structures.[60,171] These theoretical predictions not only provide a feasibility analysis for the semiconductor applications of these compounds but also offer guidance for the rational design of future molecular structures.

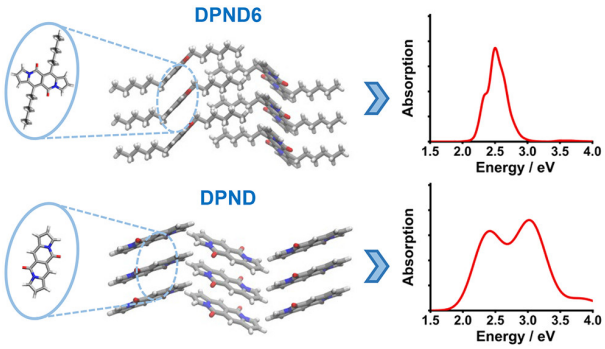

Figure 5.2: Crystal structures of **DPND** and **DPND6**, and their corresponding absorption spectra.[61]

5.2 Computational Methods

The geometry optimizations and frequency calculations of **DPND** and **DPND6** monomers were performed using the Gaussian 16 package[111] at the B3LYP[112]-D3[113]/def2-SVP[114] level of theory. Frequency analyses confirmed that all optimized structures correspond to true minima on the potential energy surface (no imaginary frequencies). The optimized coordinates for the ground-state, cationic, and anionic molecules are presented in Tables C.1-C.6 of Appendix C. To obtain more accurate electronic energies, single-point energy calculations were carried out with the M06-2X[149] functional and def2-TZVP[114] basis set. At this level, key energy parameters were computed, including the reorganization energies (λ), vertical and adiabatic ionization potentials (VIP and AIP), and vertical and adiabatic electron affinities (VEA and AEA).

Crystal structures were modeled based on single-crystal X-ray diffraction data from the Cambridge Crystallographic Data Centre (**DPND**: CCDC No. 2052443[171]; **DPND6**: CCDC No. 1966531[60]). Representative molecular pairs were selected from the crystal packing for electronic coupling analysis. The electronic coupling elements were computed using the J-from-G03 program[150,151] based on Gaussian output files, employing the B3LYP functional with the def2-SVP basis set. These couplings serve as essential input for charge transport calculations.

5.3 Results and Discussion

5.3.1 Reorganization energy

As shown in Table 5.1, the total electron reorganization energy of **DPND** is 163.03 meV. It consists of 10.32 meV from the anionic-state relaxation (λ_1) and 152.71 meV from the neutral-state relaxation (λ_2). In comparison, **DPND6** shows a significantly higher total value of 258.90 meV, with $\lambda_1 = 25.86$ meV and $\lambda_2 = 233.04$ meV. This indicates that the introduction of alkyl chains leads to larger structural changes in the neutral state, thus increasing the intrinsic barrier for electron transport.

The hole reorganization energies of **DPND** (345.75 meV) and **DPND6** (337.42 meV) are nearly the same. A more detailed decomposition shows that **DPND** has a smaller λ_1 (138.14 meV vs. 145.63 meV), indicating less structural distortion in the cationic state during hole transfer, whereas **DPND6** exhibits a smaller λ_2 (191.79 meV vs. 207.61 meV), suggesting reduced distortion in the neutral state during hole transfer.

Overall, **DPND** has a lower electron reorganization energy, making it more favorable for electron transport. In contrast, **DPND6**, with bulkier alkyl chains and increased molecular flexibility, may be more suitable for hole transport but less efficient for electron transport. These results highlight the critical role of side-chain engineering in tuning charge transport properties and provide insights for rational molecular design of organic semiconductors.

Table 5.3 presents the vertical ionization potential (VIP), adiabatic ionization potential (AIP), vertical electron affinity (VEA), and adiabatic electron affinity (AEA) of **DPND** and **DPND6**, calculated at the M06-2X/def2-TZVP level of theory. **DPND** shows a higher VIP (7.59 eV) and AIP (7.45 eV) than **DPND6** (7.31 eV and 7.16 eV, respectively), indicating that **DPND** is less prone to hole injection. On the other hand, its VEA (1.83 eV) and AEA (1.84 eV) are slightly higher than those of **DPND6** (1.74 eV and 1.76 eV), suggesting a small advantage in electron injection. Compared to **DPND**, **DPND6** contains longer alkyl side chains. This structural difference may influence molecular planarity, packing, and charge distribution, leading to slight changes in ionization and electron affinity.

Table 5.1: Summary of the relative energies for the optimized geometries of the neutral state (E_{M}) and the anionic state (E_{M}^{-}), as well as the neutral-state energies at the optimized anionic geometries (E_{M^-}) and the anionic-state energies at the optimized neutral geometries ($E_{\mathrm{M}^-}^{-}$). The energy values above are given relative to the optimized neutral-state energy E_{M}. Electron reorganization energies for the neutral state (λ_1), the anionic state (λ_2), and the total reorganization energy (λ) are also included.

Molecule	**DPND**	**DPND6**
E_{M} (meV)	0.00	0.00
E_{M}^{-} (meV)	-1831.39	-1736.86
E_{M^-} (meV)	152.71	233.04
$E_{\mathrm{M}^-}^{-}$ (meV)	-1841.72	-1762.71
λ_1 (meV)	10.32	25.86
λ_2 (meV)	152.71	233.04
λ (meV)	163.03	258.90

Table 5.2: Summary of the relative energies for the optimized geometries of the neutral state (E_{M}) and the cationic state ($E_{\mathrm{M}^+}^{+}$), as well as the neutral-state energies at the optimized cationic geometries (E_{M^+}) and the cationic-state energies at the optimized neutral geometries (E_{M}^{+}). The energy values above are given relative to the optimized neutral-state energy E_{M}. Hole reorganization energies for the neutral state (λ_1), the cationic state (λ_2), and the total reorganization energy (λ) are also included.

Molecule	**DPND**	**DPND6**
E_{M} (meV)	0.00	0.00
E_{M}^{+} (meV)	7591.98	7310.60
E_{M^+} (meV)	207.61	191.79
$E_{\mathrm{M}^+}^{+}$ (meV)	7453.84	7164.97
λ_1 (meV)	138.14	145.63
λ_2 (meV)	207.61	191.79
λ (meV)	345.75	337.42

Table 5.3: Vertical and adiabatic ionization potentials (VIP, AIP), and electron affinities (VEA, AEA) of **DPND** and **DPND6** calculated at the M06-2X/def2-TZVP level.

Molecule	VIP (eV)	AIP (eV)	VEA (eV)	AEA (eV)
DPND	7.59	7.45	1.83	1.84
DPND6	7.31	7.16	1.74	1.76

5.3.2 Transfer integrals

The electronic coupling characteristics of **DPND** dimers are analyzed for two packing motifs (Figure 5.3): parallel (P) dimers and transverse (T) dimers. The results reveal a strong correlation between the molecular packing arrangement and the corresponding transfer integrals. As shown in Figure 5.3(A), the intermolecular distance strongly influences the electronic coupling strength in P dimers. At the shortest separation (around 3.80 Å, C1/C2), the system shows strong hole coupling ($V_h = 234.5$ meV), about 3.6 times higher than the electron coupling ($V_e = 64.97$ meV), indicating a hole-dominated transport. As the distance increases to 6.619 Å (B2, D1), both couplings drop significantly ($V_e = 27.75$ meV, $V_h = 16.89$ meV). At 7.631 Å, both fall below 2 meV, suggesting inefficient long-range charge transport.

Figure 5.3(B) presents the coupling in T dimers. Due to the larger separations (10.408–11.711 Å), the couplings are generally weaker. At 10.408 Å (E1/E2, F1/F2), V_e and V_h are both around 11 meV. When the distance increases to 10.902 Å (G1/G2, H1/H2), the couplings drop to $V_e = 3.98$ meV and $V_h = 2.29$ meV. At 11.711 Å (E3/F3), both values are below 0.25 meV.

These coupling trends can be explained by the spatial distribution of the frontier orbitals. Figure 5.4 displays HOMO and LUMO patterns in P dimers. In A-B1 and A-D2, the HOMO/LUMO is only distributed on the monomers on both sides, resulting in weak coupling. The LUMOs of the A-B2 and A-D1 dimers are well connected between the molecules, which corresponds to higher electron transfer integrals (V_e) compared to the hole transfer integrals (V_h). A-C1 and A-C2 exhibit strong delocalization of both molecular orbitals, especially HOMO, forming direct interfacial connections. This correlates well with the enhanced couplings observed at approximately 3.80 Å. In T dimers, both the HOMO and LUMO are primarily localized on a single monomer (see Figure 5.5), which accounts for the generally weak electronic couplings.

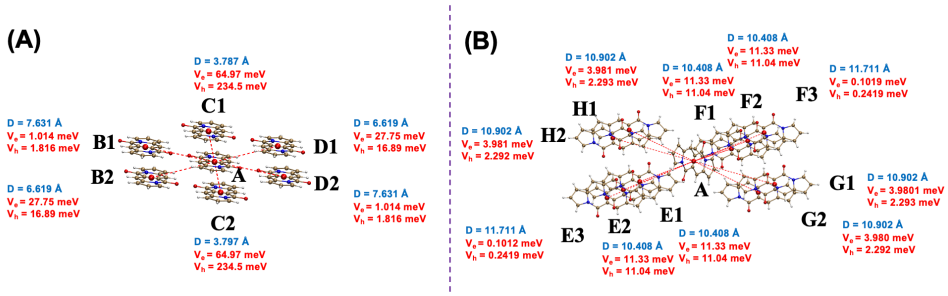

Figure 5.3: Molecular structures and electronic couplings of (A) P dimers and (B) T dimers in **DPND**.

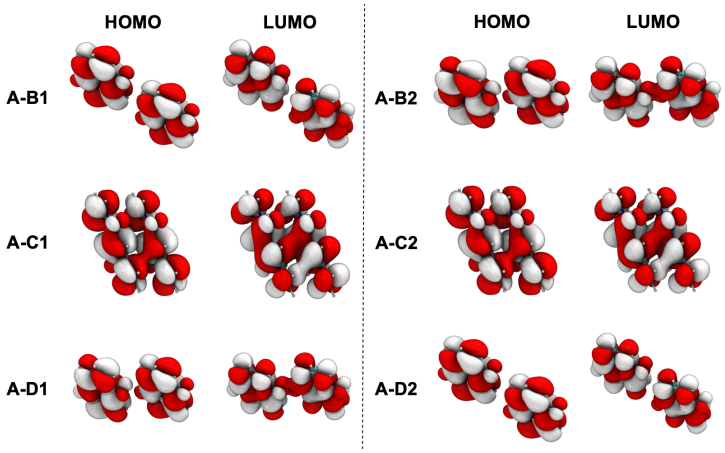

Figure 5.4: HOMO and LUMO distribution in P dimers for **DPND**.

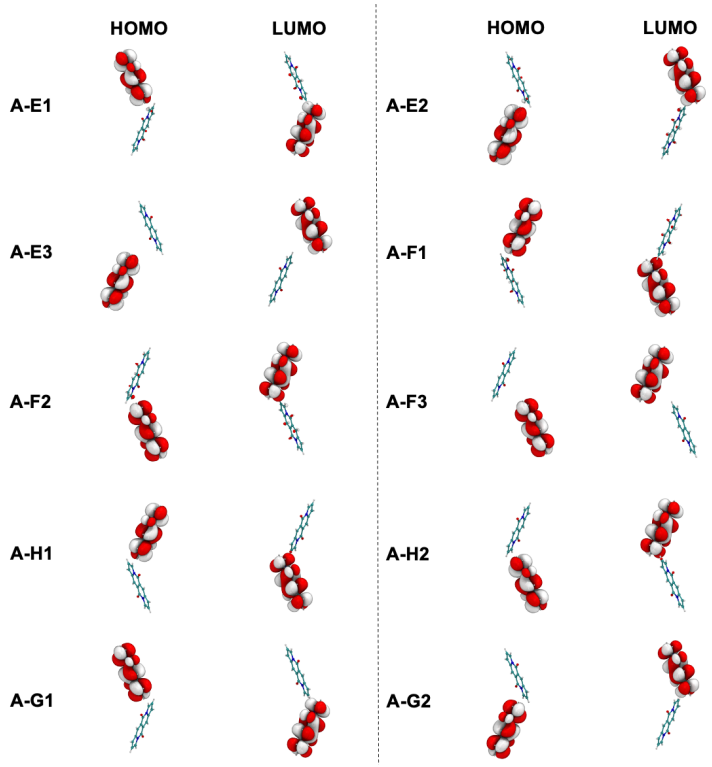

Figure 5.5: HOMO and LUMO distribution in T dimers for **DPND**.

In the single crystal of **DPND6**, the packing arrangement differs from that of **DPND**, leading to distinct electronic coupling behavior. In Figure 5.6(A), the shortest distance (4.607 Å, C1/C2) exhibits strong hole-dominated coupling ($V_h = 62.31$ meV, $V_e = 18.84$ meV; $V_h/V_e \approx 3.3$). At 9.285 Å, two contrasting coupling patterns are observed: D1/B2 shows pronounced couplings ($V_e \approx 56.10$ meV, $V_h = 65.50$ meV; $V_h/V_e \approx 1.17$), while B1/D2 displays moderate couplings ($V_e = 13.76$ meV, $V_h = 8.344$ meV), likely due to differing molecular orientations. At 11.343 Å, both couplings fall below 0.2 meV, indicating poor long-range charge transfer. Figure 5.6(B) shows T dimers of **DPND6**. At 13.714 Å, all configurations (E1, F1, E2, F2) show consistent and weak couplings

($V_e \approx 0.650$ meV, $V_h \approx 0.608$ meV; $V_h/V_e \approx 0.935$). This value corresponds to roughly 1% of the maximum coupling observed at 9.285 Åfor the D1/B2 configurations, confirming that P-type dimers are more favorable for charge transport in **DPND6**.

Figure 5.7 depicts the orbital distributions for various packing motifs. In A-B1/B2/B3, A-C1/C2 and A-D1/D2/D3, both HOMO and LUMO are delocalized across the two monomers, enhancing electronic coupling. By contrast, in A-E1/E2 and A-F1/F2, the orbitals are confined to a single monomer, leading to weaker interactions (Figure 5.8).

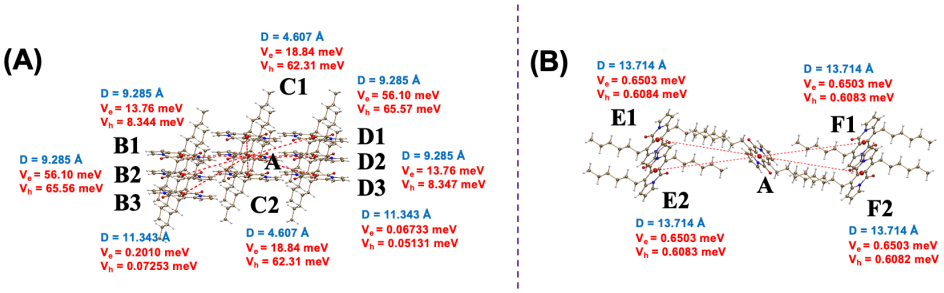

Figure 5.6: Molecular structures and electronic couplings of (A) P dimers and (B) T dimers in **DPND6**.

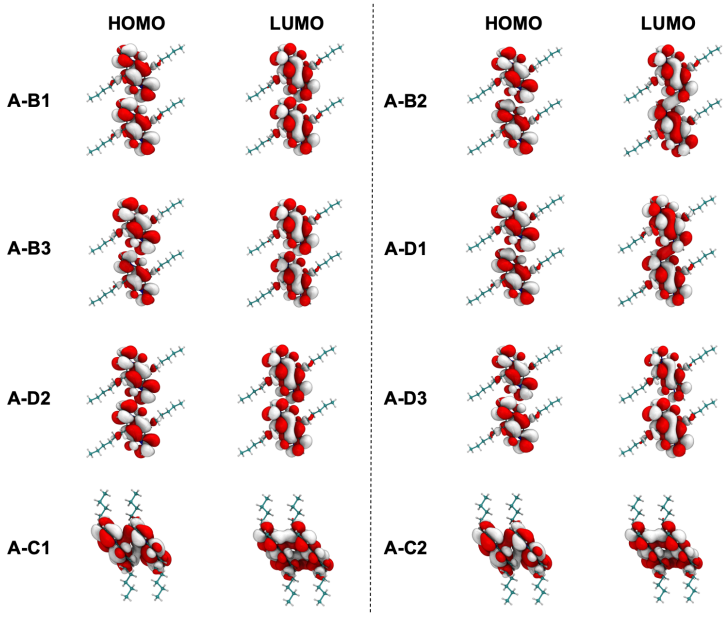

Figure 5.7: HOMO and LUMO distribution in P dimers for **DPND6**.

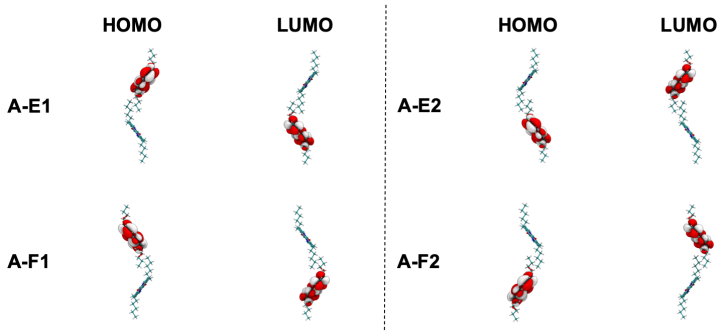

Figure 5.8: HOMO and LUMO distribution in T dimers for **DPND6**.

5.3.3 Electron and hole transfer rates

As summarized in Table 5.4 and Table 5.5, the electron and hole transfer behaviors of **DPND** and **DPND6** crystals exhibit distinct anisotropic features, reflecting the differences in their molecular packing and electronic coupling networks.

For electron transport, the **DPND** crystal shows strong electronic couplings along the A–C1 and A–C2 pathways, with $V_e \approx 64.97$ meV and corresponding transfer rates of 3.618×10^{13} s^{-1}. These high values clearly indicate that the π–π stacking between adjacent molecules in these directions provides strong electron mobility, thus forming the dominant conduction channels. In addition, the A–B2 and A–D1 directions also contribute to electron transport with moderate coupling strengths ($V_e \approx 27.75$ meV) and transfer rates on the order of 10^{12} s^{-1}. In contrast, other directions such as A–E3 and A–F3 exhibit extremely small coupling values (∼0.1 meV) and correspondingly low transfer rates ($\sim 10^7$ s^{-1}), suggesting that charge transfer through these directions is weak. In comparison, **DPND6** displays a different transport behavior. The major electron transfer pathways are found along A–B2 and A–D1, with coupling values of approximately 56.1 meV and transfer rates of 8.472×10^{12} s^{-1}. These values are slightly lower than those in **DPND**, suggesting that the alkyl substitution (hexyl chains) in **DPND6** weakens the intermolecular π–π interactions to some extent. On the other hand, the A–C1/C2 and A–B1/D2 directions exhibit only moderate transfer rates ($\sim 10^{11}$ s^{-1}), while A–E1/F1 and A–B3/D3 are less active, with transfer rates below 10^9 s^{-1}.

The hole transfer characteristics follow a similar but not identical trend. For **DPND**, the A–C1 and A–C2 pathways again dominate, with exceptionally large couplings ($V_h = 234.5$ meV) and high transfer rates (5.531×10^{13} s^{-1}). These values are an order of magnitude higher than most other directions. In contrast, the A–B2 and A–D1 pathways possess moderate electronic couplings (around 17 meV) and correspondingly moderate transfer rates (2.87×10^{11} s^{-1}). The A–E1/E2 and A–F1/F2 pairs exhibit slightly lower rates ($\sim 1.23 \times 10^{11}$ s^{-1}), while the remaining pathways (e.g., A–E3 and A–F3) involve very weak electronic interactions (<1 meV), yielding almost negligible charge transfer on the order of 10^7–10^9 s^{-1}.

For **DPND6**, hole transport exhibits a more distributed pattern, accompanied by generally lower transfer rates. The A–B2, A–C1/C2, and A–D1 directions possess coupling values of 62–66 meV and transfer rates on the order of 10^{12} s^{-1}, reflecting efficient but somewhat less favorable hole transport compared to **DPND**. Meanwhile, the A–B3 and A–D3 paths exhibit extremely low rates around 10^6 s^{-1}, indicating that long-range hole hopping is significantly suppressed.

The comparison results of coupling and mobility of the two materials show that **DPND** has stronger charge

delocalization and more efficient hole transport than **DPND6**. The **DPND** molecule has better planarity and a tighter molecular packing, which leads to a higher degree of overlap between the frontier orbitals (HOMOs and LUMOs), thereby promoting an increase in charge mobility. On the contrary, in **DPND6**, the intermolecular interactions caused by steric hindrance are relatively weak, which leads to a decrease in the transport integral and a stronger localization feature of charge transport.

Table 5.4: Electron transfer rates for different charge hopping pathways in the crystal structures of **DPND** and **DPND6**.

Molecules	Pathways	V (meV)	λ (meV)	W (s^{-1})
DPND	A-B1	1.01350	163.03	8.806×10^{9}
	A-B2	27.74600		6.000×10^{12}
	A-C1	−64.96600		3.618×10^{13}
	A-C2	−64.96600		3.618×10^{13}
	A-D1	27.74600		6.600×10^{12}
	A-D2	1.013500		8.806×10^{9}
	A-E1	11.33000		1.100×10^{12}
	A-E2	11.33100		1.100×10^{12}
	A-E3	0.10172		8.870×10^{7}
	A-F1	11.33200		1.100×10^{12}
	A-F2	11.33100		1.100×10^{12}
	A-F3	0.10186		8.895×10^{7}
	A-H1	3.98060		1.358×10^{11}
	A-H2	3.98050		1.358×10^{11}
	A-G1	3.98080		1.359×10^{11}
	A-G2	3.98020		1.359×10^{11}
DPND6	A-B1	−13.76200	258.90	5.098×10^{11}
	A-B2	56.10000		8.472×10^{12}
	A-B3	−0.20096		1.087×10^{8}
	A-C1	−18.83600		9.551×10^{11}
	A-C2	−18.83600		9.551×10^{11}
	A-D1	−56.09900		8.472×10^{12}
	A-D2	−13.76300		5.099×10^{11}
	A-D3	−0.06733		1.221×10^{7}
	A-E1	−0.65033		1.139×10^{9}
	A-E2	−0.65032		1.139×10^{9}
	A-F1	−0.65025		1.138×10^{9}
	A-F2	−0.65025		1.138×10^{9}

Table 5.5: Hole transfer rates for different charge hopping pathways in the crystal structures of **DPND** and **DPND6**.

Molecules	Pathways	V (meV)	λ (meV)	W (s^{-1})
DPND	A-B1	1.81630	345.75	3.318×10^{9}
	A-B2	−16.89300		2.870×10^{11}
	A-C1	234.50000		5.531×10^{13}
	A-C2	234.50000		5.531×10^{13}
	A-D1	−16.89300		2.870×10^{11}
	A-D2	1.81630		3.318×10^{9}
	A-E1	−11.03600		1.225×10^{11}
	A-E2	−11.03500		1.225×10^{11}
	A-E3	−0.241890		5.885×10^{7}
	A-F1	11.03700		1.225×10^{11}
	A-F2	11.03700		1.225×10^{11}
	A-F3	0.24187		5.884×10^{7}
	A-H1	−2.29260		5.286×10^{9}
	A-H2	−2.29170		5.282×10^{9}
	A-G1	2.29290		5.288×10^{9}
	A-G2	2.29200		5.284×10^{9}
DPND6	A-B1	8.3444	337.42	7.684×10^{10}
	A-B2	65.56200		4.743×10^{12}
	A-B3	−0.07253		5.805×10^{6}
	A-C1	62.30800		4.284×10^{12}
	A-C2	−62.30900		4.284×10^{12}
	A-D1	−65.57100		4.745×10^{12}
	A-D2	−8.34660		7.688×10^{10}
	A-D3	0.05131		2.905×10^{6}
	A-E1	0.608350		4.084×10^{8}
	A-E2	−0.60834		4.084×10^{8}
	A-F1	0.60830		4.083×10^{8}
	A-F2	−0.60822		4.082×10^{8}

5.3.4 Anisotropic charge carrier mobility

The electron and hole mobilities of **DPND** and **DPND6** exhibit strong anisotropy, as shown in Table 5.6, Figure 5.9-Figure 5.12. In Appendix C, the relative orientations of the Cartesian axes (*x*, *y*, *z*) and crystallographic axes (*a*, *b*, *c*) are illustrated for **DPND** and **DPND6** in Figures C.1 and C.2, respectively. The maximum electron transport of **DPND** is observed at a polar angle of $\gamma = 90.00°$ and an azimuthal angle of $\theta = 90.00°$, with a mobility of $\mu_e = 0.2690$ $cm^2 \cdot V^{-1} \cdot s^{-1}$. Similarly, the maximum hole transport is observed at $\gamma = 90.00°$ and $\theta = 270.00°$, with a mobility of $\mu_h = 0.5090$ $cm^2 \cdot V^{-1} \cdot s^{-1}$ (Figure 5.9A and Figure 5.10A). These directions correspond to the π–π stacking axis, indicating an efficient charge transport channel. The maximum hole mobility is approximately

1.89 times higher than the maximum electron mobility, suggesting a transport tendency closer to ambipolar but with a bias toward p-type behavior. 2D radar plots further confirm this trend. Symmetric peaks in the xy and xz planes match the 3D mobility map, while the low mobilities along the xz plane highlight the limited interlayer transport (Figure 5.9B-D and Figure 5.10B-D).

For **DPND6**, the maximum electron mobility $\mu_e = 0.4026\ \mathrm{cm^2{\cdot}V^{-1}{\cdot}s^{-1}}$ occurs at $\gamma = 90.00°$ and $\theta = 14.32°$ (Figure 5.11 and Figure 5.12). The maximum hole mobility $\mu_h = 0.1395\ \mathrm{cm^2{\cdot}V^{-1}{\cdot}s^{-1}}$ appears at $\gamma = 90.00°$ and $\theta = 197.70°$ (Figure 5.11 and Figure 5.12). The maximum electron mobility is approximately 2.9 times higher than the maximum hole mobility, indicating a tendency toward n-type behavior. In the 2D plots, both carriers show peak mobilities in the xy plane around $\theta \approx 14$–$20°$ and 190–200°, while transport in the yz plane drops sharply. The anisotropy arises from strong π–π coupling along the stacking axis and weak interlayer interactions. Notably, in the yz and xz planes, around $\theta = 180°$, both mobilities drop to as low as 10^{-8}–$10^{-9}\ \mathrm{cm^2{\cdot}V^{-1}{\cdot}s^{-1}}$, likely due to poor orbital overlap (Figure 5.11B-D and Figure 5.12B-D).

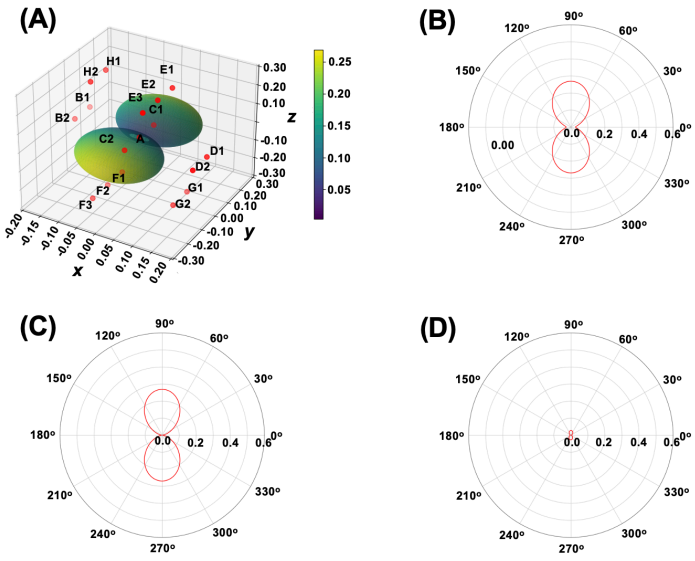

Figure 5.9: (A) Calculated angle-resolved anisotropic electron-mobility values μ_e ($\mathrm{cm^2{\cdot}V^{-1}{\cdot}s^{-1}}$) for **DPND** in three-dimensional space; The calculated angle-resolved anisotropic electron mobility of **DPND** in the (B) *xy* plane, (C) *yz* plane, and (D) *xz* plane.

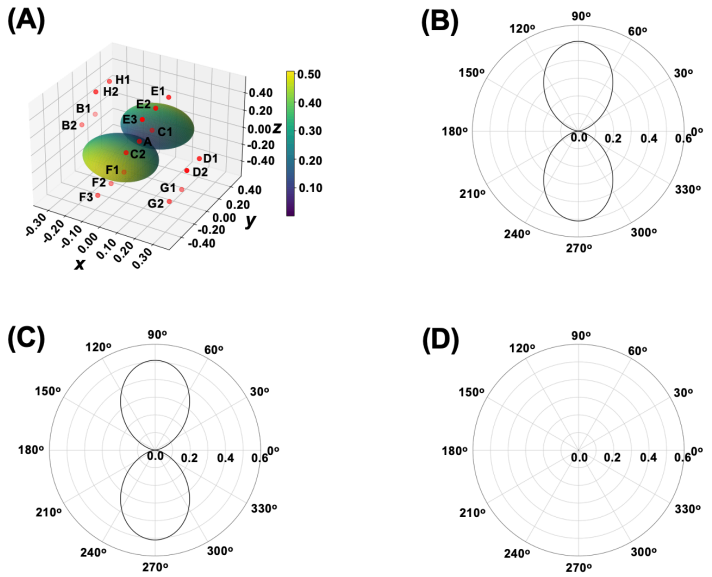

Figure 5.10: (A) Calculated angle-resolved anisotropic hole-mobility values μ_h ($cm^2 \cdot V^{-1} \cdot s^{-1}$) for **DPND** in three-dimensional space; The calculated angle-resolved anisotropic hole mobility of **DPND** in the (B) *xy* plane, (C) *yz* plane, and (D) *xz* plane.

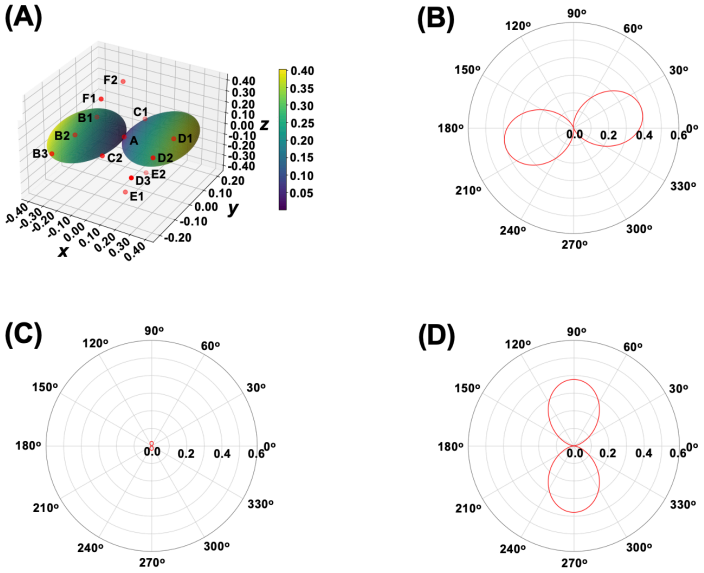

Figure 5.11: (A) Calculated angle-resolved anisotropic electron-mobility values μ_e ($cm^2 \cdot V^{-1} \cdot s^{-1}$) for **DPND6** in three-dimensional space; The calculated angle-resolved anisotropic electron mobility of **DPND6** in the (B) *xy* plane, (C) *yz* plane, and (D) *xz* plane.

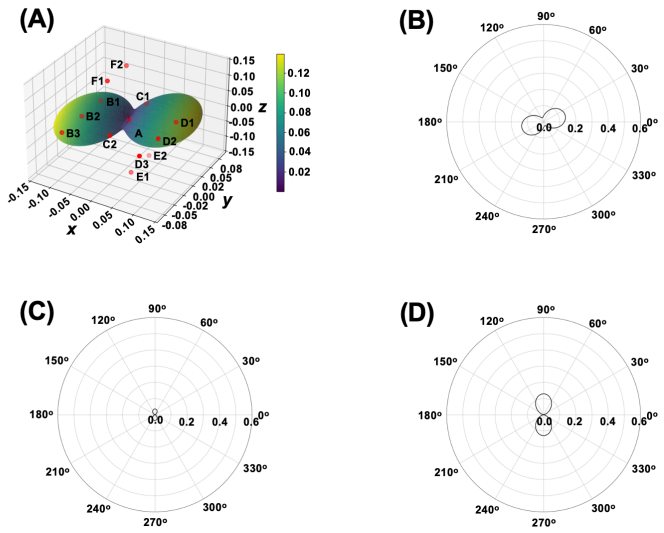

Figure 5.12: (A) Calculated angle-resolved anisotropic hole-mobility values μ_h ($cm^2 \cdot V^{-1} \cdot s^{-1}$) for **DPND6** in three-dimensional space; The calculated angle-resolved anisotropic hole mobility of **DPND6** in the (B) *xy* plane, (C) *yz* plane, and (D) *xz* plane.

As shown in Table 5.6 and Figure 5.13, alkylation significantly affects the hole and electron mobilities of **DPND** derivatives. For hole mobility (μ_h), the range of the unsubstituted **DPND** is 2.9124×10^{-5} – 0.509 $cm^2 \cdot V^{-1} \cdot s^{-1}$, while alkylated **DPND6** decreases to 4.138×10^{-9} – 0.1395 $cm^2 \cdot V^{-1} \cdot s^{-1}$, indicating that side-chain introduction suppresses the transport of p-type carriers. This is likely due to the effect of alkyl side chains on molecular packing, which blocks effective hole transport pathways.

For electron mobility (μ_e), **DPND6** shows a range of 2.9462×10^{-8} – 0.4026 $cm^2 \cdot V^{-1} \cdot s^{-1}$, compared with 3.418×10^{-3} – 0.269 $cm^2 \cdot V^{-1} \cdot s^{-1}$ for unsubstituted **DPND**, demonstrating an improvement in n-type conduction, especially in the orientation corresponding to the maximum electron mobility. This suggests that alkyl side chains can promote the formation of electron transport channels, possibly by modulating intermolecular packing distances and orbital overlap.

Overall, alkylation in **DPND6** leads to a significant decrease in hole mobility while enhancing electron mobility along the optimal direction. This indicates that side-chain modification favors stronger n-type semiconductor behavior, providing structural guidance for designing high-performance organic field-effect transistor materials and highlighting the importance of side-chain length and position in optimizing electron transport.

Table 5.6: Simulated hole mobilities (μ_h) and electron mobilities (μ_e) ($cm^2 \cdot V^{-1} \cdot s^{-1}$) for **DPND** and **DPND6**, including extreme values and their corresponding angles.

Property	DPND	DPND6
Hole mobilities (μ_h) Range	$2.9124 \times 10^{-5} - 0.5090$	$4.138 \times 10^{-9} - 0.1395$
Hole mobilities (μ_h) Min Orientation	$\gamma = 149.8°, \theta = 0.0000°$	$\gamma = 0.0000°, \theta = 0.0000°$
Hole mobilities (μ_h) Max Orientation	$\gamma = 90.00°, \theta = 270.00°$	$\gamma = 90.00°, \theta = 197.7°$
Electron mobilities (μ_e) Range	$3.418 \times 10^{-3} - 0.2690$	$2.9462 \times 10^{-8} - 0.4026$
Electron mobilities (μ_e) Min Orientation	$\gamma = 178.0°, \theta = 0.0000°$	$\gamma = 180.0°, \theta = 50.53°$
Electron mobilities (μ_e) Max Orientation	$\gamma = 90.00°, \theta = 90.00°$	$\gamma = 90.00°, \theta = 14.32°$

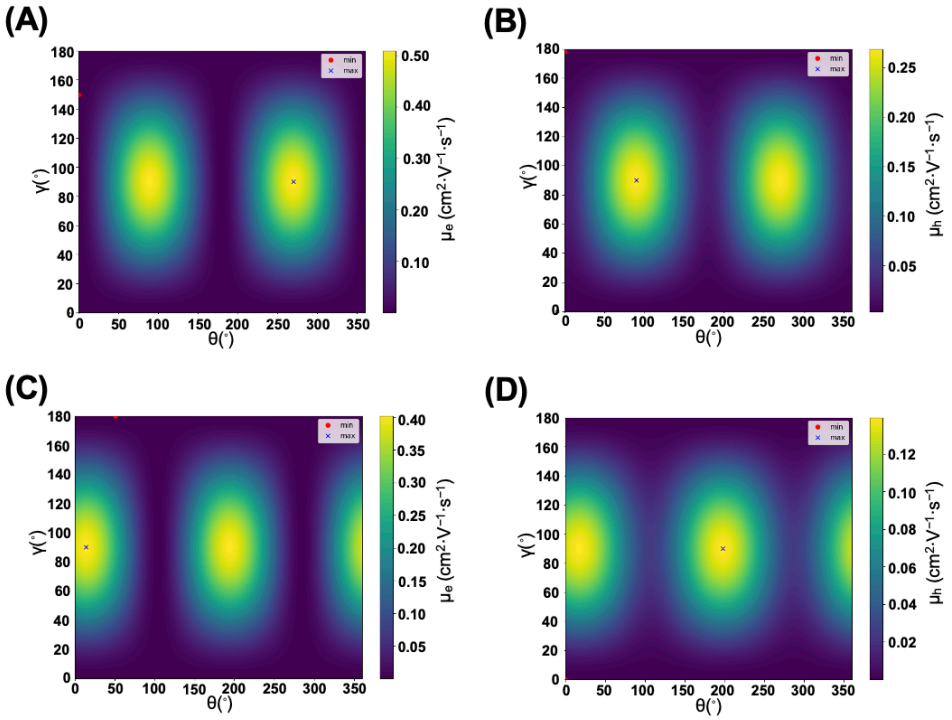

Figure 5.13: Calculated charge carrier mobilities (μ) of **DPND** and **DPND6** as functions of polar angle γ and azimuthal angle θ. (A) Electron mobility (μ_e) of **DPND**; (B) Hole mobility (μ_h) of **DPND**; (C) Electron mobility (μ_e) of **DPND6**; (D) Hole mobility (μ_h) of **DPND6**. Extreme values (maxima and minima) are indicated.

5.4 Conclusion

In this study, the electron and hole mobilities of **DPND** and **DPND6** were theoretically examined, with a focus on the influence of molecular structure and crystal packing on three-dimensional charge-transport anisotropy, based on the projection function. The simulation results show that **DPND** has a maximum hole mobility of 0.5090 $cm^2 \cdot V^{-1} \cdot s^{-1}$, higher than its electron mobility (maximum 0.2690 $cm^2 \cdot V^{-1} \cdot s^{-1}$), indicating a tendency for p-type behavior. In contrast, **DPND6** exhibits an electron mobility of 0.4026 $cm^2 \cdot V^{-1} \cdot s^{-1}$, while the hole mobility drops below 0.1395 $cm^2 \cdot V^{-1} \cdot s^{-1}$, showing dominant n-type character. The mobility differences highlight the

importance of considering anisotropic charge transport when designing high-performance organic semiconductors.

Moreover, the introduction of alkyl side chains plays a key role in tuning crystal packing. Intermolecular distances, π–π stacking, and packing orientations are affected by them, which in turn influences reorganization energy and electronic coupling. Our results indicate that side-chain engineering can effectively modulate charge transport by altering the crystal structure. It provides a promising way to convert p-type semiconductors into n-type semiconductors.

Global Summary and Outlook

This thesis presents a quantum chemical study on the excited-state properties and charge transfer processes of organic molecules, covering multiple levels from molecular photoexcitation to three-dimensional charge transport in crystals.

In Chapter 3, the photoexcitation behaviors of **TPA** and **DTPA** in chloroform were investigated, and the outer-sphere single electron transfer mechanisms between these molecules as electron donors **TPA** derivatives and chloroform as the acceptor were revealed. In future studies, different solvents mixed with chloroform can be introduced, or diverse electron-donating groups can be added to **TPA** derivatives to systematically examine their effects on electron transfer efficiency, selectivity, and product distribution, thereby enabling precise control of photochemical reactions.

In Chapter 4, the effects of bromine and iodine substitution on the three-dimensional charge carrier mobilities of **4Br-TIPS-TAP** and **4I-TIPS-TAP** were investigated by combining the projection function with Marcus–Hush theory and quantum chemical calculations. The results show that halogen substitution significantly modulates molecular conjugation, crystal packing, and electronic couplings, resulting in excellent n-type semiconductor characteristics. In future work, derivatives with other halogens or functional group substitutions can be designed to optimize crystal packing and charge transport pathways by calculating 3D charge mobilities. Additionally, quantum chemical calculations combined with machine learning can be applied to predict the potential effects of different substitution strategies on 3D mobility, enabling the precise design of high-performance organic semiconductors.

In Chapter 5, the anisotropic charge transport in crystals of the singlet fission molecules **DPND** and **DPND6** was further examined. The results indicate that **DPND** exhibits a relatively high hole mobility, showing predominantly p-type characteristics, whereas **DPND6** achieves n-type behavior due to enhanced electron mobility upon introduction of alkyl side chains. In future studies, it would be valuable to systematically vary the length and branching patterns of side chains to better understand how they influence charge transport. Combining quantum chemical calculations with machine learning tools could help screen and identify promising substitution patterns more efficiently. It would also be worthwhile to couple side-chain design with control over crystal orientation, as this could further boost charge transport in real devices and expand their use in organic photovoltaic and optoelectronic applications. In addition, because the calculated charge mobilities still deviate from experimental data, incorporating effects such as nuclear tunneling and dynamic disorder into the simulations will be important for improving the reliability of the predictions.

Appendices

Appendix A

Coordinates of the computationally optimized structures for Chapter 3

Table A.1: Optimized geometry of **TPA** in the S_0 state.

Atoms	X (Å)	Y (Å)	Z (Å)	Atoms	X (Å)	Y (Å)	Z (Å)
C	4.229230	0.143533	-0.000377	H	1.635839	-1.573053	-1.412675
C	3.553079	-0.799145	-0.782024	H	1.525757	1.680494	1.412675
C	3.490927	1.038476	0.781214	H	-2.220590	0.481112	1.410566
C	2.158576	-0.844040	-0.791631	H	-3.541779	2.581097	1.400755
C	2.096558	0.988648	0.791407	H	-2.815209	4.519265	0.000566
C	1.414402	0.047928	0.000210	H	-0.755516	4.316275	-1.400161
N	-0.000526	-0.000246	0.000516	H	0.545975	2.204115	-1.410420
C	-0.749387	1.201073	-0.000122	H	0.693012	-2.162762	1.411679
C	-0.666084	-1.249678	0.000259	H	-0.463711	-4.357535	1.401777
C	-1.905856	1.321595	0.790108	H	-2.504240	-4.699244	0.000286
C	-2.645322	2.504783	0.780411	H	-2.182132	-0.630801	-1.411010
C	-2.237992	3.592140	0.000309	H	-3.358929	-2.814748	-1.401129
C	-1.082743	3.477873	-0.780260				
C	-0.347400	2.292167	-0.790335				
C	-0.191920	-2.310987	0.790916				
C	-0.846144	-3.543343	0.781199				
C	-1.990740	-3.735356	0.000282				
C	-1.811504	-1.448057	-0.790444				
C	-2.469809	-2.678163	-0.780572				
H	5.320730	0.180635	-0.000556				
H	4.115803	-1.500330	-1.403277				
H	4.005014	1.776305	1.402182				

Table A.2: Optimized geometry of **TPA**$^{\cdot+}$.

Atoms	X (Å)	Y (Å)	Z (Å)
C	1.795962	3.792907	-0.000938
C	2.244241	2.807496	0.889518
C	0.748348	3.517012	-0.890493
C	1.655771	1.548490	0.894775
C	0.145239	2.265012	-0.895173
C	0.599833	1.273435	-0.000082
N	-0.001979	0.000853	-0.001299
C	-1.392474	-0.121338	-0.179551
C	0.788702	-1.150063	0.177056
C	-1.909861	-1.183185	-0.951711
C	-3.284361	-1.296065	-1.122893
C	-4.148873	-0.365897	-0.529270
C	-3.633072	0.687281	0.238693
C	-2.260973	0.818112	0.416104
C	2.064963	-1.222369	-0.419787
C	2.838460	-2.362835	-0.239524
C	2.356142	-3.429204	0.531950
C	0.300154	-2.223092	0.952278
C	1.088495	-3.354456	1.125561
H	2.264124	4.779181	-0.001297
H	3.049134	3.029611	1.592215
H	0.411708	4.280557	-1.593739
H	1.979197	0.785586	1.603399
H	-0.649811	2.032388	-1.603841
H	-1.228976	-1.885032	-1.433269
H	-3.687187	-2.105430	-1.734105
H	-5.227754	-0.461078	-0.666373
H	-4.308592	1.400993	0.713087
H	-1.852934	1.616295	1.036471
H	2.420283	-0.400361	-1.041406
H	3.818889	-2.430004	-0.713972
H	2.970427	-4.320921	0.670649
H	-0.674329	-2.144062	1.434373
H	0.721235	-4.178724	1.739212

Table A.3: Optimized geometry of **TPB** in the S_0 state.

Atoms	X (Å)	Y (Å)	Z (Å)	Atoms	X (Å)	Y (Å)	Z (Å)
C	7.117174	3.352049	-1.478184	C	-3.585854	0.000000	-0.000049
C	7.556247	2.688983	-0.327320	N	-4.998923	-0.000001	-0.000069
C	5.969979	2.894257	-2.134964	C	-5.707680	1.121834	0.494330
C	6.855833	1.588782	0.168520	C	-5.707666	-1.121834	-0.494490
C	5.273662	1.784101	-1.655957	C	-6.855831	1.588755	-0.168761
C	5.707680	1.121760	-0.494499	C	-5.273664	1.784350	1.655689
N	4.998924	0.000000	0.000070	C	-7.556247	2.689031	0.326913
C	5.707667	-1.121760	0.494659	C	-5.969982	2.894578	2.134528
C	3.585855	0.000000	0.000050	C	-7.117176	3.352270	1.477677
C	6.855839	-1.588780	-0.168326	C	-6.855838	-1.588755	0.168567
C	7.556240	-2.688981	0.327534	C	-5.273616	-1.784351	-1.655835
C	7.117133	-3.352048	1.478384	C	-7.556240	-2.689030	-0.327128
C	5.969918	-2.894258	2.135131	C	-5.969920	-2.894578	-2.134695
C	5.273615	-1.784102	1.656103	C	-7.117135	-3.352269	-1.477879
C	2.865747	1.160812	0.331495	H	-0.945807	2.068538	-0.612409
C	1.474039	1.157832	0.323077	H	-0.945823	-2.068538	0.612384
C	0.739872	0.000000	0.000011	H	-3.406453	2.067562	-0.606683
C	2.865756	-1.160812	-0.331415	H	-3.406470	-2.067563	0.606589
C	1.474048	-1.157832	-0.323035	H	-7.195099	1.082267	-1.073653
H	7.663856	4.217127	-1.859681	H	-4.386849	1.423022	2.178604
H	8.447056	3.038984	0.200127	H	-8.447055	3.038952	-0.200589
H	5.618875	3.397626	-3.039175	H	-5.618880	3.398083	3.038663
H	7.195102	1.082429	1.073487	H	-7.663859	4.217405	1.859043
H	4.386846	1.422694	-2.178816	H	-7.195132	-1.082266	1.073449
H	7.195135	-1.082427	-1.073283	H	-4.386784	-1.423024	-2.178724
H	8.447065	-3.038981	-0.199887	H	-8.447064	-3.038950	0.200347
H	7.663805	-4.217126	1.859896	H	-5.618792	-3.398083	-3.038820
H	5.618789	-3.397628	3.039330	H	-7.663808	-4.217404	-1.859261
H	4.386783	-1.422697	2.178937				
H	3.406454	2.067651	0.606379				
H	0.945808	2.068628	0.612106				
C	-0.739871	0.000000	-0.000010				
H	3.406471	-2.067652	-0.606284				
H	0.945825	-2.068628	-0.612079				
C	-1.474038	1.157785	-0.323246				
C	-1.474047	-1.157785	0.323206				
C	-2.865746	1.160763	-0.331665				
C	-2.865755	-1.160764	0.331586				

Table A.4: Optimized geometry of **TPA** in the S_1 state.

Atoms	X (Å)	Y (Å)	Z (Å)
C	-1.580781	-3.877220	0.002564
C	-2.201269	-2.881056	-0.763947
C	-0.439827	-3.598619	0.768313
C	-1.675768	-1.573988	-0.770181
C	0.098574	-2.296906	0.772670
C	-0.529698	-1.301308	0.000954
N	0.000444	-0.000285	0.000356
C	1.392227	0.191394	-0.000004
C	-0.861388	1.109244	-0.000251
C	1.940329	1.232620	0.772856
C	3.336689	1.418188	0.767014
C	4.148170	0.571733	-0.001259
C	3.595581	-0.463029	-0.768878
C	2.201149	-0.662564	-0.773378
C	-2.038220	1.062579	0.771261
C	-2.897132	2.179327	0.765025
C	-2.568833	3.305742	-0.002006
C	-0.525392	2.237234	-0.772447
C	-1.395335	3.345297	-0.768202
H	-1.993763	-4.889419	0.003179
H	-3.078007	-3.117739	-1.369320
H	0.021619	-4.380316	1.374231
H	-2.095418	-0.794102	-1.404936
H	0.944887	-2.032574	1.406091
H	1.288534	1.831813	1.408016
H	3.783077	2.207888	1.373856
H	5.231105	0.721197	-0.001778
H	4.238602	-1.102372	-1.376259
H	1.735404	-1.415960	-1.408039
H	-2.231479	0.198520	1.406324
H	-3.805024	2.170724	1.370679
H	-3.239757	4.168859	-0.002713
H	0.360543	2.210865	-1.406273
H	-1.162298	4.222375	-1.374456

Table A.5: Optimized geometry of **[TPA$^+$•CHCl$_3^-$]** in the S_0 state.

Atoms	X (Å)	Y (Å)	Z (Å)	Atoms	X (Å)	Y (Å)	Z (Å)
C	-0.454150	3.512999	1.678130	H	-3.069040	-4.416921	-0.099847
C	-1.028593	2.490152	2.438960	C	2.492412	1.121522	1.784986
C	-0.125647	3.298711	0.334771	H	1.633742	1.762924	1.572091
C	-1.299954	1.238808	1.850844	Cl	3.940696	2.138344	1.802781
C	-0.405182	2.058052	-0.269313	Cl	2.229199	0.364338	3.365491
C	-1.011017	1.029446	0.487041	Cl	2.587843	-0.098965	0.504084
N	-1.346580	-0.171057	-0.158397				
C	-1.534817	-0.127819	-1.579371				
C	-1.501527	-1.416985	0.463451				
C	-0.651612	-0.819486	-2.410288				
C	-0.833194	-0.781755	-3.788216				
C	-1.899492	-0.067024	-4.335295				
C	-2.780609	0.617157	-3.500134				
C	-2.599748	0.594280	-2.120571				
C	-0.828154	-1.735479	1.662770				
C	-0.935831	-3.038716	2.194138				
C	-1.729634	-3.994912	1.549967				
C	-2.317279	-2.383607	-0.173377				
C	-2.431802	-3.674442	0.382272				
H	-0.251332	4.483137	2.137668				
H	-1.271298	2.653801	3.489749				
H	0.346847	4.089195	-0.249943				
H	-1.790833	0.457539	2.427911				
H	-0.123811	1.880232	-1.304955				
H	0.178089	-1.371986	-1.967166				
H	-0.137957	-1.314820	-4.439428				
H	-2.043126	-0.043460	-5.417244				
H	-3.618854	1.172769	-3.924920				
H	-3.280927	1.128794	-1.457008				
H	-0.155419	-1.013420	2.120691				
H	-0.391697	-3.295002	3.104150				
H	-1.805970	-5.002310	1.966562				
H	-2.889823	-2.114652	-1.058502				

Table A.6: Optimized geometry of **TPA** in the T_1 state.

Atoms	X (Å)	Y (Å)	Z (Å)
C	2.571449	-3.281005	-0.482537
C	2.809072	-2.055172	-1.202051
C	1.446408	-3.360287	0.416510
C	1.996556	-0.971401	-1.041025
C	0.600753	-2.303618	0.584352
C	0.840737	-1.049847	-0.138632
N	-0.014800	0.027503	0.009083
C	-1.403212	-0.188481	0.151488
C	0.502508	1.341760	0.018298
C	-2.163570	0.587725	1.051923
C	-3.519338	0.327101	1.218175
C	-4.138880	-0.712387	0.505942
C	-3.382400	-1.488256	-0.380803
C	-2.024360	-1.235875	-0.561674
C	1.753627	1.595817	0.618870
C	2.292368	2.880049	0.583380
C	1.603433	3.923671	-0.046484
C	-0.187640	2.391293	-0.624396
C	0.360483	3.669265	-0.647472
H	3.233876	-4.137203	-0.615560
H	3.648255	-2.001083	-1.900732
H	1.281966	-4.279142	0.985530
H	2.155532	-0.058451	-1.616399
H	-0.225084	-2.351784	1.295484
H	-1.676499	1.378884	1.623491
H	-4.100133	0.930497	1.919699
H	-5.202594	-0.915839	0.645526
H	-3.858213	-2.292968	-0.946219
H	-1.432880	-1.822518	-1.265348
H	2.274157	0.782033	1.124954
H	3.255829	3.070940	1.061827
H	2.031144	4.928019	-0.073447
H	-1.141485	2.187800	-1.112804
H	-0.178657	4.475663	-1.150059

Table A.7: Optimized geometry of **DTPA** in the S_0 state.

Atoms	X (Å)	Y (Å)	Z (Å)	Atoms	X (Å)	Y (Å)	Z (Å)
C	-3.657327	-1.879299	-0.855518	H	-0.217041	-4.420238	-1.282712
C	-3.616768	-0.509932	-0.607074	H	-1.117251	-4.826180	0.203317
C	-2.520399	-2.643625	-0.606985	H	-1.059932	-3.343366	2.218003
C	-2.439795	0.117463	-0.185958	H	-0.090485	-1.847160	2.227902
C	-1.325114	-2.051953	-0.185753	H	0.729443	-3.430264	2.217622
C	-1.253994	-0.644311	-0.069073	H	-4.574318	1.902177	0.201673
N	0.000039	0.000006	0.154017	H	-3.719321	2.397258	-1.284024
C	0.069063	1.408189	-0.069089	H	-3.620966	3.380865	0.201367
C	1.185035	-0.763857	-0.069204	H	-3.336316	1.084771	2.216888
C	-1.114393	2.173593	-0.186045	H	-2.365830	2.590635	2.217031
C	-1.028976	3.504508	-0.607490	H	-1.555384	1.002614	2.227870
C	0.201460	4.106757	-0.856216	H	4.738369	1.445399	0.203404
C	1.367066	3.387010	-0.607430	H	3.934340	3.010348	0.203139
C	1.321750	2.054170	-0.185875	H	3.936766	2.022337	-1.282541
C	1.118150	-2.171678	-0.186119	H	1.644813	0.845057	2.227724
C	2.249728	-2.877236	-0.608000	H	2.606626	2.346183	2.217878
C	3.455783	-2.227592	-0.856936	H	3.425306	0.752699	2.217842
C	2.439618	-0.121653	-0.186064				
C	3.549435	-0.860899	-0.608043				
H	-4.580370	-2.353583	-1.195716				
H	-4.524802	0.078542	-0.727563				
H	-2.570599	-3.724528	-0.727332				
H	-1.939862	4.088527	-0.728083				
H	0.252297	5.143180	-1.196697				
H	2.330757	3.879072	-0.727891				
H	2.194051	-3.957837	-0.728585				
H	4.327861	-2.789746	-1.197744				
H	4.510614	-0.363972	-0.728700				
C	-0.141106	-2.881096	0.281016				
C	-0.212721	-4.339276	-0.185556				
C	-0.140397	-2.873371	1.835622				
C	-2.424617	1.562950	0.280490				
C	-3.651526	2.353814	-0.186822				
C	-2.418790	1.559143	1.835071				
C	2.565781	1.318197	0.281015				
C	3.864434	1.985353	-0.185398				
C	2.558768	1.314553	1.835607				
H	0.640061	-4.912366	0.202769				

Table A.8: Optimized geometry of **DTPA**$^{\cdot+}$.

Atoms	X (Å)	Y (Å)	Z (Å)	Atoms	X (Å)	Y (Å)	Z (Å)
C	-0.000133	-4.140810	0.647666	H	-3.730090	-2.828325	1.133015
C	1.199850	-3.458240	0.474701	H	-4.559307	-1.306045	0.771475
C	-1.200073	-3.458163	0.474703	H	-4.047373	-1.664207	-1.744957
C	1.228577	-2.093005	0.191913	H	-3.178116	-3.168555	-1.367962
C	-1.228713	-2.092926	0.191915	H	-2.359548	-1.874988	-2.282333
C	-0.000045	-1.381269	0.124862	H	3.226850	-1.327913	1.954732
N	0.000000	0.028266	0.016974	H	4.559225	-1.306353	0.771468
C	1.222591	0.734367	-0.089710	H	3.729899	-2.828571	1.133014
C	-1.222545	0.734446	-0.089710	H	4.047259	-1.664466	-1.744965
C	2.440091	0.037841	-0.287837	H	2.359419	-1.875144	-2.282335
C	3.590313	0.771692	-0.591875	H	3.177911	-3.168760	-1.367964
C	3.570867	2.158872	-0.653018	H	0.000051	1.680304	2.350606
C	2.394411	2.843432	-0.340028	H	-0.895086	3.218792	2.458193
C	1.224594	2.157891	-0.033710	H	0.895304	3.218725	2.458191
C	-2.440090	0.037998	-0.287837	H	-0.876448	4.871413	0.580793
C	-3.590264	0.771922	-0.591876	H	0.000146	4.548603	-0.940546
C	-3.570729	2.159099	-0.653021	H	0.876804	4.871339	0.580772
C	-1.224456	2.157971	-0.033711				
C	-2.394230	2.843586	-0.340031				
H	-0.000168	-5.207712	0.877101				
H	2.137309	-4.008705	0.541526				
H	-2.137567	-4.008568	0.541530				
H	4.525564	0.244104	-0.775446				
H	4.476300	2.711853	-0.909196				
H	2.404231	3.930690	-0.323279				
H	-4.525550	0.244392	-0.775445				
H	-4.476128	2.712138	-0.909201				
H	-2.403983	3.930843	-0.323285				
C	-2.564984	-1.460694	-0.134232				
C	-3.581387	-1.748296	1.002644				
C	-3.068871	-2.079804	-1.467201				
C	2.564888	-1.460860	-0.134235				
C	3.581274	-1.748532	1.002640				
C	3.068733	-2.080002	-1.467205				
C	0.000094	2.880052	0.485469				
C	0.000090	2.735280	2.040165				
C	0.000152	4.375646	0.145380				
H	-3.226931	-1.327707	1.954737				

Table A.9: Optimized geometry of **[DTPA^{+}•CHCl$_3^{-}$]** in the CT state.

Atoms	X (Å)	Y (Å)	Z (Å)	Atoms	X (Å)	Y (Å)	Z (Å)
C	2.933566	0.150469	2.575225	C	-2.691378	-3.754606	-0.171152
C	2.269824	1.309513	2.219385	H	-0.947609	-4.596943	0.725037
C	2.327618	-1.056814	2.281891	C	-3.417230	2.392898	-0.657360
H	3.911944	0.187099	3.055497	C	-3.435191	-0.093820	-0.809442
C	1.014237	1.286821	1.595598	C	-3.292310	-2.565801	-0.534646
H	2.741096	2.271550	2.416719	H	-3.390172	4.550552	-0.620221
C	1.073869	-1.128072	1.657455	H	-3.158009	-4.714876	-0.388972
H	2.845783	-1.982772	2.528472	H	-4.368373	2.346973	-1.184799
C	0.392940	0.055301	1.316890	C	-3.331354	-0.126992	-2.346998
C	0.427123	2.630367	1.196948	C	-4.904991	-0.122314	-0.348584
C	0.558605	-2.517085	1.319365	H	-4.244784	-2.593115	-1.060697
N	-0.882038	0.008098	0.706169	H	-2.276280	-0.097870	-2.654120
C	-0.957930	2.455463	0.618660	H	-3.855436	0.733492	-2.792184
C	1.311105	3.244598	0.089894	H	-3.793704	-1.042115	-2.749928
C	0.364912	3.554733	2.429465	H	-5.465290	0.739667	-0.734391
C	-0.835345	-2.441324	0.741320	H	-4.973708	-0.112174	0.748613
C	1.468622	-3.126701	0.230761	H	-5.425740	-1.016245	-0.716920
C	0.553892	-3.392829	2.588148	Cl	3.942783	1.428306	-1.939644
C	-1.531612	1.199721	0.339106	C	3.091575	-0.052928	-1.555763
C	-1.470028	-1.231063	0.399385	H	2.903615	-0.136802	-0.488541
C	-1.647707	3.643144	0.272093	Cl	3.861663	-1.492776	-2.186530
H	1.299508	2.603429	-0.801602	Cl	0.527720	0.012579	-2.201920
H	2.352394	3.338487	0.432912				
H	0.959366	4.249913	-0.188077				
H	-0.255165	3.111168	3.221771				
H	-0.051143	4.540050	2.179525				
H	1.367991	3.732508	2.839327				
C	-1.464264	-3.677903	0.454701				
H	1.404905	-2.534279	-0.691644				
H	1.179985	-4.164940	0.006177				
H	2.517870	-3.136525	0.562885				
H	-0.086006	-2.952715	3.366430				
H	1.567113	-3.497904	2.997683				
H	0.193305	-4.409391	2.381393				
C	-2.768582	1.178592	-0.324692				
C	-2.704933	-1.305363	-0.264795				
C	-2.876365	3.627006	-0.354881				
H	-1.178033	4.599151	0.496214				

Table A.10: Optimized geometry of **DTPA** in the T_1 state.

Atoms	X (Å)	Y (Å)	Z (Å)	Atoms	X (Å)	Y (Å)	Z (Å)
C	-3.562574	2.148451	-0.627844	H	-1.396523	-1.668372	-2.309153
C	-2.400423	2.821562	-0.246190	H	-3.169754	-1.566976	-2.480334
C	-3.567588	0.755245	-0.664246	H	-3.926879	-1.720632	1.229635
C	-1.231523	2.122062	0.055019	H	-3.795578	-3.153868	0.174828
C	-2.422152	0.008318	-0.372378	H	-4.658547	-1.724890	-0.397142
C	-1.224182	0.711191	-0.076226	H	0.002649	4.568963	-0.661133
N	0.000050	0.012826	0.043660	H	0.882576	4.777892	0.876892
C	1.225101	0.709844	-0.075924	H	-0.876868	4.779089	0.876966
C	-0.000757	-1.378691	0.037213	H	0.000170	1.466242	2.396330
C	1.234023	2.120653	0.055692	H	-0.894488	2.990617	2.630608
C	2.403929	2.818887	-0.244571	H	0.896735	2.989429	2.631056
C	3.565503	2.144550	-0.625752	H	3.166614	-1.568789	-2.481770
C	3.568836	0.751349	-0.662876	H	1.393306	-1.667494	-2.309770
C	2.422321	0.005681	-0.372056	H	2.400686	-3.091834	-1.932820
C	-1.273525	-2.046613	0.355193	H	4.656280	-1.731115	-0.400047
C	-1.245693	-3.097999	1.227843	H	3.791410	-3.159064	0.171587
C	-0.001711	-3.593936	1.741496	H	3.925913	-1.726808	1.227318
C	1.271296	-2.048197	0.354456				
C	1.242671	-3.099621	1.226969				
H	-4.470264	2.708043	-0.863393				
H	-2.417768	3.907332	-0.165500				
H	-4.490254	0.235504	-0.922942				
H	2.422483	3.904611	-0.163473				
H	4.474020	2.703152	-0.860461				
H	4.490998	0.230632	-0.921372				
H	-2.166221	-3.616120	1.504261				
H	-0.001988	-4.408578	2.467856				
H	2.162674	-3.619021	1.502713				
C	-2.475754	-1.524249	-0.398198				
C	-2.354201	-1.992494	-1.875757				
C	-3.791168	-2.054385	0.190237				
C	0.001494	2.800271	0.638448				
C	0.002516	4.315958	0.409507				
C	0.000941	2.542766	2.172588				
C	2.473827	-1.526940	-0.399251				
C	2.350684	-1.993575	-1.877190				
C	3.788824	-2.059587	0.187789				
H	-2.406016	-3.090722	-1.930302				

Table A.11: Optimized geometry of **DTPB** in the S_0 state.

Atoms	X (Å)	Y (Å)	Z (Å)	Atoms	X (Å)	Y (Å)	Z (Å)
C	-7.085105	3.664452	-0.644415	C	5.636240	1.172591	0.105802
C	-7.729935	2.437804	-0.795637	C	5.586110	-1.177930	-0.557955
C	-5.708279	3.677027	-0.456912	C	4.951509	2.339242	0.519211
C	-7.025009	1.236298	-0.705227	C	6.958710	1.284473	-0.382245
C	-4.966441	2.493801	-0.336195	C	5.516793	3.591285	0.256486
C	-5.644901	1.258604	-0.378638	C	7.490433	2.554113	-0.629968
N	-4.974860	0.042109	-0.098911	C	6.764794	3.708918	-0.349764
C	-5.737985	-1.113164	0.202097	C	6.908275	-1.070039	-1.047656
C	-3.579288	0.043356	0.128573	C	4.850996	-2.360036	-0.808686
C	-7.117186	-1.144466	-0.128228	C	7.391581	-2.041983	-1.929589
C	-7.910063	-2.199390	0.326849	C	5.368543	-3.310506	-1.694653
C	-7.356427	-3.261441	1.040120	C	6.617431	-3.142713	-2.287084
C	-5.982937	-3.282090	1.248923	H	0.975540	1.953813	1.057304
C	-5.153941	-2.232265	0.829802	H	0.888804	-2.145023	-0.150016
C	-2.818791	1.222170	-0.050662	C	3.589844	-2.619488	-0.001894
C	-1.426141	1.157328	0.026051	C	3.691665	2.188340	1.355686
C	-0.734957	-0.022218	0.320020	C	7.802119	0.025728	-0.492503
C	-2.912195	-1.136063	0.535852	H	4.980446	4.493453	0.545844
C	-1.518134	-1.146779	0.601881	H	8.497346	2.644685	-1.034078
H	-7.645287	4.599105	-0.715141	H	7.187835	4.693594	-0.559779
H	-8.795984	2.421249	-1.016330	H	8.398393	-1.947366	-2.333018
H	-5.187376	4.634226	-0.409345	H	4.793231	-4.208286	-1.914627
C	-3.449532	2.594802	-0.258617	H	7.003085	-3.887446	-2.986581
C	-7.651455	-0.094465	-1.088481	C	4.122059	1.775046	2.790986
H	-8.974597	-2.209877	0.098715	C	2.884144	3.487216	1.457560
H	-7.985123	-4.081436	1.393275	C	8.223683	-0.389634	0.945066
H	-5.534414	-4.141351	1.749296	C	9.076220	0.231976	-1.319039
H	-0.854314	2.065887	-0.160557	C	2.729489	-3.746539	-0.583944
C	0.743256	-0.066575	0.368264	C	4.022523	-3.036180	1.432054
C	-3.649800	-2.384995	1.006911	H	4.740979	2.565116	3.244100
H	-1.021936	-2.060944	0.926198	H	4.708429	0.844731	2.777532
C	1.497929	1.054717	0.738739	H	3.233889	1.612904	3.421486
C	1.448888	-1.244875	0.092689	H	2.006342	3.348263	2.103010
C	2.892366	1.040371	0.762809	H	3.485171	4.282044	1.919374
C	2.843186	-1.301194	0.108524	H	7.344802	-0.551266	1.586124
C	3.583419	-0.122034	0.350164	H	8.842243	0.398589	1.401926
N	4.996524	-0.101381	0.170096	H	8.804033	-1.325003	0.914983

Table A.11 (continued)

Atoms	X (Å)	Y (Å)	Z (Å)	Atoms	X (Å)	Y (Å)	Z (Å)
H	9.675314	-0.688355	-1.342915				
H	9.711379	1.004527	-0.864932				
H	8.851427	0.529040	-2.354198				
H	1.849696	-3.928041	0.048198				
H	3.292240	-4.689367	-0.610137				
H	2.385124	-3.516798	-1.603164				
H	4.605201	-3.969869	1.396470				
H	3.135469	-3.193632	2.065334				
H	4.645334	-2.260157	1.900411				
C	-2.939613	3.211088	-1.585686				
C	-3.041627	3.502743	0.928341				
C	-9.182890	-0.042801	-1.121055				
C	-7.153167	-0.459398	-2.515336				
C	-3.320704	-2.609638	2.504126				
C	-3.185136	-3.610681	0.181156				
H	2.541329	3.836206	0.472157				
H	-3.215562	2.571563	-2.437409				
H	-1.845494	3.322638	-1.579497				
H	-3.377517	4.206676	-1.748546				
H	-1.948483	3.603259	0.990041				
H	-3.401336	3.079071	1.877893				
H	-3.462317	4.512739	0.820260				
H	-9.606968	0.211211	-0.138145				
H	-9.596400	-1.009261	-1.439550				
H	-9.529668	0.699779	-1.852338				
H	-7.555361	-1.438812	-2.818065				
H	-6.055488	-0.512581	-2.552939				
H	-7.485521	0.301119	-3.239086				
H	-3.824295	-3.507433	2.890848				
H	-3.647595	-1.746514	3.103046				
H	-2.239554	-2.741633	2.654960				
H	-2.103414	-3.777112	0.288458				
H	-3.406395	-3.461361	-0.886242				
H	-3.697721	-4.525099	0.513064				

Table A.12: Optimized geometry of **DTPA** in the S_1 state.

Atoms	X (Å)	Y (Å)	Z (Å)	Atoms	X (Å)	Y (Å)	Z (Å)
C	3.905752	1.414119	-0.655340	H	0.959538	4.512176	-0.641853
C	3.633108	0.052172	-0.686716	H	1.821206	4.541630	0.920695
C	2.912608	2.312826	-0.233011	H	1.439872	2.799258	2.661427
C	2.376200	-0.459287	-0.339033	H	0.258769	1.485749	2.415460
C	1.638578	1.863312	0.089322	H	-0.313400	3.162092	2.620893
C	1.341236	0.474758	-0.031131	H	3.100607	-2.227314	-2.287901
N	0.014114	0.036977	0.066065	H	1.324925	-2.051636	-2.342011
C	-0.276372	-1.350271	0.096956	H	2.049766	-3.584434	-1.782536
C	-1.028494	0.963623	-0.058250	H	4.278869	-2.414053	0.032703
C	0.801634	-2.288613	0.282778	H	3.189174	-3.736753	0.448268
C	0.521853	-3.516201	0.857144	H	3.301478	-2.317778	1.522693
C	-0.793954	-3.873336	1.235756	H	-3.885696	-0.921355	-2.141513
C	-1.858061	-3.006323	0.918413	H	-3.475766	-2.553053	-1.538527
C	-1.640787	-1.768590	0.334798	H	-2.212218	-1.527691	-2.274464
C	-0.753674	2.359027	0.033589	H	-3.804931	-0.625193	1.669296
C	-1.724045	3.267835	-0.363869	H	-4.393145	-2.036035	0.750165
C	-2.975312	2.823683	-0.833886	H	-4.847076	-0.406193	0.236792
C	-2.345394	0.509475	-0.387429				
C	-3.273088	1.466747	-0.818457				
H	4.896966	1.782450	-0.927676				
H	4.425401	-0.638289	-0.976961				
H	3.152610	3.371434	-0.153744				
H	1.320875	-4.248496	0.983443				
H	-0.987308	-4.831258	1.722572				
H	-2.881420	-3.344394	1.095684				
H	-1.526290	4.336676	-0.307064				
H	-3.721314	3.546865	-1.169806				
H	-4.267275	1.139453	-1.126796				
C	0.567578	2.782793	0.650838				
C	0.879540	4.266004	0.427034				
C	0.481976	2.537428	2.186987				
C	2.157477	-1.962922	-0.311516				
C	2.160784	-2.490161	-1.777210				
C	3.299287	-2.643850	0.472128				
C	-2.770252	-0.938369	-0.235523				
C	-3.110107	-1.520667	-1.638865				
C	-4.027953	-1.003034	0.660508				
H	0.096276	4.894235	0.872214				

Appendix B

Coordinates of the computationally optimized structures for Chapter 4

Table B.1: Optimized geometry of **4Br-TIPS-TAP** in the S_0 state.

Atoms	X (Å)	Y (Å)	Z (Å)	Atoms	X (Å)	Y (Å)	Z (Å)
Br	7.737820	1.693442	0.019808	H	-0.658911	8.617063	1.492113
Br	7.738062	-1.692325	0.019821	H	0.388435	8.383480	2.904510
Br	-7.423328	1.692597	-0.083264	C	-1.117167	6.073234	2.670984
Br	-7.423090	-1.693630	-0.083262	H	-1.274431	4.985759	2.597191
Si	-0.117839	5.914959	-0.023933	H	-0.912827	6.313454	3.728654
Si	-0.116765	-5.914988	-0.023935	H	-2.066406	6.565627	2.405268
C	6.111241	0.724815	0.025317	C	1.325882	6.585397	-1.070811
C	6.111345	-0.723931	0.025323	H	1.237241	7.687976	-1.060197
C	4.930927	-1.417853	0.029117	C	1.245920	6.111127	-2.528995
H	4.910705	-2.507590	0.028784	H	0.328508	6.457515	-3.029763
C	3.676841	-0.726542	0.033293	H	2.103180	6.485795	-3.114519
C	1.384030	-0.727947	0.037545	H	1.262060	5.010042	-2.588707
C	0.157969	-1.451101	0.035894	C	2.673414	6.201066	-0.438532
C	-1.069505	-0.727565	0.022371	H	2.786093	6.605093	0.579801
C	-3.363769	-0.726782	-0.011567	H	2.777391	5.104926	-0.372940
C	-4.616831	-1.419331	-0.033880	H	3.516473	6.582103	-1.040374
H	-4.598237	-2.509135	-0.035761	C	-1.793753	6.219343	-0.880408
C	-5.796876	-0.724749	-0.054145	H	-1.606776	5.878761	-1.915771
C	-5.796977	0.723945	-0.054146	C	-2.170600	7.707010	-0.937068
C	-4.617030	1.418692	-0.033882	H	-4.598588	2.508499	-0.035765
H	1.091543	8.415691	1.273409	C	-3.363871	0.726318	-0.011569

Table B.1 (continued)

Atoms	X (Å)	Y (Å)	Z (Å)	Atoms	X (Å)	Y (Å)	Z (Å)
C	-1.069608	0.727422	0.022366	H	0.390238	-8.383445	2.904434
C	0.157761	1.451133	0.035886	H	-0.657123	-8.617242	1.492084
C	1.383926	0.728156	0.037544	C	-1.792655	-6.219734	-0.880329
C	3.676737	0.727079	0.033288	H	-1.605810	-5.879057	-1.915684
C	4.930724	1.418568	0.029107	C	-2.938557	-5.359263	-0.323903
H	4.910347	2.508303	0.028766	H	-2.666605	-4.292953	-0.285178
C	0.143746	2.862527	0.040092	H	-3.841015	-5.461672	-0.952211
C	0.080854	4.083761	0.037895	H	-3.218129	-5.668662	0.695321
C	0.029288	6.549750	1.768272	C	-2.169158	-7.707486	-0.937044
H	0.957579	6.068760	2.128749	H	-1.359044	-8.329597	-1.351488
C	0.224837	8.070700	1.858632	H	-2.405860	-8.098852	0.065784
H	-1.360619	8.329327	-1.351463	H	-3.062512	-7.867493	-1.565077
H	-3.063975	7.866839	-1.565118	N	2.543317	1.414331	0.035626
H	-2.407418	8.098274	0.065772	N	2.543518	-1.413956	0.035634
C	-2.939483	5.358576	-0.324083	N	-2.229526	1.411909	0.005760
H	-2.667292	4.292325	-0.285413	N	-2.229328	-1.412213	0.005766
H	-3.219165	5.667847	0.695150				
H	-3.841938	5.460820	-0.952419				
C	0.144158	-2.862497	0.040101				
C	0.081510	-4.083744	0.037907				
C	1.327048	-6.585083	-1.070907				
H	1.238665	-7.687681	-1.060300				
C	1.246885	-6.110814	-2.529081				
H	0.329530	-6.457425	-3.029800				
H	1.262746	-5.009725	-2.588779				
H	2.104204	-6.485262	-3.114658				
C	2.674529	-6.200445	-0.438706				
H	2.787363	-6.604455	0.579616				
H	3.517640	-6.581281	-1.040603				
H	2.778256	-5.104282	-0.373111				
C	0.030608	-6.549775	1.768251				
H	0.958808	-6.068577	2.128685				
C	-1.115908	-6.073542	2.671037				
H	-1.273434	-4.986104	2.597268				
H	-2.065045	-6.566156	2.405370				
H	-0.911448	-6.313729	3.728692				
C	0.226515	-8.070682	1.858571				
H	1.093273	-8.415459	1.273297				

Table B.2: Optimized geometry of **4Br-TIPS-TAP**$^{\cdot+}$.

Atoms	X (Å)	Y (Å)	Z (Å)	Atoms	X (Å)	Y (Å)	Z (Å)
Br	-7.461215	-1.687159	-0.017896	H	1.715529	-5.278217	2.256224
Br	-7.460324	1.691098	-0.018084	H	1.298915	-6.478767	3.502860
Br	7.695546	-1.690899	-0.066072	H	2.024720	-7.006332	1.974685
Br	7.696447	1.686761	-0.066140	C	-1.978618	-6.150894	-0.667523
Si	-0.211022	-5.917666	-0.004404	H	-2.170419	-7.239424	-0.633903
Si	-0.206912	5.917859	-0.004502	C	-2.114142	-5.684237	-2.124592
C	-5.846659	-0.721566	-0.007260	H	-1.443248	-6.231485	-2.804155
C	-5.846277	0.724658	-0.007339	H	-3.143970	-5.834737	-2.489346
C	-4.658050	1.420732	0.000361	H	-1.885647	-4.609406	-2.221270
H	-4.640944	2.510653	-0.000203	C	-3.004994	-5.449447	0.237178
C	-3.416379	0.726754	0.008191	H	-2.978111	-5.824647	1.271835
C	-1.125367	0.723446	0.018243	H	-2.820598	-4.362450	0.270231
C	0.119569	1.452096	0.019729	H	-4.029384	-5.606189	-0.141579
C	1.361989	0.723302	0.009115	C	1.107307	-6.598321	-1.193399
C	3.651419	0.725126	-0.016630	H	0.783478	-6.212016	-2.177354
C	4.893883	1.417375	-0.032068	C	1.076799	-8.133708	-1.258986
H	4.875959	2.507209	-0.032096	H	0.067043	-8.526505	-1.459550
C	6.082180	0.721414	-0.046478	H	1.738234	-8.503225	-2.060061
C	6.081794	-0.724691	-0.046449	H	1.427718	-8.582837	-0.316227
C	4.893125	-1.420016	-0.032009	C	2.523681	-6.062762	-0.934328
H	4.874614	-2.509840	-0.031993	H	2.547257	-4.962499	-0.888825
C	3.651031	-0.727103	-0.016601	H	2.934502	-6.443352	0.013045
C	1.361603	-0.724053	0.009148	H	3.208785	-6.382713	-1.737318
C	0.118795	-1.452178	0.019799	C	0.106286	2.842916	0.025701
C	-1.125751	-0.722856	0.018291	C	0.039221	4.071521	0.024450
C	-3.416765	-0.724944	0.008261	C	-1.973741	6.152769	-0.669065
C	-4.658801	-1.418268	0.000511	H	-2.164607	7.241462	-0.635414
H	-4.642267	-2.508197	0.000067	C	-2.108460	5.686492	-2.126331
C	0.104721	-2.842991	0.025810	H	-1.436548	6.233303	-2.805239
C	0.036779	-4.071548	0.024570	H	-1.880785	4.611489	-2.223030
C	-0.090728	-6.459934	1.821061	H	-3.137860	5.837923	-2.491902
H	-0.768295	-5.761390	2.345039	C	-3.001482	5.452083	0.234677
C	-0.631206	-7.883858	2.029342	H	-2.975125	5.827123	1.269406
H	-1.665588	-7.9978	1.670411	H	-4.025417	5.609767	-0.144912
H	-0.014254	-8.634551	1.511482	H	-2.818063	4.364919	0.267745
H	-0.625591	-8.142127	3.101644	C	-0.087701	6.459730	1.821159
C	1.313519	-6.290993	2.416265	H	-0.766353	5.761718	2.344442

Table B.2 (continued)

Atoms	X (Å)	Y (Å)	Z (Å)	Atoms	X (Å)	Y (Å)	Z (Å)
C	1.315880	6.289430	2.417547				
H	1.717099	5.276305	2.257735				
H	2.028118	7.004164	1.976659				
H	1.300517	6.477095	3.504150				
C	-0.627070	7.884110	2.029192				
H	-1.661038	7.999043	1.669385				
H	-0.622149	8.142209	3.101538				
H	-0.008993	8.634326	1.511982				
C	1.113060	6.597498	-1.192243				
H	0.789674	6.211733	-2.176557				
C	2.528688	6.060473	-0.932111				
H	2.551132	4.960176	-0.886843				
H	3.214783	6.379936	-1.734448				
H	2.939087	6.440434	0.015698				
C	1.084134	8.132929	-1.257521				
H	0.074932	8.526773	-1.458822				
H	1.434731	8.581508	-0.314380				
H	1.746589	8.501962	-2.057976				
N	-2.270659	-1.409258	0.014729				
N	-2.269909	1.410460	0.014611				
N	2.505434	-1.412606	-0.003746				
N	2.506189	1.411241	-0.003805				

Table B.3: Optimized geometry of **4Br-TIPS-TAP**$^{\bullet-}$.

Atoms	X (Å)	Y (Å)	Z (Å)	Atoms	X (Å)	Y (Å)	Z (Å)
Br	-7.780612	-1.704628	0.032430	H	1.235403	-5.033146	2.616859
Br	-7.780411	1.705558	0.032426	H	0.891884	-6.398763	3.711198
Br	7.427717	-1.705949	-0.071591	H	2.064075	-6.589163	2.391702
Br	7.427916	1.705092	-0.071592	C	-1.271762	-6.587812	-1.119061
Si	0.134588	-5.881168	-0.036075	H	-1.161417	-7.689026	-1.123035
Si	0.135476	5.881142	-0.036065	C	-1.178043	-6.088269	-2.567589
C	-6.152276	-0.713469	0.039056	H	-0.246570	-6.410987	-3.059087
C	-6.152192	0.714207	0.039054	H	-2.020890	-6.464379	-3.174602
C	-4.959915	1.407779	0.043673	H	-1.208493	-4.986763	-2.604915
H	-4.939933	2.497721	0.043419	C	-2.637363	-6.235086	-0.507518
C	-3.714012	0.721022	0.048692	H	-2.761479	-6.656536	0.502860
C	-1.415712	0.732553	0.055344	H	-2.756575	-5.141813	-0.425129
C	-0.176917	1.440936	0.055022	H	-3.465465	-6.618156	-1.130180
C	1.062626	0.732037	0.039225	C	1.831251	-6.160473	-0.869168
C	3.363240	0.720394	0.003162	H	1.650322	-5.817144	-1.9048
C	4.608408	1.407857	-0.019801	C	2.247907	-7.636373	-0.931466
H	4.592009	2.497747	-0.021429	H	1.458334	-8.277799	-1.357488
C	5.800231	0.713337	-0.041219	H	3.153482	-7.771095	-1.549683
C	5.800148	-0.714004	-0.041218	H	2.483966	-8.027897	0.072012
C	4.608244	-1.408385	-0.019800	C	2.945790	-5.271857	-0.293579
H	4.591719	-2.498273	-0.021427	H	2.643491	-4.2137	-0.252707
C	3.363156	-0.720777	0.003162	H	3.219033	-5.578780	0.728720
C	1.062540	-0.732152	0.039229	H	3.861120	-5.345639	-0.908445
C	-0.177088	-1.440904	0.055025	C	-0.161524	2.853781	0.059769
C	-1.415798	-0.732374	0.055342	C	-0.096915	4.076517	0.058186
C	-3.714097	-0.720571	0.048694	C	-1.270823	6.588082	-1.118922
C	-4.960081	-1.407181	0.043676	H	-1.160261	7.689275	-1.122887
H	-4.940227	-2.497126	0.043425	C	-1.177324	6.088546	-2.567467
C	-0.161865	-2.853751	0.059778	H	-0.245827	6.411085	-3.059036
C	-0.097458	-4.076498	0.058189	H	-1.208000	4.987046	-2.604810
C	-0.024022	-6.596135	1.730492	H	-2.020145	6.464836	-3.174404
H	-0.964127	-6.140621	2.093621	C	-2.636444	6.235616	-0.507271
C	-0.194396	-8.121003	1.776724	H	-2.760393	6.657076	0.503124
H	-1.049020	-8.462383	1.171406	H	-3.464522	6.618859	-1.129858
H	0.701740	-8.641830	1.402148	H	-2.755864	5.142365	-0.424888
H	-0.362856	-8.470474	2.811390	C	-0.022846	6.596110	1.730528
C	1.101249	-6.125103	2.661556	H	-0.963013	6.140779	2.093727

Table B.3 (continued)

Atoms	X (Å)	Y (Å)	Z (Å)	Atoms	X (Å)	Y (Å)	Z (Å)
C	1.102407	6.124836	2.661491				
H	1.236338	5.032853	2.616764				
H	2.065304	6.588708	2.391566				
H	0.893184	6.398520	3.711155				
C	-0.192908	8.121012	1.776800				
H	-1.047513	8.462575	1.171559				
H	-0.361210	8.470501	2.811486				
H	0.703303	8.641665	1.402158				
C	1.832126	6.160128	-0.869292				
H	1.651041	5.816866	-1.904918				
C	2.946534	5.271271	-0.293824				
H	2.644033	4.213170	-0.252979				
H	3.861834	5.344902	-0.908754				
H	3.219912	5.578095	0.728469				
C	2.249072	7.635946	-0.931580				
H	1.459595	8.277542	-1.357525				
H	2.485284	8.027394	0.071891				
H	3.154627	7.770505	-1.549862				
N	-2.566166	-1.417501	0.051832				
N	-2.565999	1.417816	0.051831				
N	2.213973	-1.415878	0.021386				
N	2.214138	1.415629	0.021383				

Table B.4: Optimized geometry of **4I-TIPS-TAP** in the S_0 state.

Atoms	X (Å)	Y (Å)	Z (Å)	Atoms	X (Å)	Y (Å)	Z (Å)
I	-7.893037	-1.854168	0.005364	H	1.281237	-4.973411	2.610283
I	-7.893046	1.854127	0.005368	H	0.921911	-6.302356	3.741019
I	7.605682	-1.854599	-0.068276	H	2.085461	-6.547829	2.425067
I	7.605672	1.854638	-0.068276	C	-1.283684	-6.595980	-1.072571
Si	0.148069	-5.913772	-0.016980	H	-1.185841	-7.697788	-1.061479
Si	0.148012	5.913773	-0.016980	C	-1.198725	-6.120900	-2.530220
C	-6.101602	-0.724339	0.015975	H	-0.275382	-6.459519	-3.025378
C	-6.101605	0.724306	0.015976	H	-2.049232	-6.502616	-3.121022
C	-4.917977	1.416147	0.022682	H	-1.223680	-5.019984	-2.589944
H	-4.886441	2.505817	0.022525	C	-2.638225	-6.223032	-0.448588
C	-3.662760	0.725952	0.029781	H	-2.753826	-6.628074	0.569005
C	-1.370446	0.728260	0.039166	H	-2.751802	-5.127837	-0.383560
C	-0.144319	1.451316	0.040171	H	-3.474421	-6.610839	-1.055646
C	1.083232	0.727666	0.029497	C	1.831767	-6.207548	-0.862007
C	3.377174	0.725693	0.000417	H	1.649056	-5.870252	-1.899210
C	4.631480	1.417004	-0.019699	C	2.219758	-7.692540	-0.913452
H	4.601873	2.506737	-0.021373	H	1.417037	-8.321579	-1.331830
C	5.814689	0.724301	-0.038309	H	3.118307	-7.846937	-1.535462
C	5.814693	-0.724272	-0.038309	H	2.453051	-8.080159	0.091635
C	4.631488	-1.416982	-0.019699	C	2.967526	-5.337382	-0.299877
H	4.601886	-2.506715	-0.021373	H	2.686767	-4.273293	-0.264495
C	3.377178	-0.725678	0.000417	H	3.243219	-5.642969	0.721550
C	1.083235	-0.727662	0.029495	H	3.874733	-5.433445	-0.922306
C	-0.144311	-1.451319	0.040170	C	-0.129566	2.862703	0.044209
C	-1.370442	-0.728269	0.039168	C	-0.063159	4.083788	0.042081
C	-3.662757	-0.725973	0.029780	C	-1.283742	6.595965	-1.072581
C	-4.917970	-1.416174	0.022679	H	-1.185911	7.697774	-1.061487
H	-4.886429	-2.505844	0.022520	C	-1.198767	6.120887	-2.530229
C	-0.129551	-2.862706	0.044209	H	-0.275427	6.459522	-3.025382
C	-0.063128	-4.083791	0.042081	H	-1.223704	5.019971	-2.589953
C	-0.006256	-6.547450	1.775054	H	-2.049277	6.502589	-3.121036
H	-0.940154	-6.072454	2.128956	C	-2.638283	6.223003	-0.448608
C	-0.191824	-8.069602	1.866182	H	-2.753897	6.628044	0.568983
H	-1.052200	-8.421422	1.275696	H	-3.474479	6.610799	-1.055673
H	0.698124	-8.610277	1.506295	H	-2.751848	5.127807	-0.383580
H	-0.360179	-8.382127	2.911392	C	-0.006333	6.547446	1.775053
C	1.131144	-6.061874	2.684360	H	-0.940230	6.072443	2.128946

Table B.4 (continued)

Atoms	X (Å)	Y (Å)	Z (Å)	Atoms	X (Å)	Y (Å)	Z (Å)
C	1.131065	6.061878	2.684367				
H	1.281164	4.973417	2.610292				
H	2.085380	6.547838	2.425079				
H	0.921823	6.302361	3.741025				
C	-0.191912	8.069597	1.866182				
H	-1.052285	8.421412	1.275690				
H	-0.360278	8.382120	2.911390				
H	0.698035	8.610279	1.506302				
C	1.831711	6.207569	-0.861997				
H	1.649014	5.870254	-1.899196				
C	2.967481	5.337433	-0.299842				
H	2.686740	4.273341	-0.264442				
H	3.874691	5.433501	-0.922266				
H	3.243160	5.643045	0.721581				
C	2.219674	7.692567	-0.913461				
H	1.416944	8.321586	-1.331853				
H	2.452955	8.080206	0.091622				
H	3.118224	7.846972	-1.535468				
N	-2.529760	-1.414361	0.034686				
N	-2.529767	1.414345	0.034688				
N	2.243047	-1.412148	0.015476				
N	2.243039	1.412158	0.015477				

Table B.5: Optimized geometry of **4I-TIPS-TAP**$^{\cdot+}$.

Atoms	X (Å)	Y (Å)	Z (Å)	Atoms	X (Å)	Y (Å)	Z (Å)
I	-7.594897	-1.850758	-0.011514	H	1.861620	-5.411068	2.056433
I	-7.594914	1.850690	-0.011514	H	1.514619	-6.624964	3.311436
I	7.901278	-1.849981	-0.029541	H	2.064211	-7.142874	1.708244
I	7.901260	1.850059	-0.029541	C	-2.137425	-6.029210	-0.503424
Si	-0.303124	-5.901383	-0.014375	H	-2.376041	-7.109011	-0.497578
Si	-0.303228	5.901374	-0.014377	C	-2.395897	-5.486534	-1.917026
C	-5.815224	-0.722985	0.001850	H	-1.818949	-6.023205	-2.685489
C	-5.815231	0.722933	0.001850	H	-3.462168	-5.580615	-2.183078
C	-4.623519	1.417251	0.010950	H	-2.133495	-4.417352	-1.984730
H	-4.595106	2.507079	0.011653	C	-3.035716	-5.326820	0.527712
C	-3.380673	0.724955	0.019598	H	-2.926917	-5.749426	1.538346
C	-1.089570	0.723404	0.031968	H	-2.796815	-4.251824	0.585621
C	0.155027	1.452429	0.033841	H	-4.098844	-5.420666	0.246809
C	1.396764	0.724241	0.027214	C	0.849681	-6.615058	-1.348193
C	3.685783	0.725362	0.008385	H	0.451873	-6.181644	-2.284191
C	4.929354	1.416154	-0.002869	C	0.725051	-8.143691	-1.448997
H	4.899439	2.505908	-0.002681	H	-0.320441	-8.474989	-1.554990
C	6.121759	0.722899	-0.013492	H	1.280355	-8.523276	-2.322730
C	6.121766	-0.722837	-0.013492	H	1.143199	-8.640040	-0.558834
C	4.929368	-1.416104	-0.002868	C	2.313032	-6.166188	-1.220297
H	4.899463	-2.505858	-0.002681	H	2.404663	-5.070949	-1.149571
C	3.685790	-0.725324	0.008385	H	2.793588	-6.597704	-0.329276
C	1.396771	-0.724225	0.027214	H	2.895558	-6.497814	-2.096195
C	0.155041	-1.452426	0.033842	C	0.134973	2.844032	0.034907
C	-1.089563	-0.723412	0.031969	C	0.037358	4.070357	0.027050
C	-3.380666	-0.724985	0.019597	C	-2.137525	6.029150	-0.503456
C	-4.623506	-1.417292	0.010949	H	-2.376173	7.108945	-0.497609
H	-4.595083	-2.507119	0.011652	C	-2.395958	5.486472	-1.917064
C	0.135002	-2.844029	0.034908	H	-1.819013	6.023163	-2.685516
C	0.037412	-4.070356	0.027052	H	-2.133524	4.417298	-1.984768
C	-0.029478	-6.502870	1.774537	H	-3.462228	5.580524	-2.183134
H	-0.620623	-5.792013	2.380376	C	-3.035813	5.326729	0.527662
C	-0.610201	-7.908136	2.000715	H	-2.927042	5.749332	1.538300
H	-1.677795	-7.969109	1.739058	H	-4.098939	5.420547	0.246743
H	-0.078589	-8.669246	1.408733	H	-2.796884	4.251740	0.585569
H	-0.515104	-8.196100	3.061168	C	-0.029628	6.502864	1.774540
C	1.432058	-6.409721	2.232986	H	-0.620763	5.791989	2.380368

Table B.5 (continued)

Atoms	X (Å)	Y (Å)	Z (Å)	Atoms	X (Å)	Y (Å)	Z (Å)
C	-0.610394	7.908113	2.000713				
H	-1.677985	7.969057	1.739040				
H	-0.515322	8.196077	3.061168				
H	-0.078794	8.669240	1.408741				
C	0.849578	6.615086	-1.348174				
H	0.451797	6.181664	-2.284180				
C	2.312939	6.166255	-1.220256				
H	2.404599	5.071018	-1.149533				
H	2.895471	6.497902	-2.096142				
H	2.793468	6.597780	-0.329225				
C	0.724907	8.143715	-1.448974				
H	-0.320592	8.474985	-1.554983				
H	1.143028	8.640073	-0.558802				
H	1.280216	8.523319	-2.322697				
N	-2.234519	-1.409683	0.027310				
N	-2.234532	1.409664	0.027309				
N	2.540855	-1.412548	0.017574				
N	2.540841	1.412575	0.017574				
C	1.431903	6.409755	2.233012				
H	1.861496	5.411114	2.056464				
H	2.064045	7.142925	1.708280				
H	1.514442	6.624999	3.311463				

Table B.6: Optimized geometry of **4I-TIPS-TAP**$^{\bullet-}$.

Atoms	X (Å)	Y (Å)	Z (Å)	Atoms	X (Å)	Y (Å)	Z (Å)
I	-7.927559	-1.864455	0.016634	H	1.250894	-5.023140	2.624800
I	-7.927560	1.864451	0.016634	H	0.909922	-6.389061	3.719494
I	7.610993	-1.865148	-0.057111	H	2.088511	-6.575069	2.405079
I	7.610992	1.865151	-0.057111	C	-1.232851	-6.595808	-1.119489
Si	0.165324	-5.881028	-0.031539	H	-1.115367	-7.696280	-1.123021
Si	0.165319	5.881028	-0.031539	C	-1.136909	-6.095743	-2.567704
C	-6.136873	-0.713854	0.028602	H	-0.201557	-6.412471	-3.055695
C	-6.136874	0.713851	0.028602	H	-1.975047	-6.477303	-3.177788
C	-4.941921	1.406272	0.036197	H	-1.174319	-4.994458	-2.605326
H	-4.911294	2.496099	0.036104	C	-2.602958	-6.252101	-0.513019
C	-3.695212	0.720113	0.044160	H	-2.728081	-6.674213	0.496935
C	-1.397512	0.732656	0.055932	H	-2.729796	-5.159662	-0.431255
C	-0.159053	1.441317	0.058194	H	-3.426228	-6.640545	-1.138695
C	1.080307	0.732248	0.045422	C	1.866678	-6.151931	-0.857646
C	3.380485	0.719897	0.014399	H	1.688260	-5.809844	-1.894131
C	4.626416	1.406932	-0.006310	C	2.290746	-7.625833	-0.917773
H	4.599338	2.496707	-0.007767	H	1.506206	-8.271250	-1.347051
C	5.821065	0.713676	-0.025917	H	3.199612	-7.756111	-1.532048
C	5.821066	-0.713674	-0.025917	H	2.524458	-8.015919	0.086805
C	4.626417	-1.406930	-0.006311	C	2.974542	-5.257722	-0.277824
H	4.599339	-2.496705	-0.007767	H	2.666268	-4.201290	-0.237918
C	3.380485	-0.719895	0.014399	H	3.245743	-5.563346	0.745384
C	1.080307	-0.732248	0.045422	H	3.892526	-5.326300	-0.889234
C	-0.159053	-1.441317	0.058194	C	-0.143105	2.854264	0.062446
C	-1.397511	-0.732657	0.055932	C	-0.076017	4.076812	0.060353
C	-3.695211	-0.720115	0.044160	C	-1.232857	6.595806	-1.119490
C	-4.941920	-1.406274	0.036197	H	-1.115374	7.696278	-1.123022
H	-4.911292	-2.496102	0.036103	C	-1.136914	6.095740	-2.567704
C	-0.143104	-2.854264	0.062446	H	-0.201563	6.412470	-3.055695
C	-0.076014	-4.076812	0.060353	H	-1.174322	4.994455	-2.605326
C	0.003198	-6.593932	1.735409	H	-1.975053	6.477299	-3.177788
H	-0.940845	-6.143033	2.094062	C	-2.602964	6.252097	-0.513020
C	-0.159138	-8.119657	1.782877	H	-2.728088	6.674210	0.496934
H	-1.009403	-8.466476	1.174523	H	-3.426234	6.640540	-1.138697
H	0.741363	-8.636057	1.412689	H	-2.729801	5.159658	-0.431256
H	-0.329951	-8.468641	2.817300	C	0.003191	6.593933	1.735408
C	1.122193	-6.115712	2.670376	H	-0.940852	6.143033	2.094062

Table B.6 (continued)

Atoms	X (Å)	Y (Å)	Z (Å)	Atoms	X (Å)	Y (Å)	Z (Å)
C	-0.159147	8.119658	1.782876				
H	-1.009413	8.466475	1.174522				
H	-0.329961	8.468642	2.817299				
H	0.741353	8.636058	1.412688				
C	1.866672	6.151933	-0.857646				
H	1.688255	5.809846	-1.894130				
C	2.974538	5.257727	-0.277823				
H	2.666266	4.201294	-0.237916				
H	3.892522	5.326306	-0.889233				
H	3.245737	5.563351	0.745385				
C	2.290738	7.625836	-0.917774				
H	1.506197	8.271252	-1.347052				
H	2.524449	8.015923	0.086804				
H	3.199605	7.756115	-1.532049				
N	-2.547878	-1.417810	0.049935				
N	-2.547879	1.417809	0.049935				
N	2.231888	-1.415831	0.030281				
N	2.231887	1.415832	0.030281				
C	1.122187	6.115715	2.670376				
H	1.250889	5.023143	2.624801				
H	2.088504	6.575073	2.405079				
H	0.909915	6.389064	3.719494				

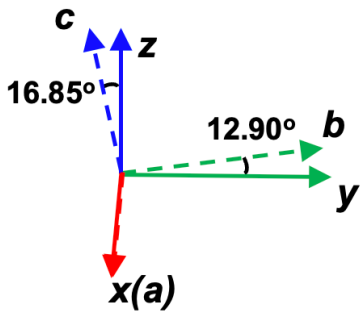

Figure B.1: Relative orientation between the Cartesian axes (x, y, z) and crystallographic axes (a, b, c) for **4Br-TIPS-TAP**.

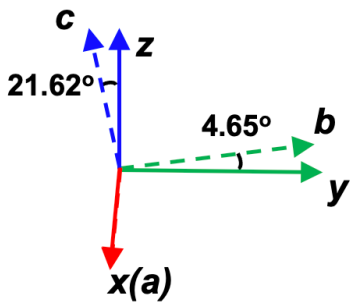

Figure B.2: Relative orientation between the Cartesian axes (x, y, z) and crystallographic axes (a, b, c) for **4I-TIPS-TAP**.

Appendix C

Coordinates of the computationally optimized structures for Chapter 5

Table C.1: Optimized geometry of **DPND** in the S_0 state.

Atoms	X (Å)	Y (Å)	Z (Å)	Atoms	X (Å)	Y (Å)	Z (Å)
O	-3.839412	-0.104817	17.820786	H	-4.332892	-2.195757	22.862135
O	0.652550	0.104817	21.857429	H	-0.642976	2.282440	14.757571
N	-1.779912	0.821526	17.469827	H	-2.543885	-2.282442	24.920643
N	-1.406950	-0.821525	22.208388	H	-2.919713	1.056408	15.681393
C	-0.921955	0.178711	20.051739	H	-0.267148	-1.056409	23.996822
C	-2.264907	-0.178710	19.626477				
C	-0.067472	0.830370	19.197139				
C	-3.119390	-0.830369	20.481077				
C	-0.486443	1.163485	17.885364				
C	-2.700419	-1.163485	21.792851				
C	0.130255	1.805638	16.812317				
C	-3.317117	-1.805638	22.865898				
C	-0.803681	1.849136	15.742416				
C	-2.383180	-1.849138	23.935799				
C	-1.967974	1.238135	16.172426				
C	-1.218887	-1.238136	23.505789				
C	-2.739568	0.150806	18.267036				
C	-0.447294	-0.150804	21.411180				
H	0.936992	1.090866	19.533347				
H	-4.123853	-1.090865	20.144868				
H	1.146031	2.195756	16.816080				

Table C.2: Optimized geometry of **DPND**$^{\cdot+}$.

Atoms	X (Å)	Y (Å)	Z (Å)
O	-3.836111	-0.114217	17.848950
O	0.649250	0.114217	21.829265
N	-1.778461	0.822882	17.467766
N	-1.408400	-0.822882	22.210449
C	-0.938491	0.176189	20.041426
C	-2.248370	-0.176191	19.636789
C	-0.063714	0.842623	19.168425
C	-3.123147	-0.842624	20.509790
C	-0.484950	1.164272	17.884745
C	-2.701911	-1.164272	21.793471
C	0.138603	1.818046	16.788266
C	-3.325465	-1.818045	22.889949
C	-0.783362	1.859116	15.736527
C	-2.403500	-1.859115	23.941689
C	-1.958925	1.239889	16.177080
C	-1.227937	-1.239889	23.501135
C	-2.738882	0.149530	18.271710
C	-0.447978	-0.149532	21.406504
H	0.940465	1.101401	19.508692
H	-4.127326	-1.101402	20.169523
H	1.155014	2.208419	16.792122
H	-4.341876	-2.208418	22.886094
H	-0.631405	2.289891	14.749227
H	-2.555457	-2.289889	24.928989
H	-2.908695	1.063189	15.674663
H	-0.278166	-1.063188	24.003552

Table C.3: Optimized geometry of **DPND**$^{\cdot-}$.

Atoms	X (Å)	Y (Å)	Z (Å)
O	-3.828504	-0.096016	17.808591
O	0.641642	0.096016	21.869624
N	-1.763072	0.822934	17.483106
N	-1.423790	-0.822934	22.195109
C	-0.926901	0.176552	20.052380
C	-2.259961	-0.176552	19.625836
C	-0.046892	0.839741	19.193184
C	-3.139970	-0.839740	20.485031
C	-0.462145	1.170928	17.890283
C	-2.724717	-1.170927	21.787932
C	0.142356	1.816496	16.795961
C	-3.329217	-1.816497	22.882254
C	-0.806138	1.848966	15.740437
C	-2.380723	-1.848967	23.937778
C	-1.968722	1.235480	16.178602
C	-1.218140	-1.235480	23.499613
C	-2.718447	0.154821	18.277947
C	-0.468415	-0.154820	21.400269
H	0.953522	1.094135	19.541389
H	-4.140384	-1.094135	20.136826
H	1.156868	2.211009	16.786882
H	-4.343730	-2.211009	22.891333
H	-0.657691	2.279668	14.750064
H	-2.529170	-2.279670	24.928150
H	-2.926025	1.045019	15.704978
H	-0.260836	-1.045019	23.973238

Table C.4: Optimized geometry of **DPND6** in the S_0 state.

Atoms	X (Å)	Y (Å)	Z (Å)	Atoms	X (Å)	Y (Å)	Z (Å)
O	2.145214	1.963557	-0.884406	H	-3.252398	1.563809	1.687506
O	-2.145148	-1.963702	0.884512	H	3.252484	-1.564058	-1.687415
N	0.059699	2.506097	-0.204609	H	-3.684200	-0.518737	-0.521678
N	-0.059662	-2.506254	0.204621	H	3.684092	0.518898	0.521428
C	0.190106	3.864738	-0.373399	H	-4.021845	1.214269	-0.664684
C	-0.190011	-3.864880	0.373572	H	4.021814	-1.214064	0.664768
C	-0.989425	4.459797	0.034704	H	-5.354616	-0.720298	1.318932
C	0.989547	-4.459937	-0.034456	H	5.354562	0.720160	-1.319197
C	-1.863387	3.431110	0.475387	H	-5.700465	1.008089	1.224443
C	1.863475	-3.431262	-0.475238	H	5.700525	-1.008180	-1.224283
C	-1.196637	2.213066	0.321499	H	-6.144167	-1.007726	-1.055552
C	1.196683	-2.213226	-0.321467	H	6.144047	1.008302	1.055159
C	1.064275	1.557126	-0.492840	H	-6.491153	0.717867	-1.152355
C	-1.064289	-1.557292	0.492702	H	6.490971	-0.717268	1.152576
C	-1.571575	0.860831	0.582745	H	-7.811156	-1.238005	0.817682
C	1.571586	-0.861001	-0.582817	H	7.811160	1.237772	-0.818161
C	-0.668103	-0.152367	0.270231	H	-8.158197	0.486676	0.722806
C	0.668093	0.152199	-0.270363	H	8.158233	-0.486853	-0.722389
C	-2.956403	0.656685	1.140048	H	-8.640128	-1.543209	-1.558785
C	2.956417	-0.656864	-1.140111	H	-8.989829	0.195868	-1.655149
C	-3.999807	0.369648	0.046433	H	-9.898423	-0.831457	-0.521729
C	3.999765	-0.369577	-0.046507	H	9.898307	0.831887	0.521674
C	-5.395715	0.133739	0.619447	H	8.989571	-0.194824	1.655535
C	5.395686	-0.133708	-0.619508	H	8.639902	1.544206	1.558210
C	-6.453652	-0.135871	-0.450297				
C	6.453550	0.136232	0.450224				
C	-7.852455	-0.385184	0.116325				
C	7.852406	0.385302	-0.116375				
C	-8.903013	-0.655548	-0.959486				
C	8.902844	0.656224	0.959412				
H	1.116761	4.270733	-0.767340				
H	-1.116658	-4.270870	0.767538				
H	-1.200160	5.526961	0.019027				
H	1.200322	-5.527092	-0.018667				
H	-2.871868	3.558371	0.859760				
H	2.871966	-3.558525	-0.859583				
H	-2.957300	-0.176621	1.851081				
H	2.957286	0.176329	-1.851273				

Table C.5: Optimized geometry of **DPND6**$^{\cdot+}$.

Atoms	X (Å)	Y (Å)	Z (Å)	Atoms	X (Å)	Y (Å)	Z (Å)
O	2.145181	1.915977	-0.923441	H	-3.249451	1.621169	1.686020
O	-2.145218	-1.9159	0.923363	H	3.249416	-1.621031	-1.686073
N	0.077683	2.507676	-0.221178	H	-3.650220	-0.461862	-0.540406
N	-0.077705	-2.507593	0.221148	H	3.650285	0.461777	0.540540
C	0.216197	3.859207	-0.396843	H	-4.016318	1.265239	-0.653125
C	-0.216253	-3.859132	0.396722	H	4.016321	-1.265348	0.653089
C	-0.957411	4.481848	0.028941	H	-5.312287	-0.724674	1.303864
C	0.957341	-4.481774	-0.029098	H	5.312326	0.724670	-1.303767
C	-1.826966	3.480554	0.483956	H	-5.685296	0.999537	1.239960
C	1.826918	-3.480472	-0.484055	H	5.685304	-0.999550	-1.239949
C	-1.173156	2.231298	0.324737	H	-6.100361	-0.983351	-1.076352
C	1.173133	-2.231212	-0.324770	H	6.100451	0.983276	1.076401
C	1.068976	1.543446	-0.515793	H	-6.473480	0.739165	-1.142510
C	-1.068968	-1.543357	0.515845	H	6.473443	-0.739267	1.142585
C	-1.566305	0.913476	0.596029	H	-7.758992	-1.270090	0.796975
C	1.566302	-0.913385	-0.596001	H	7.759128	1.269864	-0.796918
C	-0.649073	-0.135175	0.270561	H	-8.132015	0.450988	0.731490
C	0.649081	0.135266	-0.270504	H	8.132021	-0.451240	-0.731391
C	-2.944653	0.711201	1.151587	H	-8.588591	-1.548051	-1.582980
C	2.944652	-0.711102	-1.151555	H	-8.964320	0.188197	-1.649194
C	-3.980959	0.410178	0.044315	H	-9.852166	-0.871245	-0.530740
C	3.980982	-0.410219	-0.044268	H	9.852216	0.871063	0.530826
C	-5.370019	0.140491	0.620194	H	8.964442	-0.188541	1.649186
C	5.370045	-0.140529	-0.620140	H	8.588629	1.547695	1.583162
C	-6.422223	-0.126405	-0.456612				
C	6.422258	0.126298	0.456676				
C	-7.815628	-0.406321	0.110631				
C	7.815689	0.406107	-0.110555				
C	-8.862103	-0.673791	-0.969419				
C	8.862172	0.673512	0.969504				
H	1.139205	4.262137	-0.808205				
H	-1.139268	-4.262066	0.808064				
H	-1.147968	5.552476	0.007756				
H	1.147875	-5.552408	-0.007976				
H	-2.827558	3.623166	0.884480				
H	2.827506	-3.623084	-0.884590				
H	-2.949246	-0.113307	1.872136				
H	2.949261	0.113471	-1.872032				

Table C.6: Optimized geometry of **DPND6**$^{\cdot -}$.

Atoms	X (Å)	Y (Å)	Z (Å)	Atoms	X (Å)	Y (Å)	Z (Å)
O	1.526627	3.090773	0.556792	H	-1.396631	-0.763014	-3.302723
O	0.214943	-2.029415	-2.447340	H	4.520336	0.721277	0.732987
N	-0.413285	2.636149	-0.505706	H	-1.893837	-1.987858	-1.224102
N	2.154747	-1.568335	-1.387303	H	3.903863	1.684941	2.869139
C	-1.011510	3.843407	-0.193181	H	-3.276410	-1.903027	-2.310743
C	2.754526	-2.774722	-1.701233	H	2.214749	1.810144	2.409355
C	-2.281750	3.836060	-0.745030	H	-2.896448	-0.019066	0.084516
C	4.003952	-2.788306	-1.104768	H	2.835589	-0.051181	4.046772
C	-2.471592	2.600181	-1.413307	H	-4.318210	-0.105557	-0.944271
C	4.178615	-1.567048	-0.405651	H	3.737180	-0.851106	2.757152
C	-1.289235	1.846932	-1.259771	H	-3.269204	-2.375178	0.842546
C	3.011049	-0.798368	-0.592122	H	1.668103	-1.260482	1.482638
C	0.881532	2.269280	-0.103926	H	-4.694686	-2.499221	-0.188322
C	0.852528	-1.210693	-1.776585	H	1.543914	-1.895139	3.116042
C	-0.884324	0.562924	-1.691768	H	-4.354419	-0.488088	2.109838
C	2.589692	0.471006	-0.132568	H	0.338021	0.774476	2.197389
C	0.407476	0.108505	-1.326664	H	-5.788692	-0.633503	1.098249
C	1.308229	0.933824	-0.518876	H	0.161030	0.065821	3.803535
C	-1.895918	-0.241103	-2.478930	H	-6.134004	-3.009959	1.932056
C	3.525109	1.185256	0.817367	H	-6.124369	-1.844082	3.278161
C	-2.641779	-1.294525	-1.638781	H	-4.690394	-2.847993	2.954320
C	3.104198	1.173887	2.301670	H	-1.029763	-1.936571	2.730264
C	-3.502051	-0.717059	-0.515707	H	-0.846556	-1.144638	1.145538
C	2.865978	-0.198918	2.950163	H	-1.866096	-0.399836	2.393869
C	-4.093556	-1.783344	0.404837				
C	1.593574	-0.954551	2.535285				
C	-4.954570	-1.214203	1.533304				
C	0.285974	-0.185710	2.732771				
C	-5.507545	-2.282128	2.476005				
C	-0.931241	-0.958366	2.227797				
H	-0.462203	4.572337	0.392265				
H	2.216031	-3.492746	-2.309719				
H	-3.005790	4.647117	-0.670210				
H	4.722945	-3.604896	-1.166643				
H	-3.363969	2.275755	-1.941338				
H	5.049145	-1.267453	0.171384				
H	-2.631834	0.452918	-2.917054				
H	3.625640	2.236938	0.520570				

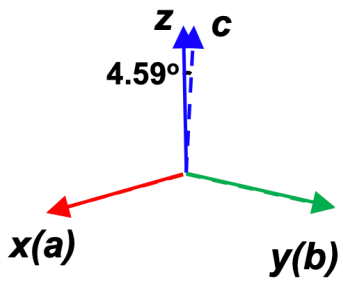

Figure C.1: Relative orientation between the Cartesian axes (x, y, z) and crystallographic axes (a, b, c) for **DPND**.

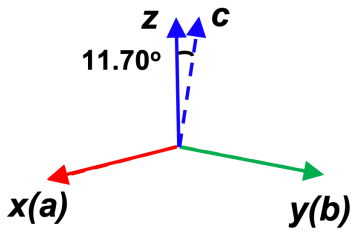

Figure C.2: Relative orientation between the Cartesian axes (x, y, z) and crystallographic axes (a, b, c) for **DPND6**.

Publications

- H. J. Brockmann[†], **L. Huang**[†], F. Hainer, D. Galindo, A. Jocic, J. Han, M. Kivala[*], A. Dreuw[*], T. Buckup[*], Photochemistry upon Charge Separation in Triphenylamine Derivatives from fs to μs. *J. Phys. Chem. B*, 2025, **129**(12), 3207–3215.
- **L. Huang**, J. Han, A. Dreuw[*]. Investigation of anisotropic electron and hole mobility in dipyrrolonaphthyridinedione (**DPND**) and **DPND6** crystals. (In Preparation)
- W. Zhang[†], **L. Huang**[†], J. Han, A. Dreuw[*]. Theoretical investigation of 3D anisotropic charge carrier mobility in halogenated N-heteroacenes: **4Br-TIPS-TAP** and **4I-TIPS-TAP**. (In Preparation)

Acknowledgements

Pursuing a doctoral degree at Heidelberg University is an extremely precious experience. It has been a challenging yet fruitful journey of growth. Standing at the end of this journey, I would like to express my sincere warmth and gratitude, bringing it to a perfect conclusion.

First of all, I would like to express my most sincere gratitude to Prof. Dr. Andreas Dreuw. You are not only an outstanding scholar with rigorous scholarship, but also a guide to enlighten the soul. While providing professional guidance, you always create an academic atmosphere that is both inspiring and warm and inclusive with your humor and friendliness. Special thanks to you for always believing in my potential when I was in a difficult situation and self-doubted. It was you who opened the door to the world of quantum chemistry for me.

I also sincerely thank Prof. Dr. Saeed Amirjalayer. Your persistent pursuit of scientific research and your generous advice have always benefited me greatly. At the same time, I would like to express my special gratitude to Dr. Jie Han. Despite your busy schedule, you still often spare time to offer guidance and provide many insightful views and patient support.

I would further like to thank Manfred Trunk, Prof. Dr. Tiago Buckup, Prof. Dr. Milan Kivala, Dr. Wen-Shan Zhang, Dr. Dirk Rehn, Dr. Adrian Dempwolff, Dr. Philipp Pracht, Dr. Adem Kulahlioglu, Dr. Nils Oberhof, Dr. Marco Bauer and Dr. Golokesh Santra for their constant help throughout my PhD. From software usage to technical questions, you never hesitated to assist. I am also very thankful to Felicitas Hirsch, Linus Dittmer, Sebastian Pauly, Antonia Papapostolou, Friederike Schneider, Anna Weidlich, Adrian Müller, Jonas Leitner, Tobias Kaczun, Lin Tian, Vyshna Ratheesh, Linghua Zhang, Melih Ceylan, Oscar Obel, Anna Ulrich, Christoph Popko and Hendrik J. Brockmann. Your support, cooperation, and friendship created a warm and energetic working environment. Through seminars, joint projects, and daily conversations, we shared ideas and grew together. It has been a privilege to be part of such a team - one of the most rewarding experiences in my life.

I would like to thank my family. Though far away, your love and encouragement have always been with me. In times of stress and solitude, it was your faith in me that gave me strength. Your understanding and unwavering support allowed me to focus fully on my studies and pursue my dreams.

Meanwhile, I am deeply grateful to the China Scholarship Council (CSC) for its financial support and to the German Science Foundation (DFG) for their funding and trust. I acknowledge the use of ChatGPT to proofread my final draft. I owe my deepest appreciation to all the teachers and friends who have supported, inspired, and accompanied me along the way. You have made this doctoral journey meaningful, and your kindness will always stay with me.

Bibliography

[1] A. Larkum, *Current opinion in biotechnology* **2010**, *21*, 271–276.

[2] R. E. Blankenship, *Molecular mechanisms of photosynthesis*, John Wiley & Sons, **2021**.

[3] B. Ke, *Photosynthesis: photobiochemistry and photobiophysics*, Springer, **2001**.

[4] G. D. Scholes, G. R. Fleming, A. Olaya-Castro, R. Van Grondelle, *Nature chemistry* **2011**, *3*, 763–774.

[5] G. Dennler, N. S. Sariciftci, C. J. Brabec, *Semiconducting Polymers: Chemistry Physics and Engineering* **2006**, *1*, 455–530.

[6] O. Lopez-Estrada, H. G. Laguna, C. Barrueta-Flores, C. Amador-Bedolla, *ACS omega* **2018**, *3*, 2130–2140.

[7] J. K. Utterback, J. L. Ruzicka, H. R. Keller, L. M. Pellows, G. Dukovic, *Annual review of physical chemistry* **2020**, *71*, 335–359.

[8] S. Y. Reece, D. G. Nocera, *Annual review of biochemistry* **2009**, *78*, 673–699.

[9] J. Blumberger, *Chemical reviews* **2015**, *115*, 11191–11238.

[10] H. R. Williamson, B. A. Dow, V. L. Davidson, *Bioorganic chemistry* **2014**, *57*, 213–221.

[11] R. Williams, *Molecular Physics* **1989**, *68*, 1–23.

[12] C. C. Moser, J. M. Keske, K. Warncke, R. S. Farid, P. L. Dutton, *Nature* **1992**, *355*, 796–802.

[13] H. Shiozawa, B. C. Bayer, H. Peterlik, J. C. Meyer, W. Lang, T. Pichler, *Scientific Reports* **2017**, *7*, 2439.

[14] W. Sun, M. Li, J. Fan, X. Peng, *Accounts of Chemical Research* **2019**, *52*, 2818–2831.

[15] B. Daly, J. Ling, A. P. De Silva, *Chemical Society Reviews* **2015**, *44*, 4203–4211.

[16] A. P. De Silva, T. S. Moody, G. D. Wright, *Analyst* **2009**, *134*, 2385–2393.

[17] Y. Gao, Z. Yu, L. Huang, Y. Zeng, X. Liu, D. Tang, *Analytical chemistry* **2023**, *95*, 9130–9137.

[18] H. Niu, J. Liu, H. M. O'Connor, T. Gunnlaugsson, T. D. James, H. Zhang, *Chemical Society Reviews* **2023**, *52*, 2322–2357.

[19] D. Astruc, *Nature chemistry* **2012**, *4*, 255–267.

[20] P. R. Murray, J. H. Cox, N. D. Chiappini, C. B. Roos, E. A. McLoughlin, B. G. Hejna, S. T. Nguyen, H. H. Ripberger, J. M. Ganley, E. Tsui, et al., *Chemical reviews* **2021**, *122*, 2017–2291.

[21] A. R. Allen, E. A. Noten, C. R. Stephenson, *Chemical reviews* **2021**, *122*, 2695–2751.

[22] A. K. Bains, A. Sau, B. S. Portela, K. Kajal, A. R. Green, A. M. Wolff, L. F. Patin, R. S. Paton, N. H. Damrauer, G. M. Miyake, *Science* **2025**, *388*, 1294–1300.

[23] M. Xu, D. Li, K. Sun, L. Jiao, C. Xie, C. Ding, H.-L. Jiang, *Angewandte Chemie* **2021**, *133*, 16508–16512.

[24] M. J. Zachman, V. Fung, F. Polo-Garzon, S. Cao, J. Moon, Z. Huang, D.-e. Jiang, Z. Wu, M. Chi, *Nature Communications* **2022**, *13*, 3253.

[25] E. Santos, R. Nazmutdinov, W. Schmickler, *Current opinion in electrochemistry* **2020**, *19*, 106–112.

[26] E. Santos, W. Schmickler, *Chemical Reviews* **2022**, *122*, 10581–10598.

[27] C.-P. Hsu, L. Hammarström, M. D. Newton, *The Journal of Chemical Physics* **2022**, *157*.

[28] S. Giannini, J. Blumberger, *Accounts of Chemical Research* **2022**, *55*, 819–830.

[29] X. Chen, P. V. Kamat, C. Janáky, G. F. Samu, *ACS Energy Letters* **2024**, *9*, 3187–3203.

[30] S. Shao, M. A. Loi, *Advanced Materials Interfaces* **2020**, *7*, 1901469.

[31] N. Lu, L. Li, D. Geng, M. Liu, *Organic Electronics* **2018**, *61*, 223–234.

[32] T. V. Sawant, C. S. Yim, T. J. Henry, D. M. Miller, J. R. McKone, *Joule* **2021**, *5*, 360–378.

[33] R. A. Marcus, *The Journal of Chemical Physics* **1956**, *24*, 979–989.

[34] R. A. Marcus, *The Journal of chemical physics* **1956**, *24*, 966–978.

[35] H. Taube, *Science* **1984**, *226*, 1028–1036.

[36] N. S. Hush, *Transactions of the Faraday Society* **1961**, *57*, 557–580.

[37] V. Levich, *Adv. Electrochem. Electrochem. Eng* **1966**, *4*, 249–371.
[38] V. Levich, R.-R. Dogonadze, E. German, A. Kuznetsov, Y. I. Kharkats, *Electrochimica Acta* **1970**, *15*, 353–367.
[39] M. Bixon, J. Jortner, *Advances in Chemical Physics: Electron Transfer—from Isolated Molecules to Biomolecules. Part 1* **1999**, *106*, 35–202.
[40] J. Jortner, *The Journal of Chemical Physics* **1976**, *64*, 4860–4867.
[41] J. Han, PhD thesis, Heidelberg University, **2020**.
[42] A. Szabo, N. S. Ostlund, *Modern quantum chemistry: introduction to advanced electronic structure theory*, Courier Corporation, **1996**.
[43] T. Helgaker, P. Jorgensen, J. Olsen, *Molecular electronic-structure theory*, John Wiley & Sons, **2013**.
[44] P. Hohenberg, W. Kohn, *Physical review* **1964**, *136*, B864.
[45] W. Kohn, L. J. Sham, *Physical review* **1965**, *140*, A1133.
[46] A. D. Becke, *The Journal of chemical physics* **1993**, *98*, 5648–5652.
[47] R. G. Parr, S. R. Gadre, L. J. Bartolotti, *Proceedings of the National Academy of Sciences* **1979**, *76*, 2522–2526.
[48] E. Runge, E. K. Gross, *Physical review letters* **1984**, *52*, 997.
[49] M. E. Casida in *Recent Advances In Density Functional Methods: (Part I)*, World Scientific, **1995**, pp. 155–192.
[50] J. Roncali, *Accounts of chemical research* **2009**, *42*, 1719–1730.
[51] M. Liang, J. Chen, *Chemical Society Reviews* **2013**, *42*, 3453–3488.
[52] Z. Yu, L. Sun, *Advanced Energy Materials* **2015**, *5*, 1500213.
[53] J. Wang, K. Liu, L. Ma, X. Zhan, *Chemical reviews* **2016**, *116*, 14675–14725.
[54] V. Coropceanu, J. Cornil, D. A. da Silva Filho, Y. Olivier, R. Silbey, J.-L. Brédas, *Chemical reviews* **2007**, *107*, 926–952.
[55] T. He, X. Zhang, J. Jia, Y. Li, X. Tao, *Advanced Materials (Deerfield Beach Fla.)* **2012**, *24*, 2171–2175.
[56] B. Fraboni, A. Fraleoni-Morgera, A. Cavallini, *Organic Electronics* **2010**, *11*, 10–15.
[57] J.-D. Huang, S.-H. Wen, W.-Q. Deng, K.-L. Han, *The Journal of Physical Chemistry B* **2011**, *115*, 2140–2147.
[58] H. Ma, F. Lin, S. Cheng, J.-D. Huang, *The Journal of Physical Chemistry C* **2023**, *127*, 2524–2532.
[59] J.-D. Huang, S. Chai, F. Lin, H. Ma, *ACS Applied Electronic Materials* **2023**, *5*, 2902–2911.
[60] L. Wang, L. Lin, J. Yang, Y. Wu, H. Wang, J. Zhu, J. Yao, H. Fu, *Journal of the American Chemical Society* **2020**, *142*, 10235–10239.
[61] S. Feng, Y. Zhao, W. Liang, *The Journal of Physical Chemistry A* **2022**, *126*, 6395–6406.
[62] E. Schrödinger, *Physical Review* **1926**, *28*, 1049–1070.
[63] M. Born, R. Oppenheimer, *Annalen der Physik* **1927**, *389*, 457–484.
[64] T. Helgaker, P. Jørgensen, J. Olsen, *Molecular Electronic-Structure Theory*, John Wiley & Sons Ltd, Chichester, West Sussex, **2000**.
[65] L. H. Thomas in Mathematical proceedings of the Cambridge philosophical society, *Vol. 23*, Cambridge University Press, **1927**, pp. 542–548.
[66] E. Fermi, *Rend. Accad. Naz. Lincei* **1927**, *6*, 32.
[67] N. D. Woods, M. Payne, P. Hasnip, *Journal of Physics: Condensed Matter* **2019**, *31*, 453001.
[68] J. P. Perdew, K. Schmidt in AIP conference proceedings, *Vol. 577*, American Institute of Physics, **2001**, pp. 1–20.
[69] J. P. Perdew, A. Ruzsinszky, J. Tao, V. N. Staroverov, G. E. Scuseria, G. I. Csonka, *The Journal of chemical physics* **2005**, *123*.
[70] M. Bursch, J.-M. Mewes, A. Hansen, S. Grimme, *Angewandte Chemie* **2022**, *134*, e202205735.
[71] M. Gray, A. Mandal, J. M. Herbert, *The Journal of Physical Chemistry A* **2025**, *129*, 3969–3982.
[72] C. A. Ullrich, *APL Computational Physics* **2025**, *1*.
[73] M. A. Marques, E. K. Gross, *Annu. Rev. Phys. Chem.* **2004**, *55*, 427–455.
[74] A. Dreuw, M. Head-Gordon, *Chemical reviews* **2005**, *105*, 4009–4037.
[75] D. B. Williams-Young, S. H. Yuwono, A. E. DePrince III, C. Yang, *Journal of Chemical Theory and Computation* **2023**, *19*, 9177–9186.
[76] S. Hirata, M. Head-Gordon, *Chemical Physics Letters* **1999**, *314*, 291–299.
[77] C. Reichardt, T. Welton, *Solvents and solvent effects in organic chemistry*, John Wiley & Sons, **2010**.
[78] J. Tomasi, B. Mennucci, R. Cammi, *Chemical reviews* **2005**, *105*, 2999–3094.
[79] E. Cances, B. Mennucci, J. Tomasi, *The Journal of chemical physics* **1997**, *107*, 3032–3041.
[80] B. Mennucci, *Wiley Interdisciplinary Reviews: Computational Molecular Science* **2012**, *2*, 386–404.
[81] N. Sutin, *Accounts of Chemical Research* **1982**, *15*, 275–282.
[82] N. S. Hush, *The Journal of Chemical Physics* **1958**, *28*, 962–972.
[83] T. M. Clarke, J. R. Durrant, *Chemical reviews* **2010**, *110*, 6736–6767.
[84] R. A. Marcus, *Reviews of Modern Physics* **1993**, *65*, 599–610.
[85] P. Song, B. Guan, Q. Zhou, M. Zhao, J. Huang, F. Ma, *Scientific reports* **2016**, *6*, 35555.

[86] Z. Chen, P. van der Hoorn, B. Baumeier, *Physical Review B* **2025**, *112*, 024202.

[87] E.-G. Kim, V. Coropceanu, N. E. Gruhn, R. S. Sánchez-Carrera, R. Snoeberger, A. J. Matzger, J.-L. Brédas, *Journal of the American Chemical Society* **2007**, *129*, 13072–13081.

[88] Y. Liu, X. Liu, J. Huang, J. Liu, S. Xie, Y. Zheng, *Journal of molecular modeling* **2016**, *22*, 182.

[89] M. A. Mumit, T. K. Pal, M. A. Alam, M. A.-A.-A.-A. Islam, S. Paul, M. C. Sheikh, *Journal of molecular structure* **2020**, *1220*, 128715.

[90] E. F. Valeev, V. Coropceanu, D. A. da Silva Filho, S. Salman, J.-L. Brédas, *Journal of the American Chemical Society* **2006**, *128*, 9882–9886.

[91] Y. Jiang, S. Zhang, B. Wang, T. Qian, C. Jin, S. Wu, J. Shen, *Tetrahedron* **2018**, *74*, 5733–5738.

[92] L. Wang, X. Yang, X. Chen, Y. Zhou, X. Lu, C. Yan, Y. Xu, R. Liu, J. Qu, *Materials Science and Engineering: C* **2017**, *72*, 551–557.

[93] H. Chen, P. Yang, Y. Li, L. Zhang, F. Ding, X. He, J. Shen, *Spectrochimica Acta Part A: Molecular and Biomolecular Spectroscopy* **2020**, *224*, 117384.

[94] Q. Xiong, K. Zhao, Y. Cheng, C. He, Y. Lai, M. Shi, X. Ming, F. Jin, D. Tao, R. Liao, et al., *Spectrochimica Acta Part A: Molecular and Biomolecular Spectroscopy* **2023**, *286*, 122012.

[95] A. Karak, S. K. Manna, A. K. Mahapatra, *Analytical Methods* **2022**, *14*, 972–1005.

[96] X. Gan, W. Li, C. Li, Z. Wu, D. Liu, B. Huang, H. Zhou, Y. Tian, *Sensors and Actuators B: Chemical* **2017**, *239*, 642–651.

[97] J. Preat, C. Michaux, D. Jacquemin, E. A. Perpete, *The Journal of Physical Chemistry C* **2009**, *113*, 16821–16833.

[98] A. Farokhi, H. Shahroosvand, F. Zisti, M. Pilkington, M. K. Nazeeruddin, *Journal of Materials Chemistry A* **2023**.

[99] Z. Wang, Q. Chen, J. Chen, Y. Zou, S. Ding, J. Chen, J. Yuan, C. Zhu, M. Liang, *Solar Energy* **2021**, *221*, 402–411.

[100] A. Farokhi, H. Shahroosvand, G. Delle Monache, M. Pilkington, M. K. Nazeeruddin, *Chemical Society Reviews* **2022**, *51*, 5974–6064.

[101] S. Protti, M. Mella, S. M. Bonesi, *New Journal of Chemistry* **2021**, *45*, 16581–16593.

[102] H. Görner, *The Journal of Physical Chemistry A* **2008**, *112*, 1245–1250.

[103] E. Forster, K. Grellman, *Chemical Physics Letters* **1972**, *14*, 536–538.

[104] N. Chattopadhyay, C. Serpa, P. Purkayastha, L. G. Arnaut, S. J. Formosinho, *Physical Chemistry Chemical Physics* **2001**, *3*, 70–73.

[105] S. M. Bonesi, D. Dondi, S. Protti, M. Fagnoni, A. Albini, *Tetrahedron Letters* **2014**, *55*, 2932–2935.

[106] K. Sreenath, C. V. Suneesh, V. K. Ratheesh Kumar, K. R. Gopidas, *The Journal of Organic Chemistry* **2008**, *73*, 3245–3251.

[107] X. Zheng, X. Wang, Y. Qiu, Y. Li, C. Zhou, Y. Sui, Y. Li, J. Ma, X. Wang, *Journal of the American Chemical Society* **2013**, *135*, 14912–14915.

[108] M. Kuratsu, S. Suzuki, M. Kozaki, D. Shiomi, K. Sato, T. Takui, K. Okada, *Inorganic chemistry* **2007**, *46*, 10153–10157.

[109] K. Do, D. Kim, N. Cho, S. Paek, K. Song, J. Ko, *Organic letters* **2012**, *14*, 222–225.

[110] H. J. Brockmann, L. Huang, F. Hainer, D. Galindo, A. Jocic, J. Han, M. Kivala, A. Dreuw, T. Buckup, *The Journal of Physical Chemistry B* **2025**, *129*, 3207–3215.

[111] M. Frisch, G. Trucks, H. Schlegel, G. Scuseria, M. Robb, J. Cheeseman, G. Scalmani, V. Barone, G. Petersson, H. Nakatsuji, et al., *Google Scholar There is no Corresponding Record for This Reference* **2016**.

[112] A. D. Becke, *The Journal of chemical physics* **1992**, *96*, 2155–2160.

[113] S. Grimme, S. Ehrlich, L. Goerigk, *Journal of computational chemistry* **2011**, *32*, 1456–1465.

[114] F. Weigend, R. Ahlrichs, *Physical Chemistry Chemical Physics* **2005**, *7*, 3297–3305.

[115] C. Adamo, V. Barone, *The Journal of chemical physics* **1999**, *110*, 6158–6170.

[116] A. Dreuw, M. Head-Gordon, *Journal of the American Chemical Society* **2004**, *126*, 4007–4016.

[117] J. C. Dobrowolski, G. Karpińska, *ACS omega* **2020**, *5*, 9477–9490.

[118] S. Sinnecker, F. Neese, *The Journal of Physical Chemistry A* **2006**, *110*, 12267–12275.

[119] J. Tomasi, *Wiley Interdisciplinary Reviews: Computational Molecular Science* **2011**, *1*, 855–867.

[120] J. Tomasi, B. Mennucci, E. Cancès, *Journal of Molecular Structure: THEOCHEM* **1999**, *464*, 211–226.

[121] A. V. Marenich, C. J. Cramer, D. G. Truhlar, *The Journal of Physical Chemistry B* **2009**, *113*, 6378–6396.

[122] C. Adamo, D. Jacquemin, *Chemical Society Reviews* **2013**, *42*, 845–856.

[123] D. Jacquemin, A. Planchat, C. Adamo, B. Mennucci, *Journal of chemical Theory and Computation* **2012**, *8*, 2359–2372.

[124] Z. Liu, T. Lu, Q. Chen, *Carbon* **2020**, *165*, 461–467.

[125] T. Lu, F. Chen, *Journal of computational chemistry* **2012**, *33*, 580–592.

[126] J. Sanz García, M. Boggio-Pasqua, I. Ciofini, M. Campetella, *Journal of Computational Chemistry* **2019**, *40*, 1420–1428.

[127] X. Wu, J. Han, S. Xia, W. Li, C. Zhu, J. Xie, *CCS Chemistry* **2022**, *4*, 2469–2480.

[128] J. M. Saveant, *The Journal of Physical Chemistry* **1994**, *98*, 3716–3724.

[129] C.-L. Ji, J. Han, T. Li, C.-G. Zhao, C. Zhu, J. Xie, *Nature Catalysis* **2022**, *5*, 1098–1109.

[130] H. Richtol, E. Fitzgerald Jr, P. Wuelfing Jr, *The Journal of Physical Chemistry* **1971**, *75*, 2737–2741.

[131] J.-D. Huang, S.-H. Wen, *Chemphyschem* **2013**, *14*, 2579–2588.
[132] G. Clark, A. Marwick, R. Koch, R. Laibowitz, *Applied Physics Letters* **1987**, *51*, 139–141.
[133] C. W. Tang, S. A. VanSlyke, C. H. Chen, *Journal of applied physics* **1989**, *65*, 3610–3616.
[134] J. H. Burroughes, D. D. Bradley, A. Brown, R. Marks, K. Mackay, R. H. Friend, P. L. Burns, A. B. Holmes, *nature* **1990**, *347*, 539–541.
[135] R. H. Friend, R. Gymer, A. Holmes, J. Burroughes, R. Marks, C. Taliani, D. Bradley, D. D. Santos, J.-L. Bredas, M. Lögdlund, et al., *Nature* **1999**, *397*, 121–128.
[136] M. E. Roberts, S. C. Mannsfeld, N. Queraltó, C. Reese, J. Locklin, W. Knoll, Z. Bao, *Proceedings of the National Academy of Sciences* **2008**, *105*, 12134–12139.
[137] L. Torsi, G. M. Farinola, F. Marinelli, M. C. Tanese, O. H. Omar, L. Valli, F. Babudri, F. Palmisano, P. G. Zambonin, F. Naso, *Nature materials* **2008**, *7*, 412–417.
[138] J. Zaumseil, H. Sirringhaus, *Chemical reviews* **2007**, *107*, 1296–1323.
[139] H. Sirringhaus, N. Tessler, R. H. Friend, *Science* **1998**, *280*, 1741–1744.
[140] C. W. Tang, *Applied physics letters* **1986**, *48*, 183–185.
[141] G. Yu, J. Gao, J. C. Hummelen, F. Wudl, A. J. Heeger, *Science* **1995**, *270*, 1789–1791.
[142] J. Roncali, *Chemical Society Reviews* **2005**, *34*, 483–495.
[143] J. T. Quinn, J. Zhu, X. Li, J. Wang, Y. Li, *Journal of Materials Chemistry C* **2017**, *5*, 8654–8681.
[144] S. Griggs, A. Marks, H. Bristow, I. McCulloch, *Journal of Materials Chemistry C* **2021**, *9*, 8099–8128.
[145] O. D. Jurchescu, J. Baas, T. T. Palstra, *Applied Physics Letters* **2004**, *84*, 3061–3063.
[146] J. E. Anthony, D. L. Eaton, S. R. Parkin, *Organic letters* **2002**, *4*, 15–18.
[147] U. H. Bunz, J. U. Engelhart, B. D. Lindner, M. Schaffroth, *Angewandte Chemie International Edition* **2013**, *52*, 3810–3821.
[148] M. Chu, J.-X. Fan, S. Yang, D. Liu, C. F. Ng, H. Dong, A.-M. Ren, Q. Miao, *Advanced materials* **2018**, *30*, 1803467.
[149] Y. Zhao, D. G. Truhlar, *Theoretical chemistry accounts* **2008**, *120*, 215–241.
[150] J. Kirkpatrick, *International Journal of Quantum Chemistry* **2008**, *108*, 51–56.
[151] B. Baumeier, J. Kirkpatrick, D. Andrienko, *Physical Chemistry Chemical Physics* **2010**, *12*, 11103–11113.
[152] H. Reiss, L. Ji, J. Han, S. Koser, O. Tverskoy, J. Freudenberg, F. Hinkel, M. Moos, A. Friedrich, I. Krummenacher, et al., *Angewandte Chemie International Edition* **2018**, *57*, 9543–9547.
[153] T. Wiesner, Z. Wu, J. Han, L. Ji, A. Friedrich, I. Krummenacher, M. Moos, C. Lambert, H. Braunschweig, B. Rudin, et al., *Chemistry–A European Journal* **2022**, *28*, e202201919.
[154] J. E. Norton, J.-L. Brédas, *Journal of the American Chemical Society* **2008**, *130*, 12377–12384.
[155] S. Yin, L. Li, Y. Yang, J. R. Reimers, *The Journal of Physical Chemistry C* **2012**, *116*, 14826–14836.
[156] J.-D. Huang, H. Ma, *ACS omega* **2022**, *7*, 48391–48402.
[157] H. M. Yamamoto, J.-I. Yamaura, R. Kato, *Journal of the American Chemical Society* **1998**, *120*, 5905–5913.
[158] H. M. Yamamoto, R. Maeda, J.-I. Yamaura, R. Kato, *Journal of Materials Chemistry* **2001**, *11*, 1034–1041.
[159] O. Pitayatanakul, K. Iijima, M. Ashizawa, T. Kawamoto, H. Matsumoto, T. Mori, *Journal of Materials Chemistry C* **2015**, *3*, 8612–8617.
[160] K. Müllen, U. Scherf, *Organic light emitting devices: synthesis, properties and applications*, John Wiley & Sons, **2006**.
[161] Z. Bao, J. Locklin, *Organic field-effect transistors*, CRC press, **2018**.
[162] K. Kudo, M. Yamashina, T. Moriizumi, *Japanese Journal of Applied Physics* **1984**, *23*, 130.
[163] S.-S. Sun, N. S. Sariciftci, *Organic photovoltaics: mechanisms, materials, and devices*, CRC press, **2017**.
[164] X. Xu, Y. Zhao, Y. Liu, *Small* **2023**, *19*, 2206309.
[165] L. Luo, W. Huang, C. Yang, J. Zhang, Q. Zhang, *Frontiers of Physics* **2021**, *16*, 33500.
[166] Y.-Y. Lin, D. Gundlach, S. Nelson, T. Jackson, *IEEE Electron Device Letters* **2002**, *18*, 606–608.
[167] X.-D. Tang, Y. Liao, H. Geng, Z.-G. Shuai, *Journal of Materials Chemistry* **2012**, *22*, 18181–18191.
[168] J. Cao, S. Yang, *RSC advances* **2022**, *12*, 6966–6973.
[169] Z. Shuai, H. Geng, W. Xu, Y. Liao, J.-M. André, *Chemical Society Reviews* **2014**, *43*, 2662–2679.
[170] T. Okamoto, *Polymer journal* **2019**, *51*, 825–833.
[171] L. Wang, W. Cai, J. Sun, Y. Wu, B. Zhang, X. Tian, S. Guo, W. Liang, H. Fu, J. Yao, *The Journal of Physical Chemistry Letters* **2021**, *12*, 12276–12282.
[172] Y. Wan, Z. Guo, T. Zhu, S. Yan, J. Johnson, L. Huang, *Nature chemistry* **2015**, *7*, 785–792.
[173] T. S. Volek, M. A. Verkamp, G. N. Ruiz, A. J. Staat, B. C. Li, M. J. Rose, J. D. Eaves, S. T. Roberts, *Journal of the American Chemical Society* **2024**, *146*, 29575–29587.

NATURWISSENSCHAFTLICH-MATHEMATISCHE GESAMTFAKULTÄT

COMBINED FACULTY OF NATURAL SCIENCES AND MATHEMATICS

RUPRECHT-KARLS-
UNIVERSITÄT
HEIDELBERG

Eidesstattliche Versicherung gemäß § 8 der Promotionsordnung für die Naturwissenschaftlich-Mathematische Gesamtfakultät der Universität Heidelberg / Sworn Affidavit according to § 8 of the doctoral degree regulations of the Combined Faculty of Natural Sciences and Mathematics

1. Bei der eingereichten Dissertation zu dem Thema / The thesis I have submitted entitled

   Quantum Chemical Investigation of Excited States and Electron Transfer in Organic Semiconductors

   handelt es sich um meine eigenständig erbrachte Leistung / is my own work.

2. Ich habe nur die angegebenen Quellen und Hilfsmittel (inkl. KI-basierter Hilfsmittel) benutzt und mich keiner unzulässigen Hilfe Dritter bedient. Insbesondere habe ich wörtlich oder sinngemäß aus anderen Werken übernommene Inhalte als solche kenntlich gemacht. / I have only used the sources indicated (incl. AI-based tools) and have not made unauthorised use of services of a third party. Where the work of others has been quoted or reproduced, the source is always given.

3. Die Arbeit oder Teile davon habe ich ~~wie folgt~~/bislang nicht [1)] an einer Hochschule des In- oder Auslands als Bestandteil einer Prüfungs- oder Qualifikationsleistung vorgelegt. / I have not yet/~~have already~~ [1)] presented this thesis or parts thereof to a university as part of an examination or degree.

   Titel der Arbeit / Title of the thesis:

   Hochschule und Jahr / University and year:

   Art der Prüfungs- oder Qualifikationsleistung / Type of examination or degree:

4. Die Richtigkeit der vorstehenden Erklärungen bestätige ich. / I confirm that the declarations made above are correct.

5. Die Bedeutung der eidesstattlichen Versicherung und die strafrechtlichen Folgen einer unrichtigen oder unvollständigen eidesstattlichen Versicherung sind mir bekannt. / I am aware of the importance of a sworn affidavit and the criminal prosecution in case of a false or incomplete affidavit

Ich versichere an Eides statt, dass ich nach bestem Wissen die reine Wahrheit erklärt und nichts verschwiegen habe. / I affirm that the above is the absolute truth to the best of my knowledge and that I have not concealed anything.

Heidelberg, 16.10.2025
Ort und Datum / Place and date

Lotao Huang
.....
Unterschrift / Signature

[1)] Nicht Zutreffendes streichen. Bei Bejahung sind anzugeben: der Titel der andernorts vorgelegten Arbeit, die Hochschule, das Jahr der Vorlage und die Art der Prüfungs- oder Qualifikationsleistung. / Please cross out what is not applicable. If applicable, please provide: the title of the thesis that was presented elsewhere, the name of the university, the year of presentation and the type of examination or degree.

The German text is legally binding.